

# Development and Characterisation of Silicon Photomultiplier Multichannel Arrays for the Readout of a Large Scale Scintillating Fibre Tracker

THÈSE N° 8842 (2018)

PRÉSENTÉE LE 21 SEPTEMBRE 2018  
À LA FACULTÉ DES SCIENCES DE BASE  
LABORATOIRE DE PHYSIQUE DES HAUTES ÉNERGIES 1  
PROGRAMME DOCTORAL EN PHYSIQUE

ÉCOLE POLYTECHNIQUE FÉDÉRALE DE LAUSANNE

POUR L'OBTENTION DU GRADE DE DOCTEUR ÈS SCIENCES

PAR

**Axel KUONEN**

acceptée sur proposition du jury:

Prof. P. Ricci, président du jury  
Prof. A. Bay, Dr G. Haefeli, directeurs de thèse  
Prof. U. Uwer, rapporteur  
Prof. A. Pellegrino, rapporteur  
Dr J.-M. Sallese, rapporteur



ÉCOLE POLYTECHNIQUE  
FÉDÉRALE DE LAUSANNE

Suisse  
2018



To my loved ones...

**A sword wields no strength unless  
the hands that holds it has courage.**

The Legend of Zelda



# Acknowledgements

This work would not have been made possible without the tremendous help of several people that I wish to thank by these few lines. First I would like to thank Aurelio Bay, my thesis director, to have offered me the possibility to work on a hardware related topic and for the help and advices he provided me along this work. I really enjoyed our big talks about music and amplifiers!

A huge thank you to Guido Haefeli, my thesis co-director, without whom this work would have been impossible. Guido is more than a supervisor to me and became over the years a mentor and a very close friend! I would like to insist on the pleasure I had working with you and how deeply I will miss you and our conversations.

To Maria Elena Stramaglia and Olivier Girard, my sidekicks in crime, for the wonderful time spent together in the lab or in conferences around the world! It was an honour to work with you two and I want to thank you for all the help and support you provided me on a daily basis. To Raymond Frei and its electronics team, Nicolas Auberson and Guy Masson for their precious help and their availability.

To Alain Pinard, Florian Bernard and the mechanical workshop for all the time they gave me and the mechanical pieces they made. I promise not to bother you anymore!

To Olivier Schneider and Fred Blanc for the intense discussions for the general mechanics class. After all, the correction sessions were not so bad.

To all the LPHE team without whom these four years would have been insipid. I will miss each of you. Special thanks to Tatsuya Nakada for the very challenging discussions during lunch breaks that helped to push things further.

To the "Quatuor du LPHE" for the good time spent together and the soccer physics tournament at lunch time. We have spent almost ten years together and I enjoyed every single day of it.

To the "Whocares" for the musical feelings and knowledge you brought me.

To the LHCb SciFi collaboration who is doing a tremendous work and who gave me the chance to present my results. I will always remember the testbeam campaigns and the group effort they represent.

To all the person I had the chance to work with during my PhD, for their advices, collaboration and good time spent together.

Pour finir à vous Mems et Peps, merci de tout coeur pour tout ce que vous avez fait pour moi. Une famille soudée et qui s'aime est la chose la plus importante dans ce monde et je réalise la

## **Acknowledgements**

---

chance que j'ai de vous avoir. Je ne serai jamais arrivé aussi loin sans vous... Merci!

*Lausanne, 12 June 2018*

Axel Kuonen

# Abstract

The current LHCb detector will continue collecting data until the long shutdown 2 (2019/2020). It will be upgraded in order to operate at higher luminosity. To achieve this, two major changes are required. First the Level-0 hardware trigger limited to 1 MHz will be replaced by a triggerless data acquisition running at 40 MHz. Secondly, the tracking system will be upgraded to cope with the higher track density and the required granularity. The Inner Tracker (silicon strip) and Outer Tracker (straw drift tubes) will be replaced with a single large area (300m<sup>2</sup>) scintillating fibre tracker (SciFi). The tracker is based on scintillating fibres read out by silicon photomultipliers (SiPM). A custom front-end chip has been designed for a fast readout.

This work presents the SiPM developments and motivates the choice of the selected technology. The SiPM technology is used for its high photo detection efficiency (PDE) and its single photon sensitivity due to its intrinsic high gain. Different technologies from two manufacturers, Hamamatsu and KETEK, were tested and compared. A detailed characterisation is presented for the selected design. The breakdown voltage, gain, temperature dependency, correlated noise, dark count rate (DCR) and PDE were found to fulfil the requirements for this application. The device reveals a peak PDE of 45% at the benchmark operation point.

SiPMs are radiation sensitive. The neutron fluence in the detector location increases dramatically the noise which was studied in many irradiation campaigns. The expected effect was found to be acceptable for the LHCb requirement.

This work focuses on novel SiPM characterisation methods that were developed for LHCb. In particular, a pulse shape statistical analysis to measure correlated noise probabilities, time constants and noise correction factors is presented. Setups to measure the PDE, from pulse frequency measurement, and the DCR, from IV measurements, were also developed.

The SciFi technology has an excellent application potential as for example beam tracking instrumentation. A telescope composed of four x-y scintillating fibre tracking stations is also presented. A track resolution of 16  $\mu\text{m}$  was achieved with a single hit spatial resolution of 36  $\mu\text{m}$ .

A simulation study implementing an optical focusing system at the SiPM micro-pixel using micro-lenses is presented. The micro-lenses allow to decrease the light loss at the dead areas and has the potential to reduce the total active area.

At the current state of production 20% of the 5500 SiPMs required for the LHCb SciFi have been fully electrically tested and geometrically and optical inspected. The detectors are selected in

## Abstract

---

groups featuring similar breakdown voltages, to be assembled on the cooling bars.

**Keywords:** Silicon photomultiplier arrays, Scintillating Fibre Tracker, SciFi Upgrade, LHCb, Beam telescope, Characterisation, Photodetectors.



## Résumé

Le détecteur LHCb continuera à collecter des données jusqu'au second long shutdown 2(2019/2020). Le détecteur sera amélioré pour fonctionner à plus haute luminosité. Pour y parvenir, deux changements majeurs sont requis. D'abord, le trigger de niveau 0 limité à 1 MHz sera remplacé par un système d'acquisition de données sans trigger fonctionnant à 40 MHz. Deuxièmement, les trajectographes seront mis à niveau pour faire face à la densité de trace plus élevée et la plus grande granularité requise. Le trajectographe interne (silicium) et le trajectographe externe (driftubes) seront remplacés par un seul trajectographe à fibre scintillante (SciFi) de grande surface ( $300 \text{ m}^2$ ). Le trajectographe est basé sur des fibres scintillantes lues par des photomultiplicateurs au silicium (SiPM). Une électronique de lecture personnalisée est utilisée pour une lecture rapide du système.

Ce travail présente les développements des SiPM et motive le choix de la technologie choisie dans ce contexte. La technologie SiPM est utilisée pour son efficacité élevée de détection de photon (PDE) et sa sensibilité pour détecter peu de photon en raison de son gain intrinsèque élevé. Différentes technologies de deux fabricants (Hamamatsu et KETEK) ont été testées et comparées. Une caractérisation détaillée est présentée pour le design sélectionné. La tension de claquage, le gain, la dépendance à la température, le bruit corrélé, la fréquence de bruit non-corrélé (DCR) et le PDE ont été jugés conformes aux exigences pour cette application. L'appareil révèle un PDE de crête de 45% au point de fonctionnement de référence. Les SiPM sont sensibles aux radiations. La fluence des neutrons à l'emplacement du détecteur augmente considérablement le bruit. Cet effet a été étudié dans de nombreuses campagnes d'irradiation et a été jugé acceptable selon les exigences.

Ce travail met l'accent sur les nouvelles méthodes de caractérisation des SiPMs qui ont été développées. En particulier, une analyse statistique de la forme de l'impulsion pour mesurer les probabilités de bruit corrélées, les constantes de temps et les facteurs de correction de bruit est présentée. Des bancs de test pour mesurer le PDE, à partir de la mesure des fréquences d'impulsion, ainsi que le DCR, à partir de mesures IV, ont également été développés.

La technologie SciFi présente un excellent potentiel d'applications en ce qui concerne l'instrumentation de faisceau. Une implémentation composée de quatre stations de fibres scintillantes x-y est présentée. Une résolution spatiale de  $36 \mu\text{m}$  et une résolution de la trace de  $16 \mu\text{m}$  ont été atteintes.

Une simulation mettant en œuvre un système de focalisation optique déposé sur les micro-

## Abstract

---

pixels des SiPM basés sur des micro-lentilles est présentée. Les micros-lentilles permettent de diminuer l'effet négatif des zones mortes et de réduire en même temps la surface active. Dans l'état actuel de la production, 20% des 5500 SiPMs requis pour le LHCb SciFi ont été entièrement testés électriquement, inspectés géométriquement et optiquement. Les détecteurs sont emballés par groupe de quatre partageant des tensions de claquage similaires et envoyés au centre d'assemblage pour installation.

# Zusammenfassung

Der aktuelle LHCb-Detektor nimmt Daten bis zum long shutdown 2 (2019/2020). Der Detektor wird umgebaut, um mit höherer Luminosität arbeiten zu können. Um dies zu erreichen, sind zwei wesentliche Änderungen erforderlich. Zuerst der Level-0-Hardwaretrigger auf 1 MHz begrenzt, wird durch ein triggerloses Datenerfassungssystem ersetzt mit einer Auslesefrequenz von 40 MHz. Zweitens wird das Trackersystem aufgerüstet, um der höheren Spurdichte und der erforderlichen Granularität gerecht zu werden. Der innere Tracker (Silizium) und der äußere Tracker (Drift tubes) werden durch einen einzigen großflächigen ( $300 \text{ m}^2$ ) Scintillator Fasertracker (SciFi) ersetzt. Der Tracker basiert auf szintillierenden Fasern, die mit einem Silizium-Photomultiplikator (SiPM) ausgelesen werden. Ein benutzerdefinierter Front-End-Chip wird für ein schnelles Auslesen des Systems verwendet.

Diese Arbeit stellt die SiPM-Entwicklungen vor und motiviert in diesem Zusammenhang die Auswahl der ausgewählten Technologie. Die SiPM-Technologie wird aufgrund ihrer hohen Lichtempfindlichkeit (PDE) verwendet. Verschiedene Technologien von zwei Herstellern (Hamamatsu und KETEK) wurden getestet und verglichen. Eine detaillierte Charakterisierung wird für das ausgewählte Design präsentiert. Die Durchbruchspannung, die Verstärkung, die Temperaturabhängigkeit, das korrelierte Rauschen, die Dunkelzählrate (DCR) und die PDE erfüllten die Anforderungen für diese Anwendung. Das Photodetektor hat eine maximale PDE von 45%. SiPMs sind Strahlung empfindlich. Die Neutronenstrahlung erhöht dramatisch die Dunkelstromrate welche in verschiedenen Testversuchen untersucht wurden. Der erwartete Effekt erwies sich als akzeptabel für die Anforderungen.

Diese Arbeit konzentriert sich auf neuartige SiPM-Charakterisierungsmethoden, die entwickelt wurden. Insbesondere wird eine Analyse zur Messung korrelierter Rauschwahrscheinlichkeiten, Zeitkonstanten und Rauschkorrekturfaktoren vorgestellt. Messvorrichtungen zur Bestimmung des PDE aus Pulsfrequenzmessung und DCR aus IV-Messungen wurden ebenfalls entwickelt.

Die SciFi-Technologie hat ein ausgezeichnetes Potential für Anwendungen wie für Teststrahlinstrumente. Eine Implementierung bestehend aus vier x-y-Scintillating-Faser-Tracking-Stationen wird vorgestellt und eine Orstauflösung von  $16 \mu\text{m}$  wurde erreicht.

Eine Simulationsstudie, die ein optisches Fokussierungssystem am SiPM-Mikropixel unter Verwendung von Mikrolinsen implementiert, wird vorgestellt. Die Mikro-Linsen ermöglichen es, die negativen Auswirkungen von nicht aktiven Bereichen zu verringern und gleichzeitig

## **Abstract**

---

die aktive Fläche zu reduzieren.

20% der für den LHCb SciFi benötigten 5500 SiPMs wurden vollständig elektrisch getestet, geometrisch und optisch geprüft. Die Detektoren wurden klassifiziert und wurden zur weiteren verarbeitung geschickt.

# Contents

<b>Acknowledgements</b>	<b>v</b>
<b>Abstract (English/Français/Deutsch)</b>	<b>vii</b>
<b>List of figures</b>	<b>xv</b>
<b>List of tables</b>	<b>xx</b>
<b>1 Introduction</b>	<b>1</b>
<b>2 LHC and the LHCb detector</b>	<b>3</b>
2.1 The LHCb experiment . . . . .	4
2.2 The LHCb tracking system . . . . .	5
2.2.1 Vertex locator . . . . .	5
2.2.2 Tracker Turicensis . . . . .	7
2.2.3 The dipole magnet . . . . .	7
2.2.4 T stations . . . . .	8
2.2.5 Track reconstruction . . . . .	9
2.3 The LHCb detector upgrade . . . . .	10
<b>3 The LHCb Scintillating Fibre Tracker</b>	<b>13</b>
3.1 Requirements, performances and constraints . . . . .	13
3.1.1 Requirements . . . . .	13
3.1.2 Geometry and radiation constraints . . . . .	14
3.2 General layout and working principle . . . . .	15
3.3 Scintillating fibre . . . . .	16
3.4 Silicon photomultiplier . . . . .	21
3.5 SciFi modules . . . . .	22
3.6 Readout electronics and data processing . . . . .	23
3.6.1 Front-end electronics with the PACIFIC chip . . . . .	23
3.6.2 Data processing and clustering . . . . .	25
3.6.3 Back-end electronic . . . . .	26

## Contents

---

<b>4</b>	<b>Photodetectors</b>	<b>29</b>
4.1	Light interaction in matter . . . . .	30
4.2	Vacuum based photodetectors . . . . .	31
4.2.1	Photomultiplier tubes (PMT): . . . . .	31
4.2.2	Hybrid photodetectors (HPD): . . . . .	32
4.2.3	Microchannel plates (MCP): . . . . .	33
4.3	Gaseous based photodetectors . . . . .	33
4.4	Solid-state photodetectors . . . . .	34
4.4.1	PIN diodes: . . . . .	34
4.4.2	Avalanche photodiode (APD): . . . . .	36
<b>5</b>	<b>SiPM characteristics and motivation for LHCb</b>	<b>39</b>
5.1	SiPM technology . . . . .	39
5.1.1	Electrical SiPM models . . . . .	41
5.2	Main characteristics of SiPMs . . . . .	44
5.2.1	Temperature dependency of the breakdown voltage . . . . .	45
5.2.2	Gain . . . . .	45
5.2.3	Correlated and uncorrelated noise . . . . .	45
5.2.4	Photo detection efficiency . . . . .	47
5.3	SiPM for the LHCb SciFi: requirements and development . . . . .	48
5.3.1	LHCb SiPM requirements . . . . .	48
5.3.2	SiPM technology evolution since 2011 . . . . .	50
<b>6</b>	<b>SiPM characterisation methods and results</b>	<b>53</b>
6.1	SiPM characterisation methods . . . . .	53
6.1.1	Pulse shape time dependent measurement . . . . .	53
6.1.2	PDE and gain measurement . . . . .	58
6.1.3	IV measurement . . . . .	61
6.1.4	Measurement with short SciFi module and electron-gun . . . . .	63
6.2	Results for the Hamamatsu H2017 . . . . .	66
6.2.1	Irradiation campaigns and results . . . . .	72
6.3	Results for the KETEK K2015 . . . . .	77
6.3.1	Irradiation results . . . . .	78
<b>7</b>	<b>LHCb SciFi packaging and flex cable</b>	<b>81</b>
7.1	Kapton flex assembly . . . . .	81
7.1.1	Ceramic stiffener and temperature sensor . . . . .	83
7.2	Qualification and stress tests . . . . .	86
7.2.1	Thermal cycling of the flex PCB . . . . .	86
7.2.2	Electrical cross-talk tests of the flex PCB . . . . .	86
7.2.3	Mechanical tests of the connectors . . . . .	86
7.2.4	Scratch tests of the optical surface . . . . .	87
7.2.5	Glueing tests . . . . .	88

7.3	Production quality control in Lausanne . . . . .	89
<b>8</b>	<b>Improvements over the current detector</b>	<b>91</b>
8.1	SiPM pixel implementation and micro-lens deposit . . . . .	91
8.1.1	Micro-lens simulation . . . . .	91
8.1.2	First iteration of lenses deposition . . . . .	93
8.2	Through Silicon Via . . . . .	94
8.3	Fast pulse output . . . . .	95
<b>9</b>	<b>Tests in beam and simulation</b>	<b>97</b>
9.1	The SciFi beam telescope . . . . .	97
9.1.1	Hit detection efficiency and spatial resolution . . . . .	99
9.2	SciFi Testbeam campaign . . . . .	101
9.2.1	Testbeam latest results . . . . .	101
9.3	Simulation of a SciFi detector and comparison with experimental results . . . .	104
<b>10</b>	<b>Conclusion</b>	<b>109</b>
<b>A</b>	<b>Experimental methods</b>	<b>111</b>
A.1	Pulse shape time dependent measurements . . . . .	111
A.2	Correlated noise corrections for the PDE . . . . .	112
A.3	PDE measurement setup additional informations: . . . . .	114
A.4	IV setup additional informations: . . . . .	116
A.5	Test setup with short SciFi module and electron-gun . . . . .	117
<b>B</b>	<b>Production testing and quality assurance</b>	<b>121</b>
B.1	Electrical tests and breakdown measurement . . . . .	122
B.2	Geometrical properties measurement . . . . .	123
B.3	Optical inspection . . . . .	124
<b>C</b>	<b>SiPM micro-lens simulation</b>	<b>127</b>
C.1	Photon generation . . . . .	127
C.2	Input of light on the lens . . . . .	128
C.3	Light transport through the lens . . . . .	128
C.4	SiPM pixel simulation and corresponding fill factor . . . . .	130
<b>D</b>	<b>Testbeam campaigns</b>	<b>131</b>
	<b>Bibliography</b>	<b>139</b>
	<b>Curriculum Vitae</b>	<b>141</b>





# List of Figures

2.1	CERN accelerator complex . . . . .	3
2.2	Distribution of the angles of the produced $b$ and $\bar{b}$ quarks . . . . .	4
2.3	Side view of the current LHCb detector . . . . .	5
2.4	pp interaction probability as a function the luminosity . . . . .	6
2.5	LHCb tracking system and track types for Run I and II . . . . .	6
2.6	VELO cross section in the (x,z) plane . . . . .	7
2.7	Schematic representation of a $R$ -sensor and a $\phi$ -sensor . . . . .	8
2.8	Schematic view of the TT detector . . . . .	8
2.9	Schematic view of an IT station . . . . .	9
2.10	Schematic view of the IT and OT station . . . . .	9
2.11	LHCb upgrade schematic side view . . . . .	11
3.1	SciFi layout and location . . . . .	14
3.2	LHCb upgrade radiation environment including neutron shielding . . . . .	15
3.3	The SciFi Tracker stations . . . . .	16
3.4	Illustration of the SciFi detection principle . . . . .	17
3.5	Scintillation process . . . . .	18
3.6	Energy levels of an organic molecule with $\pi$ -electronstructure. . . . .	19
3.7	Absorption and emission spectrum of compounds used in plastic scintillators . . . . .	20
3.8	Fibre emission spectrum . . . . .	20
3.9	SCSF-78MJ scintillating fibre cross-section . . . . .	21
3.10	Light propagation in the fibre . . . . .	21
3.11	Schematic view of a 6 layer SciFi mat for LHCb . . . . .	22
3.12	Exploded view of module assembly . . . . .	23
3.13	Readout box over-view . . . . .	24
3.14	PACIFIC channel architecture . . . . .	24
3.15	Functional diagram showing the data flow in the FE electronics . . . . .	25
3.16	The 10-bit clustering algorithm . . . . .	26
3.17	2-bit categorisation . . . . .	27
4.1	Total interaction cross section (left) and absorption depth (right) of photons in silicon . . . . .	31
4.2	PMT illustration . . . . .	31

## List of Figures

---

4.3	HPD illustration . . . . .	32
4.4	MPC illustration . . . . .	33
4.5	Gain for different solid-state photodetectors . . . . .	34
4.6	$p-n$ junction illustration . . . . .	35
4.7	$p-i-n$ diode cross-section illustration . . . . .	35
4.8	APD illustration . . . . .	37
5.1	G-APD cells in parallel . . . . .	40
5.2	KETEK SiPM silicon implementation . . . . .	40
5.3	Basic SiPM electrical model. . . . .	41
5.4	SiPM current generation steps . . . . .	42
5.5	Illustration of a bad avalanche quenching . . . . .	42
5.6	SiPM high frequency equivalent electrical circuit. . . . .	43
5.7	Current of the fast component flowing through $R_{Load}$ . . . . .	43
5.8	Current of the slow component flowing through $R_Q$ . . . . .	44
5.9	Illustration of DiXT and DeXT process . . . . .	46
5.10	Example of SiPM correlated noise with DiXT (top left), DeXT (top right) and AP (bottom centre). . . . .	47
5.11	SiPM mounted on flex PCB and channel zoom . . . . .	49
5.12	Example of amplitude distribution and illustration of the noise cut leading to inefficiency (signal cut) . . . . .	50
5.13	SiPM dead regions . . . . .	50
6.1	Illustration of the pulse shape measurement setup . . . . .	54
6.2	Illustration of $V_{BD}^{Amp}$ determination procedure . . . . .	55
6.3	$V_{BD}^G$ determination principle . . . . .	55
6.4	Illustration of the peak sorting algorithm using different amplitude thresholds and time windows . . . . .	56
6.5	Illustration of the limits of the peak sorting algorithm and multiple peak categorisation . . . . .	57
6.6	AP and DeXT mean lifetime determination . . . . .	58
6.7	Illustration of the PDE setup . . . . .	59
6.8	Illustration of the peak counting method . . . . .	59
6.9	Gain as a function of $\Delta V$ for one channel of H2017 . . . . .	60
6.10	IV characteristics measurement setup . . . . .	62
6.11	The IV logarithmic derivative and the linear fit with light injected . . . . .	63
6.12	Picture of the short fibre module setup . . . . .	64
6.13	Illustration of the light yield determination using the MPV of the distribution . . . . .	64
6.14	SPIROC pulse shape measured at the analogue output . . . . .	65
6.15	ADC dark spectrum at $\Delta V = 3.5$ V for detectors with high DCR . . . . .	66
6.16	Comparison of $V_{BD}$ from different methods . . . . .	67
6.17	$V_{BD}$ spread over the 128 channels of 20 detectors . . . . .	67
6.18	$R_Q$ distribution within one SiPM and of all 128 channels of 20 SiPMs . . . . .	68

6.19 Scatter plot of $V_{BD}$ as a function of $R_Q$ . . . . .	68
6.20 Recovery time measurement from the amplitude as a function of the arrival time for AP pulses . . . . .	69
6.21 Long decay time constant extracted from a fit of clean events . . . . .	69
6.22 Fit results of the time constants for different $\Delta V$ . . . . .	70
6.23 Correlated noise probabilities for a H2017 detector as a function of $\Delta V$ . . . . .	70
6.24 Amplitude of classified correlated noise pulses as a function of arrival time . . .	71
6.25 Example of a secondary classified pulse . . . . .	71
6.26 Correlated noise for 160 channels out from 20 different detectors . . . . .	72
6.27 PDE measurement for H2017 with current method . . . . .	72
6.28 PDE measurement for H2017 with frequency method . . . . .	73
6.29 DCR as a function of time during the annealing process . . . . .	74
6.30 DCR as a function of the fluence for proton and neutron irradiation . . . . .	74
6.31 DCR measured as a function of the temperature for three $\Delta V$ . . . . .	75
6.32 Cluster sum distribution for different irradiation level . . . . .	75
6.33 NCR for different $\Delta V$ (left) and irradiation levels (right) as a function of the seed threshold readout with the SPIROC ASIC . . . . .	76
6.34 NCR as a function of DCR at threshold of 2.5/1.5/4.5 PE . . . . .	76
6.35 Gain as a function of $\Delta V$ for on channel of K2015 wafer 4 . . . . .	77
6.36 K2015 wafer 4 noise characterisation . . . . .	78
6.37 K2015 wafer 4 PDE . . . . .	78
6.38 DCR measured as a function of the temperature for wafer 4 . . . . .	79
6.39 DCR measured as a function of the temperature for wafer 10 . . . . .	79
7.1 Kapton flex PCB . . . . .	81
7.2 Decoupling capacitors close to the detector . . . . .	82
7.3 Kapton flex PCB stackup and design . . . . .	83
7.4 Assembled SiPM on the Kapton flex PCB using solder ball . . . . .	83
7.5 Solder ball laser system . . . . .	84
7.6 SiPM x-ray picture . . . . .	84
7.7 Ceramic stiffener picture . . . . .	84
7.8 Temperature probe comparison . . . . .	85
7.9 x-y table for vibrational tests . . . . .	87
7.10 x-y table for scratching test . . . . .	88
7.11 Glueing stress test setup . . . . .	88
7.12 Main production steps for the different manufacturer companies and EPFL . .	89
8.1 Simulated lens disposition . . . . .	92
8.2 Simulated lens parametrisation . . . . .	92
8.3 Effect of the lens on the photon distribution . . . . .	93
8.4 Light intensity on the active area and the dead area . . . . .	94
8.5 First results of micro-lens deposit . . . . .	95
8.6 Profilometry of the SiPM surface . . . . .	95

## List of Figures

---

8.7	TSV cross section illustration . . . . .	96
8.8	The capacitively coupled fast output illustration . . . . .	96
9.1	Illustration of the SciFi telescope . . . . .	98
9.2	Picture of the SciFi telescope . . . . .	98
9.3	Scheme of the track reconstruction principle . . . . .	99
9.4	Hit detection efficiency of the x and y DUT stations as a function of $\Delta V$ . . . . .	100
9.5	Residual distribution of the x plane of DUT . . . . .	100
9.6	DESY testbeam setup . . . . .	102
9.7	Irradiated and non-irradiated long fibre module readout by SPIROC . . . . .	103
9.8	$\Delta V$ scans of the hit efficiency . . . . .	103
9.9	Hit efficiency as a function of the light yield . . . . .	104
9.10	$\Delta V$ scan of the residual . . . . .	105
9.11	Illustration of the fibre cross-talk . . . . .	105
9.12	Light yield and cluster size comparison for different interaction points . . . . .	107
A.1	Light intensity profile in the PDE setup . . . . .	115
A.2	Light intensity profile in the IV characterisation setup . . . . .	117
A.3	Light intensity recorded by one channel for different SiPM current . . . . .	118
A.4	SPIROC ADC gain as a function of the current . . . . .	119
B.1	Grey room picture . . . . .	121
B.2	Electrical test system used at Valtronic . . . . .	122
B.3	Picture of the production breakdown test setup . . . . .	123
B.4	SiPM dimensions definition . . . . .	124
B.5	Picture of the geometrical inspection setup . . . . .	125
B.6	Optical inspection setup . . . . .	125
C.1	Angular distribution of generated photons . . . . .	127
C.2	Simulation of the $3 \times 3$ pixels grid . . . . .	129
C.3	Vectors and angles definition . . . . .	130

# List of Tables

3.1	Polystyrene properties . . . . .	19
5.1	Typical model values for H2017 . . . . .	44
6.1	NCR comparison between SPIROC and PACIFIC for three different irradiation level	77
7.1	Flex electrical cross-talk results . . . . .	86
7.2	Glue test results . . . . .	88
8.1	Detected light increase for different lens implementations . . . . .	93
9.1	Hit efficiency for a non-irradiated module for three threshold sets . . . . .	104
B.1	SiPM chip tolerances on the different dimensions . . . . .	124



# 1 Introduction

This work takes place in the context of the LHCb Upgrade where parts of the LHCb detector will be replaced to cope with new, more stringent, requirements. The LHCb experiment and the LHCb Upgrade are presented in Chap.(2).

Chap.(3) focuses on the LHCb scintillating fibre tracker foreseen to replace the current tracking stations with detectors based on the scintillating fibre technology, readout by silicon photomultipliers. An introduction to photodetectors is given in Chap.(4) and the selected device is motivated in Chap.(5).

An important contribution of my work is the automatization of all characterisation setups and methods allowing fast and more precise measurements of key characteristics of a large number of silicon photomultipliers. The setups, the methods and the results obtained for different silicon photomultipliers technologies are presented in Chap.(6). Irradiation campaigns were required to fully characterise the photodetectors. The results obtained by the studies of irradiated detectors are also presented.

I helped developing the quality assurance setups required for the SiPM production testing. The results obtained can be seen in Chap.(7)

To improve the radiation hardness of the detector new technologies were studied. I have studied at the level of simulations a micro-lens technique to increase the efficiency of light collection. A first prototype test was also performed and results can be seen in Chap.(8).

My work also included the construction of a fibre based telescope used during testbeams for tracks reconstructions. This work included the telescope design, construction, operation and data analysis. The telescope is presented in Chap.(9). This chapter also presents results obtained by the SciFi LHCb collaboration during the latest testbeams. It also presents the results of a simulation that helps understanding the physical processes happening in the SciFi tracker. The results of the simulation are compared to the testbeam data.





## 2 LHC and the LHCb detector

The European Organisation for Nuclear Research (CERN) in Geneva is the one of largest high energy physics facility in the world. Its motivation is the understanding of the fundamental law of our Universe by studying the smallest component of matter, the so called "particles". CERN provides, among other facilities, particle accelerators that delivers particle beams of different types with wide ranges of energies and intensities. LHC is the largest accelerator consisting of a 27 km ring of superconducting magnets located in an underground tunnel. The CERN accelerator complex can be seen in Fig.2.1. Two proton beams are accelerated in opposite directions and collide in four interaction points where the main experiments (ALICE, ATLAS, CMS and LHCb) are located. The center of mass energy of  $\sqrt{s} = 13$  TeV for proton-proton collisions is achieved since 2015 and will continue until the end of Run 2 in the end of 2018. For Run 3 (2021) the center of mass energy will be raised to  $\sqrt{s} = 14$  TeV. Next to proton-proton, LHC also provides heavy ions-proton and heavy ions-heavy ions collisions.

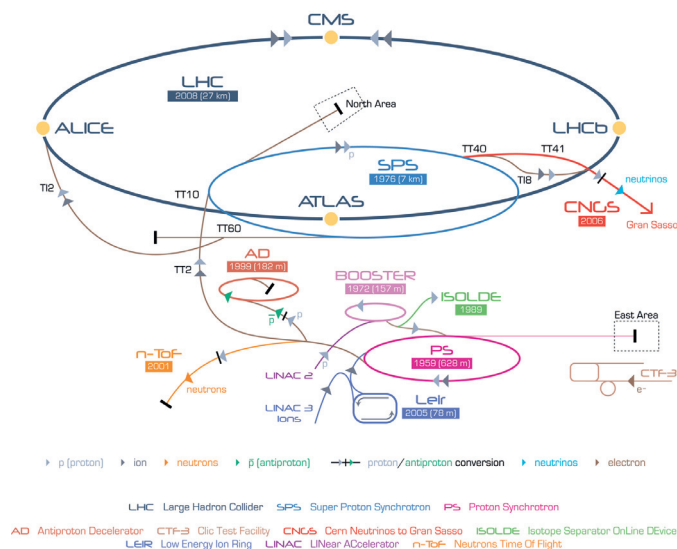


Figure 2.1: Schematics of the CERN accelerator chain complex [1]. It shows the LHC collider with its injectors and the main experiments.

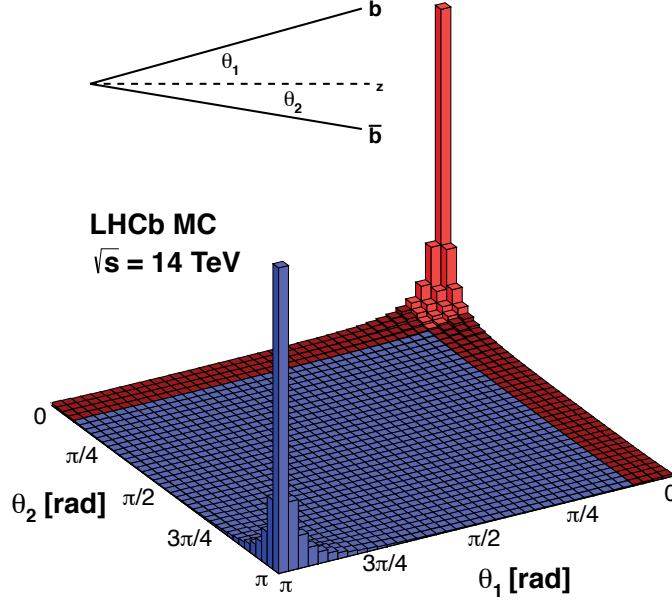


Figure 2.2: Two-dimensional distribution of  $\theta_1$  and  $\theta_2$  angles of the  $b$  and  $\bar{b}$  produced from  $\sqrt{s} = 14 \text{ TeV}$  proton-proton collisions. The red colour indicates the acceptance of LHCb. Image taken from [3].

## 2.1 The LHCb experiment

LHCb is a single-arm spectrometer with a forward angular coverage from approximately 10 mrad to 300 (250) mrad in the bending (non-bending) plane [2]. LHCb is dedicated to b-quark physics and to matter-antimatter symmetry (CP violation). Most of the  $b\bar{b}$  pairs of interest are emitted in a pseudo-rapidity range of  $1.8 < \eta < 4.9$  where  $\eta$  is defined as  $\eta = -\ln(\tan(\theta/2))$ , and  $\theta$  is the angle between the particle's momentum  $\vec{p}$  and the beam axis (Fig.(2.2)).

A schematic side-view of the LHCb detector is shown in Fig.2.3. LHCb is composed by a tracking system, a particle identification system and calorimeters. Are part of the tracking system: the vertex locator (VELO, see Sec.(2.2.1)), the tracker Turicensis (TT, see Sec.(2.2.2)), a dipole magnet (see Sec.(2.2.3)) and the three T tracking stations (see Sec.(2.2.4)). The particle identification systems includes: two Cherenkov detectors (RICH), electromagnetic and hadronic calorimeters, and muon chambers.

The coordinate system origin is located at the proton-proton interaction point and the z axis is coinciding with the beam axis, pointing from the interaction point to the muon chambers.

During proton beam collisions, a large number of particle is created from the primary proton-

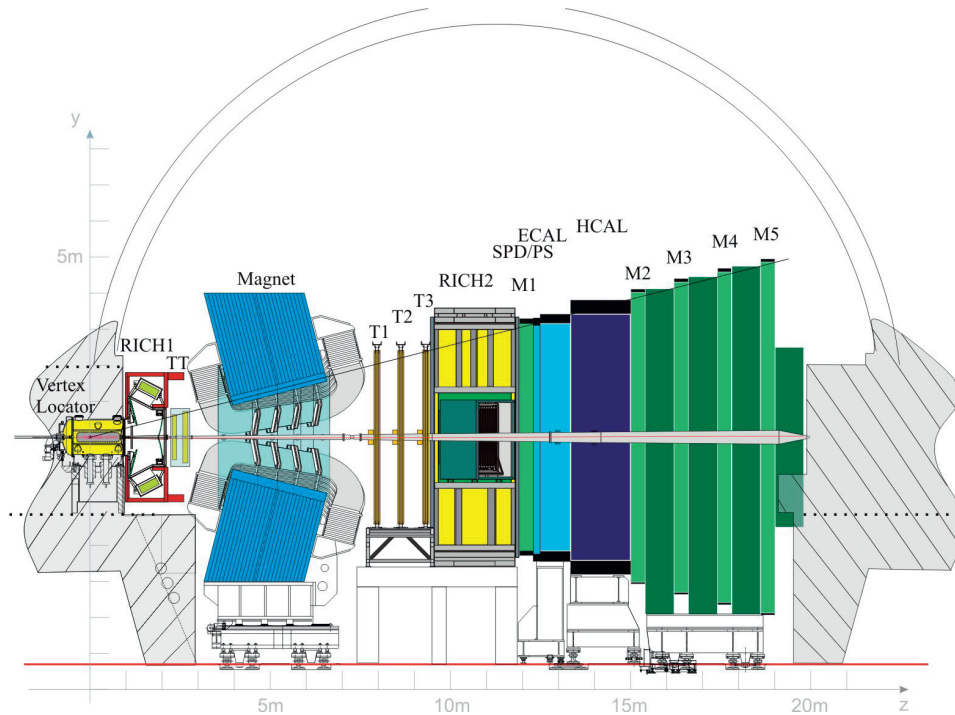


Figure 2.3: Schematic side view of the LHCb detector in its current state. Each subdetector is shown. Image taken from [2].

proton interaction. The number of primary proton-proton collision per bunch crossing at the interaction point is called pile-up  $\nu$ . LHCb nominal luminosity is lowered compared to the other experiments to reduce radiation damage in the detector and simplify the event reconstruction (low pile-up). A specific beam-focussing method is implemented resulting to a nominal luminosity at the interaction point of  $\mathcal{L} = 4 \times 10^{32} \text{ cm}^2 \text{ s}^{-1}$ . At this luminosity, events are dominated by single proton-proton interactions [4]. The pile-up as a function of the luminosity can be seen in Fig.(2.4).

## 2.2 The LHCb tracking system

This section focuses in more details on each sub-parts of the tracking system starting with the one close to the interaction point. The tracking system is designed to reconstruct the trajectory of charged particles traversing the detector. Measuring the bending radius induced by the magnetic field, informations like the charge and the momentum of the particles can be obtained.

### 2.2.1 Vertex locator

The VERTex LOcator (VELO) [2, 6, 7, 8] is a silicon-strip detector designed to provide precise measurements of tracks coordinates close to the interaction point. This coordinates are used

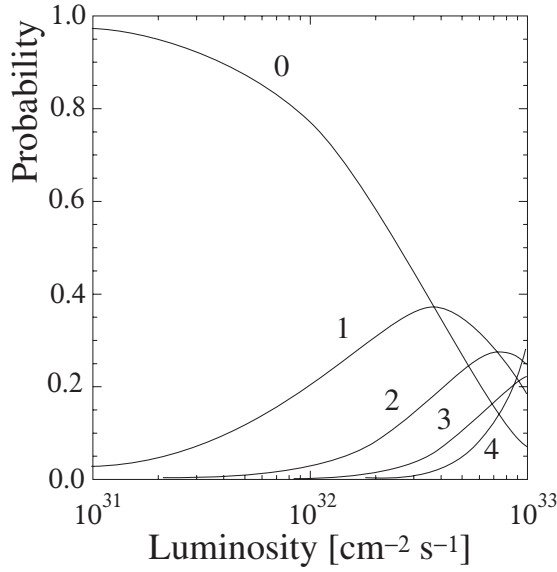


Figure 2.4: Probabilities for having 0,1,2,3 and 4 pp interactions per bunch crossing as a function of the machine luminosity at LHCb. Image taken from [4].

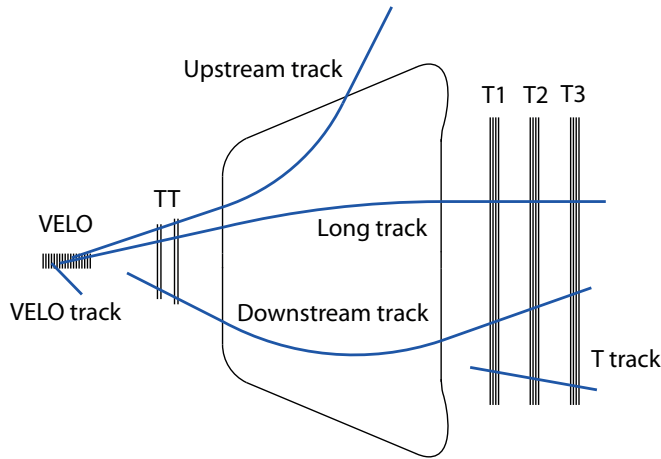


Figure 2.5: LHCb tracking system and different track types reconstruction. Image taken from [5].

to identify primary vertices and secondary vertices that are a distinctive feature of  $b$  and  $c$  quarks decays. The VELO covers the angular acceptance of the downstream sub-detectors, for particles with a pseudorapidity in the range  $1.6 < \eta < 4.9$  and emerging from primary vertices in the range  $|z| < 10.6\text{cm}$ . A schematic view of the positioning of the VELO modules can be seen in Fig.(2.6). It is manufactured with 84 single-sided radial ( $R$ ) and azimuthal-angle ( $\phi$ ) measuring stripes sensors. The sensors are assembled in 42 half-modules positioned

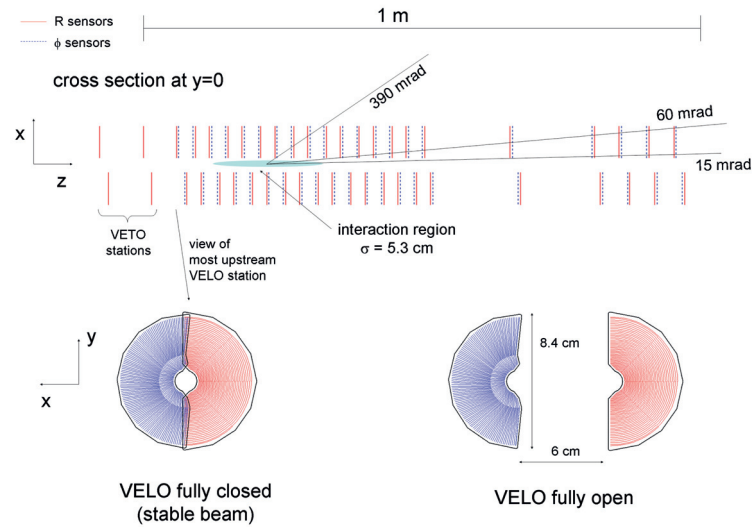


Figure 2.6: Schematic view of the VELO cross section in the  $(x,z)$  plane at  $y=0$  with the detector in the close state. The front face of the first module is illustrated in both open and closed positions. Image taken from [2].

on the left and right of the beam. The  $\phi$ -measuring sensors are subdivided into inner and outer regions while the  $R$ -measuring sensors cover  $45^\circ$  quadrants. Two additional stations are located in the backward direction forming the pile-up system allowing veto of event with multiple interaction or backward tracks. The sensors are located very close, about 8 mm to the beam during LHCb operation. To avoid radiation damages during beam dump, the detector can be moved away from the beam in a safe position.

### 2.2.2 Tracker Turicensis

The Tracker Turicensis is a 150 cm wide and 130 cm high planar tracking detector. It is located upstream of the magnet and uses silicon microstrip sensors with a strip pitch of about  $200 \mu\text{m}$  [2]. It has four detection layers arranged in  $x$ - $u$ - $v$ - $x$  planes ( $0^\circ, -5^\circ, +5^\circ, 0^\circ$  respectively) as shown in Fig.(2.8). The stations are host in a large light tight volume where the temperature is controlled to be below  $5^\circ\text{C}$  [9]. The spacial resolution achieved is  $50 \mu\text{m}$ .

### 2.2.3 The dipole magnet

A warm dipole magnet is used to measure the momentum of charged particles [2]. It is designed with a saddle-shaped coil in a window-frame yoke with sloping poles in order to match the detector acceptance. The magnet polarity can be flipped to study systematic uncertainty in tracking for charged particles. The bending power in the region  $0 < z < 10$  m is about 4 Tm in the horizontal plane.

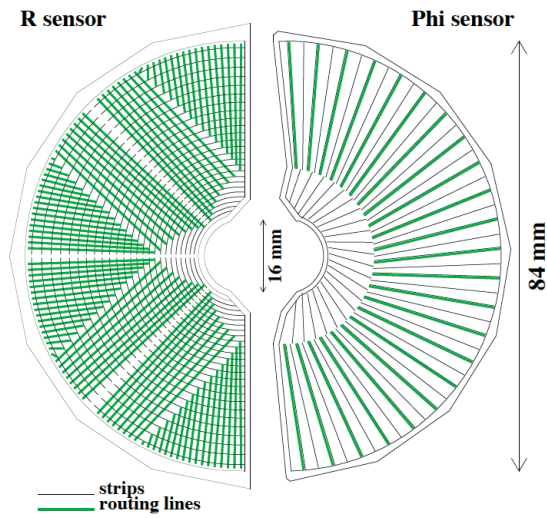


Figure 2.7: Schematic representation of a  $\phi$  and  $R$  sensors. The  $R$  sensors are arranged in four  $45^\circ$  quadrants and have routing lines perpendicular to the strips. The  $\phi$ -sensors are divided in outer and inner regions with routing lines parallel to the outer strips. Image taken from [6].

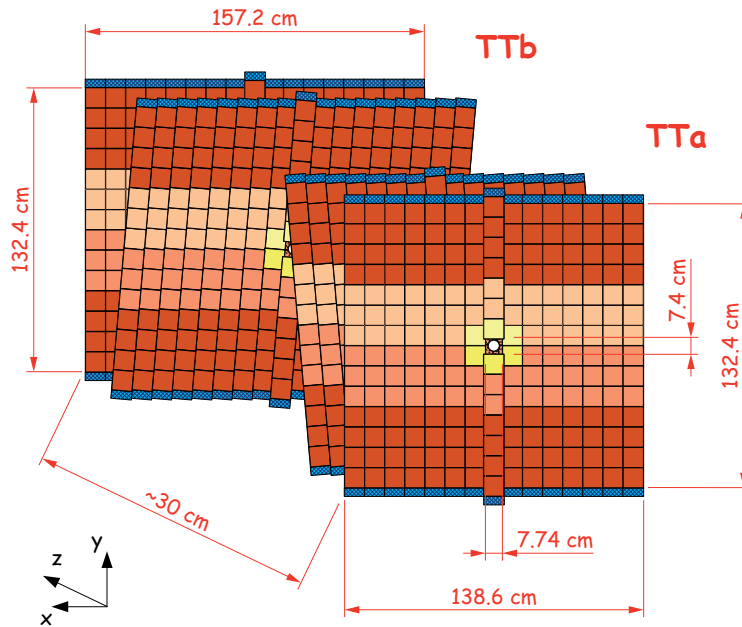


Figure 2.8: Schematic view of the four TT stations. Different readout sectors are indicated by different colors. Image taken from [10].

## 2.2.4 T stations

There are three downstream tracking stations: T1, T2 and T3. The current T stations consist of two separate sub-detectors: the Inner Tracker (IT) and Outer Tracker (OT)

The IT covers a 120 cm wide and 40 cm high cross shaped region in the centre of the three tracking stations located downstream of the magnet [2]. Like the TT, the IT uses silicon microstrip sensors with a strip pitch of about  $200\ \mu\text{m}$  and covers an area of  $0.35\ \text{m}^2$  close to the high track density region. The spacial resolution achieved is  $50\ \mu\text{m}$  and the hit efficiency is greater than 99%.

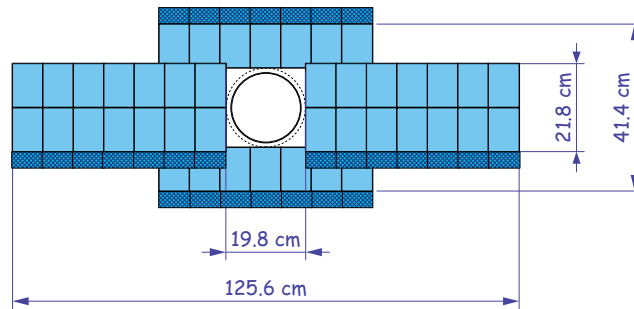


Figure 2.9: Layout of an x detection layer in the second IT station. Image taken from [10].

The OT uses large straw detectors and covers 99% of the  $30\ \text{m}^2$  detector surface. Its spatial resolution is  $200\ \mu\text{m}$  and the hit efficiency is above 99%. The gas mixture (70% Argon and 30%  $\text{CO}_2$ ) is chosen to guarantee a fast drift time below 50 ns. Both IT and OT planes are stereo layer angle oriented to remove ghost hits. A front schematic view is shown in Fig.(2.10).

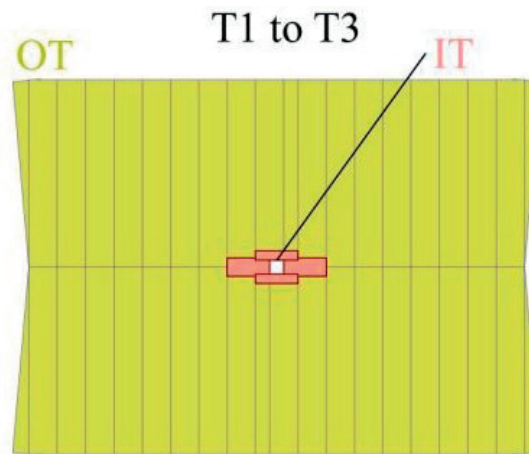


Figure 2.10: Schematic view of the OT and IT stations. Image taken from [11].

### 2.2.5 Track reconstruction

Depending on the charge particle hits in the different tracking sub-detectors, the tracks are classified in five categories [12], as illustrated in Fig.(2.5) :

- VELO tracks, where hits are only present in the VELO and are used for primary vertex

reconstruction and long track searches.

- T tracks, where hits are only present in the T stations. These tracks are used for long tracks reconstruction and are typically produced by secondary interactions.
- Long tracks, where hits are present in the full tracking system. They offer the most accurate momentum reconstruction.
- Upstream tracks, where hits are only present in the VELO and TT (decaying particles).
- Downstream tracks, where hits are only present in the TT and T stations. They are used to reconstruct long lives particles (neutral particles decaying between VELO and TT).

### 2.3 The LHCb detector upgrade

The LHCb detector in its initial configuration, will continue collecting data until the second long shutdown (LS2) of the LHC. Parts of the current LHCb detector need to be changed or replaced for Run 3. Results obtained during Run 1 and Run 2 shows that LHCb is robust and is performing well. However a limit of  $2 \text{ fb}^{-1}$  per year for interesting decay channels cannot be overcome [13]. The upgraded LHCb is planned to run with an instantaneous luminosity increased up to  $\mathcal{L} \approx 2 \times 10^{33} \text{ cm}^2 \text{ s}^{-1}$  [14] corresponding to an integrated value of  $5 \text{ fb}^{-1}$  per year. This luminosity can be achieved using 25 ns bunch spacing with an average pile-up  $\nu$  of 3.8 – 7.6. Two major changes are needed.

Firstly, the Level-0 hardware trigger will be replaced by a software trigger running at 40 MHz [15]. It requires to replace the front-end electronics of all tracking detectors and the RICH. This more flexible software-based trigger system will not only allow a large increase in data collection but also improve the trigger efficiency in particular decays.

Secondly, the current tracking system VELO, TT, IT and OT will be replaced to adapt to higher luminosity. The TT will be replaced by a new high-granularity silicon micro-strip plane based tracking detector called the Upstream Tracker (UT). For the T tracking stations (IT and OT) the granularity of the current OT is insufficient in the central region and will be replaced by a scintillating fibers tracker (SciFi) read out with silicon photomultipliers (SiPMs). The VELO detector will be replaced with a pixel detector readout by a custom developed VeloPix front-end ASIC [8]. The current technologies need to be replaced because of the following reasons [14]:

- The employed silicon sensors are not sufficiently radiation hard, especially in the inner region of the detector.
- The higher luminosity will lead to higher occupancies. VELO, TT and OT faces a problem.
- The current front-end ASIC (Beetle chip) needs to be replaced for the 40 MHz readout.



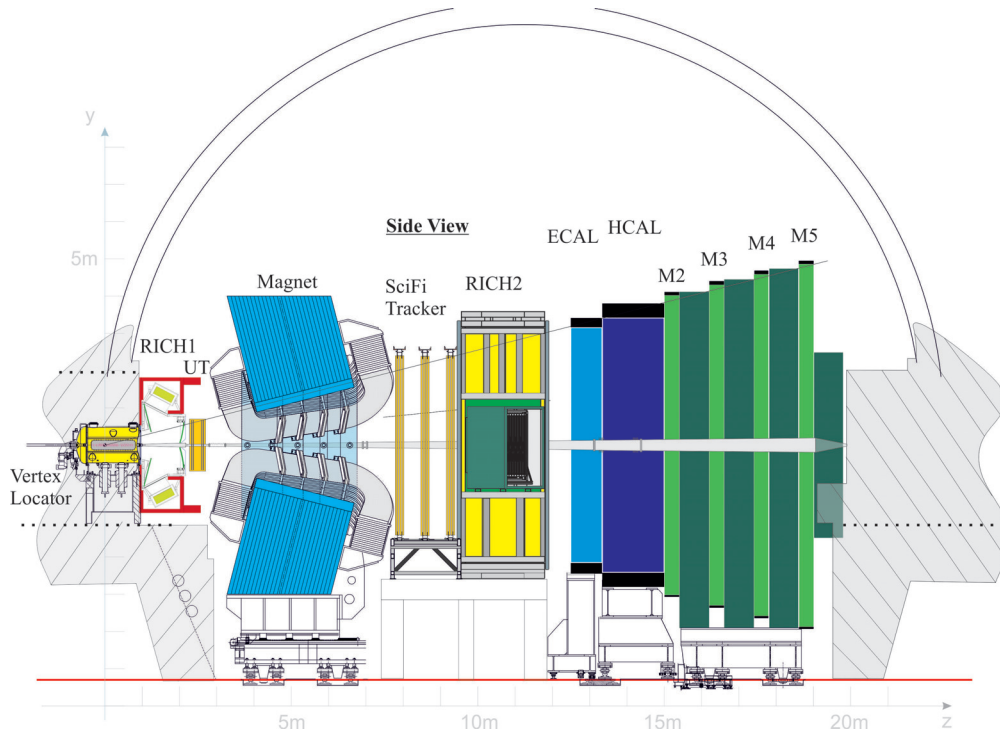


Figure 2.11: Schematic side view of the LHCb upgrade detector. The TT is replaced by the UT and the T stations by the SciFi Tracker.

A schematic side-view of LHCb with the TT replaced by the UT and the T stations by the SciFi tracker is shown in Fig.(2.11). This upgrade is scheduled for LS2 in 2019-2020 and is planned to operate ten years collecting a total of  $50 \text{ fb}^{-1}$  of data [16]. The SciFi tracker will be discussed in Chap.(3).



## 3 The LHCb Scintillating Fibre Tracker

The current OT and IT will be replaced by a single technology of scintillating fibres read out by silicon photomultipliers. This novel technology was never build in such a large scale resulting in many challenges. This chapter focuses on the requirements, performances, constraints and working principle of the SciFi tracker. The choice for each sub-parts of the detector is discussed in detail and motivated.

### 3.1 Requirements, performances and constraints

The track reconstruction requires a tracker with a high hit detection efficiency, good spacial resolution in the bending plane of the magnet and low material budget in the acceptance [14]. The readout electronics must be operated at 40 MHz interaction rate and the detector must withstand the harsh radiation environment.

#### 3.1.1 Requirements

The requirements for the SciFi tracker are the following [14]:

- The largest possible hit efficiency (>98%), while keeping the reconstructed noise below the signal rate at the same position (<10%).
- A spacial hit resolution better than 100  $\mu\text{m}$ . This resolution is sufficient since the extrapolation of tracks from the VELO will be dominated by multiple scattering in the sub-detectors upstream of the magnet.
- The amount of material should remain low in the acceptance region to minimise multiple scattering. A total radiation length ( $X/X_0$ ) of less than 1% per detection layer is required.
- The readout electronics needs to be adapted to the new readout scheme with small inefficiencies due to dead-times.

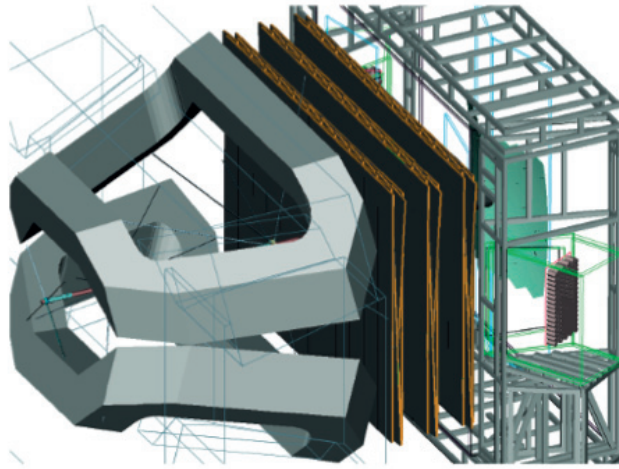


Figure 3.1: SciFi layout and location between the dipole magnet on the left and the RICH2 on the right. Image taken from [14].

- Performances must remain constant throughout the detector lifetime.

### 3.1.2 Geometry and radiation constraints

**Geometry constraints:** The geometry of the SciFi detection planes and its detection elements needs to be well known to ensure the resolution of the detector. This implies tolerances on the straightness and flatness (50-100  $\mu\text{m}$  in  $x$ -horizontal-direction and 300  $\mu\text{m}$  in the  $z$ -parallel to the beam-direction).

The  $z$  position of the stations are constrained by the available space of the OT and IT. The three T stations are placed at equidistant positions between the dipole magnet and the RICH2.

**Constraint by the radiation environment:** The radiation level expected for the upgraded detector has been simulated with FLUKA [17, 18]. The SiPM location, outside the detector acceptance, is partially shielded from the charged particle flux by the dipole magnet. The radiation in this location is mainly due to neutrons. With the assumption of a proton-proton cross-section of 84 mb, an integrated luminosity of  $50 \text{ fb}^{-1}$  and 14 TeV center-of-mass energy collision, the maximum neutron fluence expected is  $8.1 \cdot 10^{11} \text{ n}_{\text{eq}}/\text{cm}^2$  for T1 and  $14 \cdot 10^{11} \text{ n}_{\text{eq}}/\text{cm}^2$  for T3. The neutron flux is mainly produced at the calorimeters downstream of the SciFi tracker stations. To reduce this neutron flux, a shield made of polyethylene with 5% of boron is placed at the current M1 location (Fig.(2.3)). The M1 station will be removed in the LHCb upgrade. The neutron shield has a 10 cm (outer) and 20 cm (inner) thickness. The shield reduces the neutron flux by more than a factor two for T1 and more than a factor three for T3. The neutron fluence is then reduced to  $3.5 \cdot 10^{11} \text{ n}_{\text{eq}}/\text{cm}^2$  and  $4.7 \cdot 10^{11} \text{ n}_{\text{eq}}/\text{cm}^2$

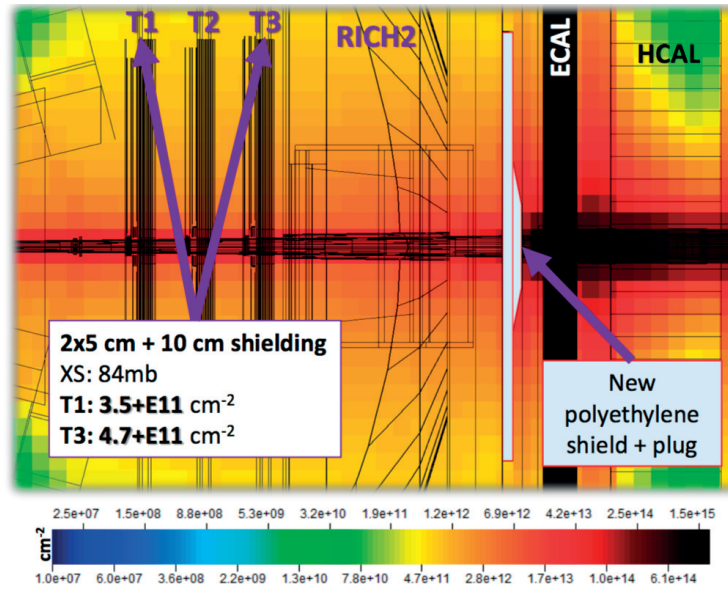


Figure 3.2: The LHCb upgrade radiation environment including a polyethylene with 5%boron neutron shielding. The shield is located at the actual M1 location and reduces the neutron fluence by a factor two and three at the SiPM location. Simulation taken from [19].

at the SiPM location for T1 and T3 respectively. The simulation results taken from [19] can be seen in Fig.(3.2). To the addition of neutron fluence, a charged dose of 50 Gy at T1 and 100 Gy at T3 will also be present [20]. The parts of the scintillating fibres in the most irradiated region around the beam pipe will have seen a total ionizing dose of 35 kGy mainly composed of charged hadrons.

To mitigate the effect of radiation on the SiPMs a cooling system capable of reaching the temperature of  $-40^\circ\text{C}$  for the SiPM and be stable within  $1^\circ\text{C}$  is used. The cooling system will be presented in Sec.(3.5).

### 3.2 General layout and working principle

This section presents the general layout of the LHCb SciFi tracker and illustrates its working principle. The SciFi tracker consists of three stations located between the dipole magnet and the RICH2. It covers a  $6 \times 5 \text{ m}^2$  surface and is based on  $250 \mu\text{m}$  diameter scintillating fibres. Each station is composed of 4 detection planes. The outer planes of each stations are aligned with the  $y$ -axis (called  $x$ -layer) while the two central one are tilted of  $+5^\circ$  and  $-5^\circ$  respectively (called  $u$ -layer and  $v$ -layer). Each detection layer is composed of scintillating fibres arranged in 6 layers fibre mats (Sec.(3.5)).

The light detection is made by multichannel SiPMs with a channel width of  $250 \mu\text{m}$ . Each channel is composed of pixels. The SiPM are glued on a cooling bar inside the cooling enclosure at the top and bottom of each module.

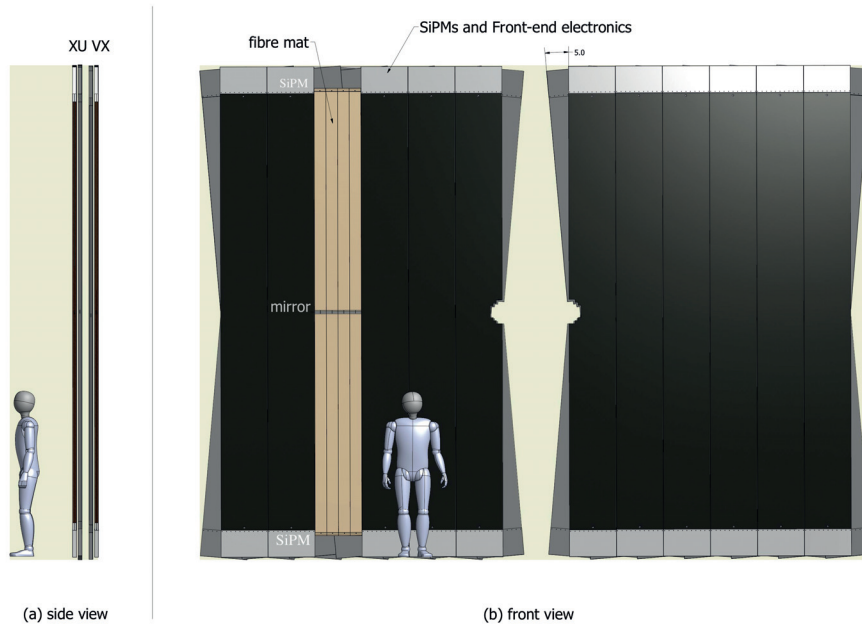


Figure 3.3: A SciFi Tracker station composed of four detection planes arranged in x-u-v-x. Each detection plane is composed of 12 modules. Image taken from [21].

**Working principle:** When a charged particle passes through a scintillating fibre it deposits its energy through ionisation subsequently transformed into light by the scintillating process (explained in Sec.(3.3)). Only a small portion (10.8%) of the scintillating photons is trapped in the fibre. The photon propagation in the fibre suffers from attenuation. The attenuation length of the fibre used for this project (SCSF-78MJ) is 320cm. The SiPMs are placed at one end of the fibre outside the main charged particle flux. A mirror is placed at the opposite side. The SiPM channels cover a set of fibres like illustrated in Fig.(3.4) and the number of incident photons is measured.

### 3.3 Scintillating fibre

The scintillating fibres must perform three tasks namely, the scintillation process, the photon trapping and the photon propagation through the fibre. For the LHCb SciFi, only organic scintillators are considered since inorganic material have a high atomic number, a long decay time and high costs. The ideal scintillating fibre for LHCb should possess the following properties [24]:

- Efficient conversion of the ionisation energy of charged particles into detectable light.

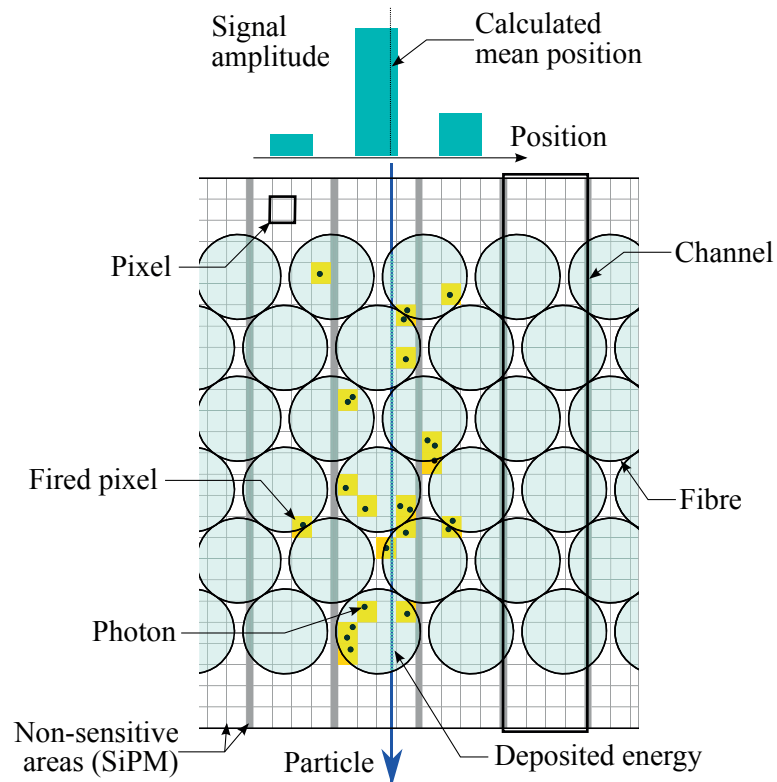


Figure 3.4: Illustration of a particle traversing a six layers fibre mat, creating photons. After the transport in the fibre, the light is detected by the SiPM. The triggered pixels can be seen in yellow. The signal amplitude for the channel is shown at the top [22, 23].

- Long attenuation length.
- Uniform geometrical aspect and no irregularities in diameter.
- The decay time of the scintillation process must be short to generate a fast signal pulse. A maximum of few nanoseconds is required for LHCb.
- Low cost

A compromise has to be made and scintillating fibres are found to be a viable option due to their cost and decay time.

Ionisation energy is deposited in the polymer core of the fibre. Few electron-volts of deposited energy is sufficient to produce an excitation of the polymer [25]. Polystyrene has proven to be a particularly efficient material. It represents 99% of the core material and is responsible for the non-radiative energy transfer (by dipole-dipole interaction, called Förster transfer) to the primary scintillators molecules also called primary dye. The decay time of polystyrene is quite long and the Förster energy transfer happens on very short distances. The addition of large concentration of the primary dye (1% of the core material) shorten the decay time and increases the light yield.

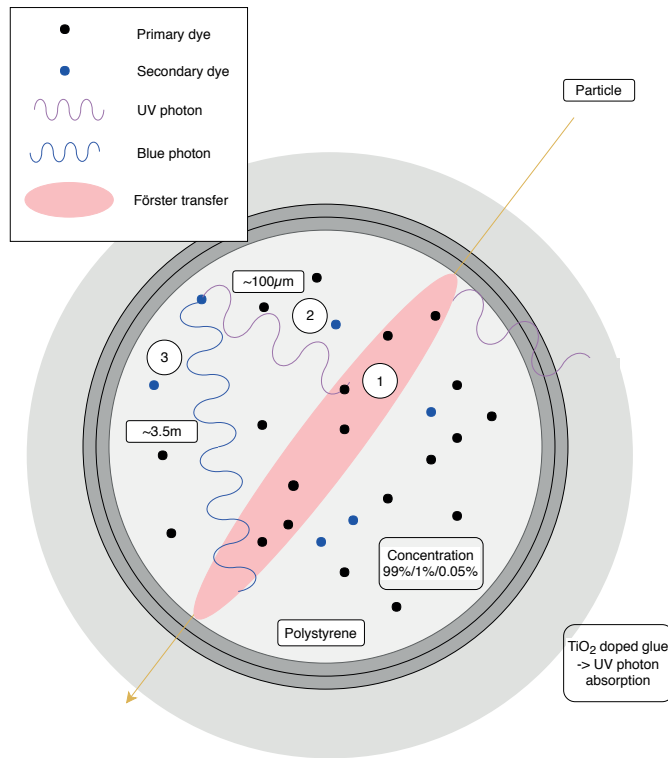


Figure 3.5: Steps of the scintillation process. (1) is the Förster energy transfer to the primary dye. (2) is the emission of an UV-photon from the excited primary dye. (3) is the UV photon absorption by the wavelength shifter and the emission of the blue photon.

The scintillation process is linked to the energy levels for  $\pi$ -electrons which are illustrated in Fig.(3.6). Free valence electrons are excited from the ground level  $S_0$  to higher excited singlet states. Thermal equilibrium to a lower state ( $S_1$ ) is rapidly reached ( $\sim 10^{-11}$  s). The radiative transition (called fluorescence) occurs in a typical time of  $10^{-8} - 10^{-9}$  s which constitutes the scintillation light. The triplet states can be populated ( $T_1$  and  $T_2$ ) and have slow transition times ( $>10^{-4}$  s) to  $S_0$  through phosphorescence. This light production is far outside the required time constraints of a fast readout and appears as noise (after-glow).

However, the first dye has a high attenuation to its own generated UV photons and is not adequate for the required wavelength emission spectrum. The produced UV-photons travel a mean distance of  $\sim 100\mu\text{m}$ . A second dye is then introduced to work as a wavelength shifter ( $\sim 0.05\%$  of the core material). It absorbs the photon emitted from the primary dye, via radiative or non-radiative transfer, and re-emit fluorescence light at a longer wavelength where the attenuation length of the fibre is acceptable.

As explained in the following, the only fibre that meet the LHCb requirements is the Kuraray SCSF-78MJ [29]. It uses p-terphenyl as primary dye and tetraphenyl-butadiene (TPB) as a wavelength shifter. The emission/absorption chain is shown in Fig.(3.7).



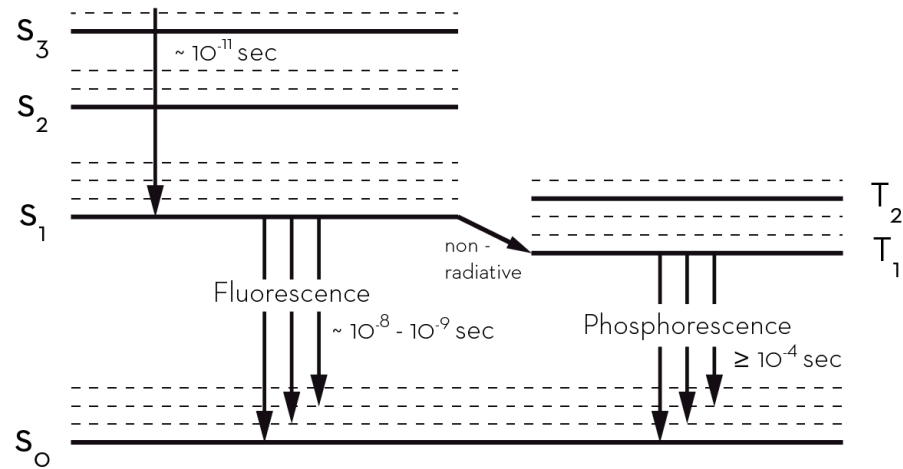


Figure 3.6: Energy levels of an organic molecule with  $\pi$ -electronstructure. Image taken from [26].

**Kuraray SCSF-78MJ requirement and properties:** The SciFi Tracker performance requirements call for a scintillating plastic material with short scintillation decay time, high intrinsic light yield, low specific density and nuclear charge number [30] (See Tab.(3.1)).

Scintillation decay time	$\tau_d$	<3 ns
Light yield	LY	>7000 ph/ MeV
Specific density	$\rho$	<1.1 g/cm <sup>3</sup>
Nuclear charge number	Z	<12

Table 3.1: Polystyrene properties [30].

The trapping efficiency of the fibre is 10.8% (Brewster angle of 5.4%). UV-photons generated from the first dye below 400 nm travel sufficiently far to reach neighbouring fibres and therefore generate a fibre to fibre cross-talk. The fibre emission spectrum peaks around 450 nm and can be seen in Fig.(3.8).

The scintillating fibre with a diameter of 250  $\mu\text{m}$  is illustrated in Fig.(3.9). The fibre is composed of a core and two cladding around it. The double cladding is added to improve the trapping efficiency. The cladding represents 6% of the fibre radius and acts as dead material. During the fibre production, irregularities in diameter (bumps) can appear which are related to the production process or contamination in the production environment. Bumps up to 300  $\mu\text{m}$  diameter are acceptable and do not impact the winding process (see Sec.(3.5)). A curing process was developed to remove larger bumps.

The light attenuation in the scintillating fibre is much higher than for clear fibres. The attenuation exhibit two exponential terms [32]:

1. A term which is attributed to light propagation in the cladding or following an helicoidal

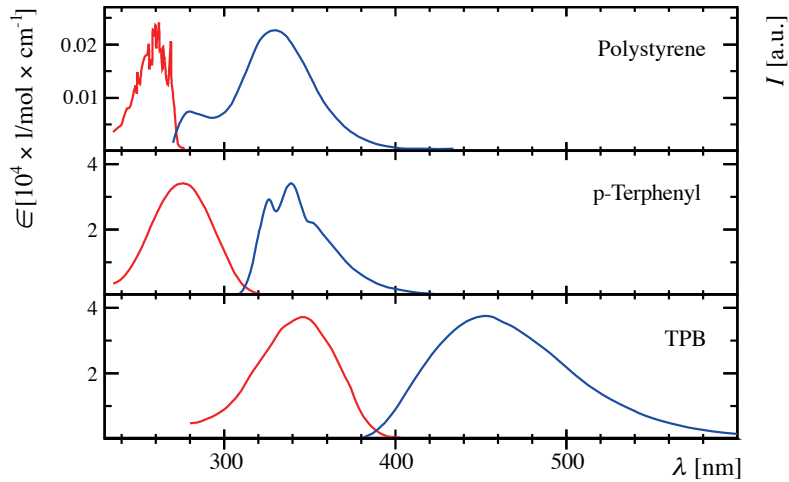


Figure 3.7: Absorption and emission spectra of compounds used in plastic scintillators. Red curves show the absorption, blue curves the emission intensity (number of photons). The data for polystyrene, p-terphenyl and TPB refers to solutions in cyclohexane and are obtained from [27]. Image taken from [28].

path as shown in the right plot in Fig.(3.10) (called short attenuation length).

2. A long attenuation length term describing the losses of the meridional light propagating in the core as shown in the left plot in Fig.(3.10). Note that the added scintillating molecules are responsible for higher attenuation. Hence it is important to minimise the quantity of scintillators.

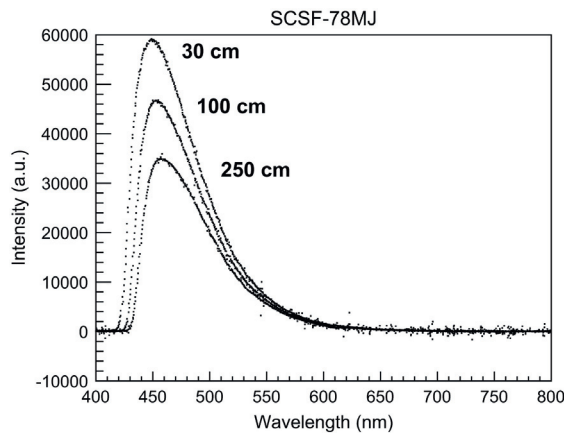


Figure 3.8: Wavelength spectra observed after varying distances traveled inside the fibre [31].

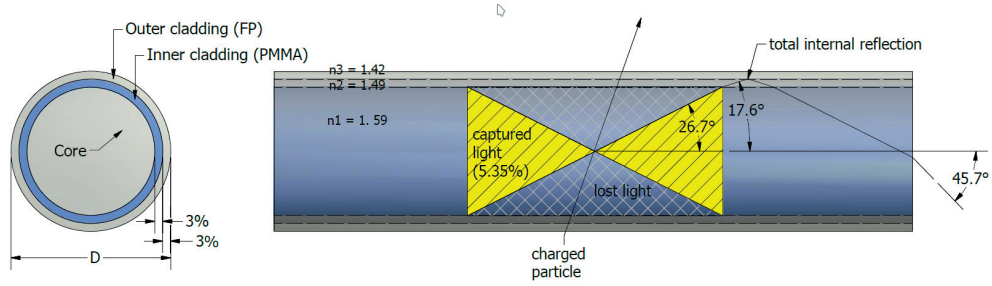


Figure 3.9: SCSF-78MJ scintillating fibre cross-section. Image taken from [32].

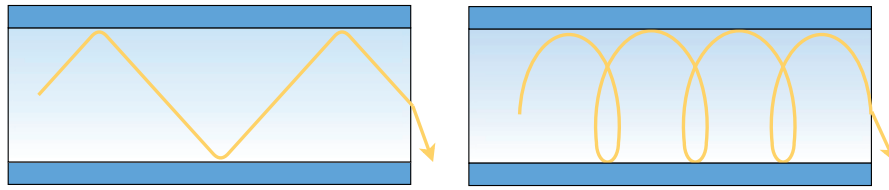


Figure 3.10: Meridional (left) and helicoidal (right) light propagation in the fibre.

The optical attenuation length of the fibre is of the order of  $\Lambda_{att} = 350$  cm, averaged over the wavelength range of the emitted light.  $\Lambda_{att}$  is defined as:

$$I(l)/I_0 = e^{-\frac{l}{\Lambda_{att}}} \quad (3.1)$$

with  $I_0$  the initial intensity and  $I(l)$  the expected intensity at a position  $l$  along the fibre.

**Fibres radiation requirements** Plastic scintillators exposed to ionising radiation show a decrease in light yield. Two major causes are identified: (1) degraded transmission properties of the polystyrene core and (2) a degradation of the scintillating and wavelength shifting fluors [32]. The second cause can be avoided using modern wavelength shifters. For the LHCb SciFi, the only degradation expected is due to the reduced transparency which is expected to be 40% after the full lifetime of the detector.

### 3.4 Silicon photomultiplier

SiPMs are solid-state photodetectors that offer all the key features required for low light applications in the context of a high resolution scintillating fibre tracker. Two SiPM manufacturers, Hamamatsu [33] and KETEK [34] have produced customised multi-channel arrays for the LHCb upgrade. The selection of the SiPM technology and their working principle is exposed in Chap.(5) and the characterisation methods are shown in Chap.(6).

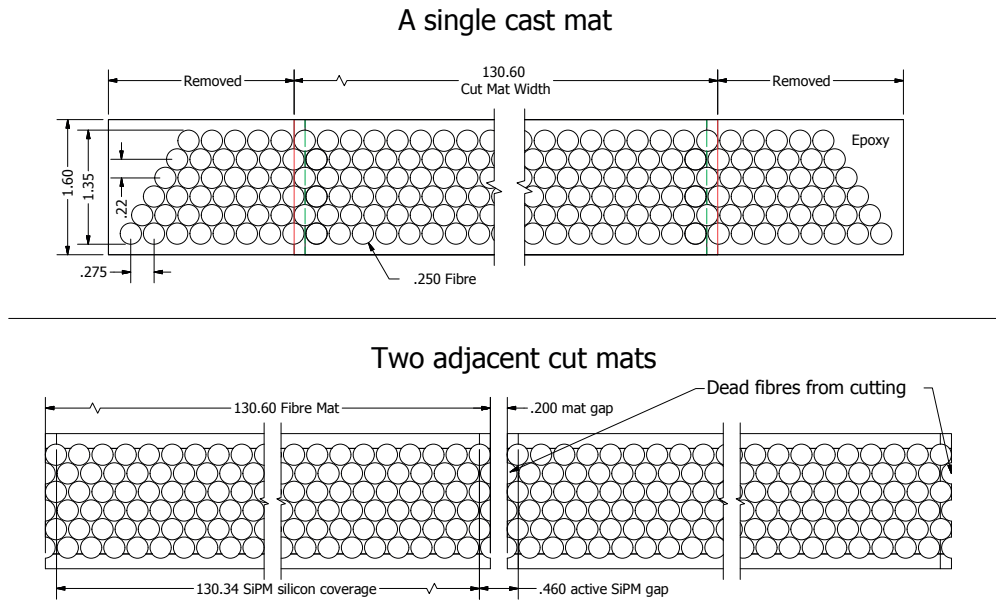


Figure 3.11: Schematical view of a 6 layer SciFi mat for LHCb. Image taken from [32].

### 3.5 SciFi modules

The module of the fibre tracker consists of fibre mats (detection layer), support structures, photodetectors, cooling systems and readout electronics.

**Fibre mats:** The scintillating fibre mat is the detection element of the SciFi tracker and needs to be manufactured with high mechanical accuracy. The fibres are arranged in mats of six layers. The number of layers has been optimised to achieve sufficient light yield while keeping the material budget low. To produce the mats, a threaded winding wheel ( $d=86$  cm) with a pitch of 0.275 mm is used. A layer of fibres is formed by laying down the fibres on the wheel turning at a speed of  $\sim 1$  tps. The accurate placement of the first layer is guaranteed by the thread of the wheel. Each additional layer uses the last layer as a positioning guide. To stabilise the fibres, a thin layer of glue loaded with  $\text{TiO}_2$  is applied [32]. A schematic cut view of the fibre mat is shown in Fig.(3.11). A machine has been developed to produce the mats, controlling the speed, the fibre tension and positioning.

After winding, series of steps for stabilisation, light shielding and flattening the mats are performed. The fibre mat is cut at each side with a diamond tool to obtain a high quality optical surface. On one end of the fibre mat, a high reflectivity mirror is glued. The finished mat is 2.42 m long and 130.65 mm wide.

**Modules:** A fibre module is the assembly of multiple fibre mats onto a support structure. An over-view is shown in Fig.(3.12). Each of the 12 detection planes of the tracker is composed of

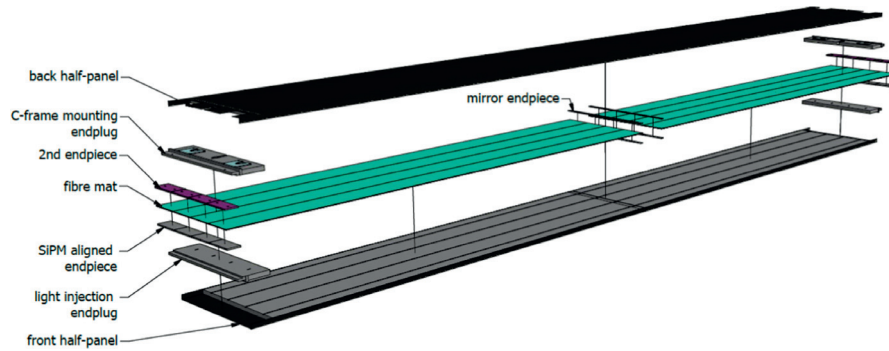


Figure 3.12: Exploded view of module assembly. Image taken from [31].

12 modules. The fibres mats are sandwiched between two low material budget honeycomb structures. Two end-plugs are glued and provide either the light injection system foreseen for calibration or the mounting interface to the readout box.

**Readout box:** It is composed of the cold box, hosting the SiPM and the SiPM cooling system and the front-end electronic support holding the boards with the front-end, the clusterisation boards and the master board, as explained in the next section.

The cold box provides the SiPM cooling through a 3D-printed titanium bar connected to a liquid chiller. The SiPM arrays are glued on this cooling pipe after optical alignment. A spring loaded mechanism ensures good optical contact between the SiPM and the fibres.

### 3.6 Readout electronics and data processing

The readout electronics is composed of the front-end and back-end electronics. The data processing flow is also presented.

#### 3.6.1 Front-end electronics with the PACIFIC chip

The front-end boards are located in the warm part of the readout box. They process the SiPMs signals and provide the interface to the data-acquisition system [14]. The PACIFIC (low-Power Asic for the SCIntillating FIBre TraCker) front-end ASIC was developed and optimised for the readout of the LHCb SciFi Tracker. One PACIFIC chip can read 64 SiPM channels. After amplification, shaping and integration, the signal is digitised with only three comparators providing a 2-bits digital output. A pole-0 cancellation circuit adapted to the SiPM signal shape is used to obtain a fast signal shaping.

In a second step the signal is integrated over 25 ns. The digitisation is performed by applying a set of three configurable thresholds. The PACIFIC channel architecture is illustrated in Fig.(3.14).

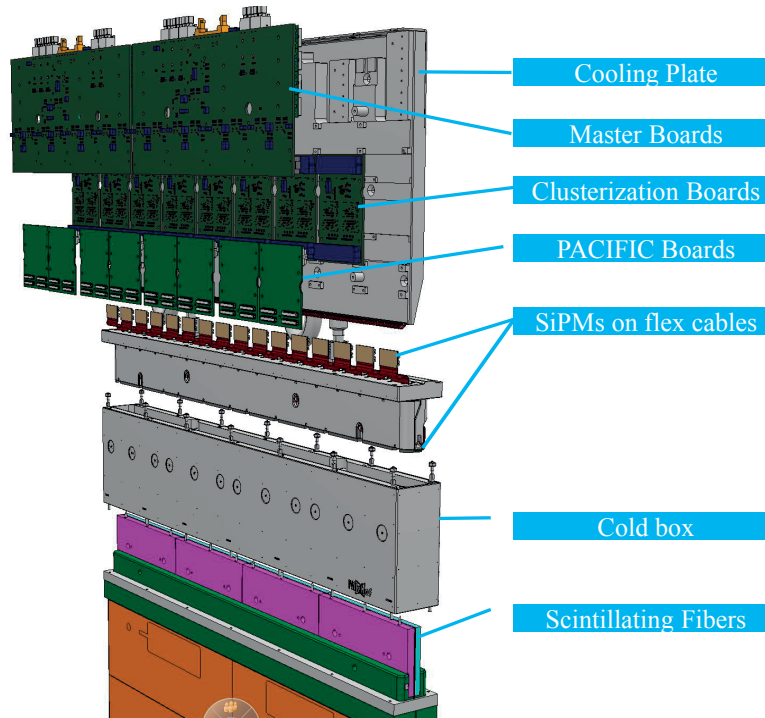


Figure 3.13: Over-view of the readout box including module, end piece, coldbox and electronics on a cooling frame. Image taken from [35].

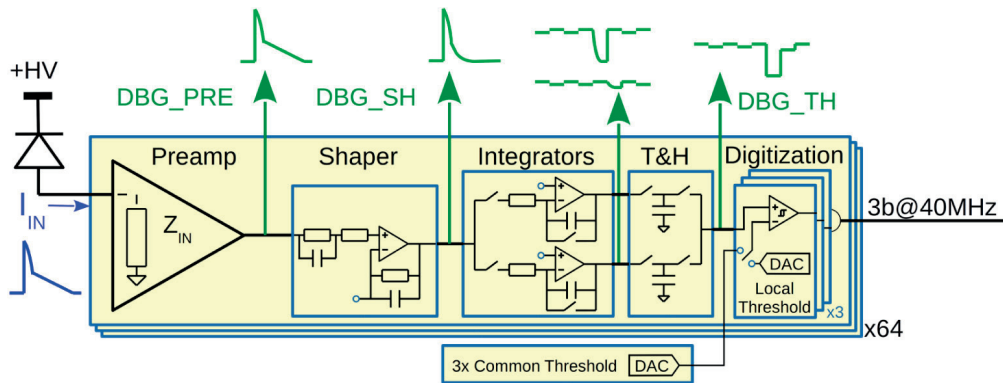


Figure 3.14: Scheme of a PACIFIC channel architecture. Image taken from [36].

The outputs of four PACIFIC chips are collected by an FPGA that applies a clustering and zero suppression algorithm (Sec.3.6.2). The cluster data is collected and sent to the master board where the communications with the back-end electronic via optical links is made [36]. The architecture of the SciFi front-end follows the electronics architecture defined for the LHCb Upgrade [37]. A functional block diagram can be seen in Fig.(3.15).

Each front-end board also provides the bias voltage to all SiPM channels. For gain adjustment of the SiPMs, the front-end ASIC provides channel individual bias voltage adjustment over a

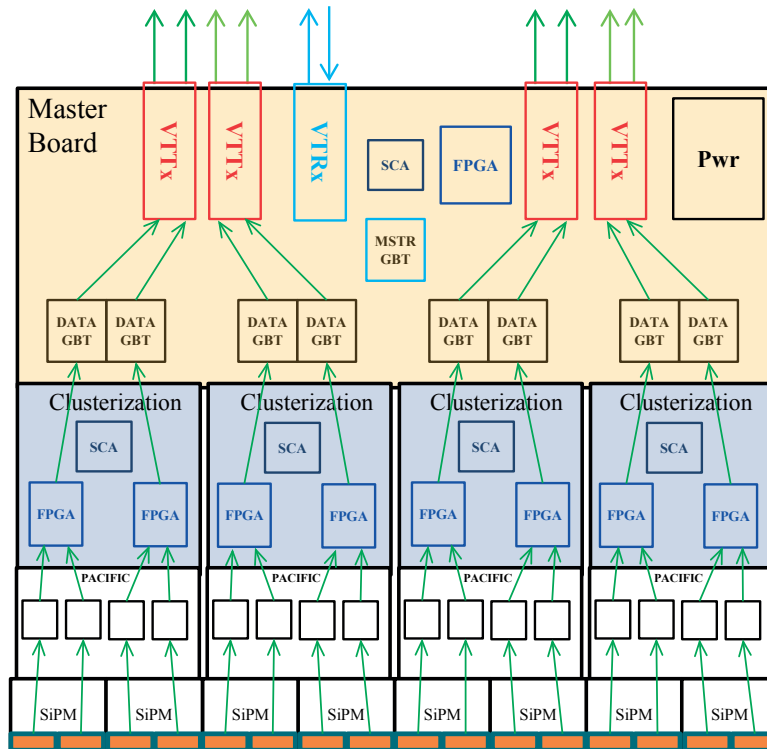


Figure 3.15: Functional diagram showing the data flow in the FE electronics. It corresponds to half a readout box. The data flow is denoted by the green line. Image taken from [35].

range of 600 mV (50 mV steps) [38, 39].

### 3.6.2 Data processing and clustering

The light produced by charged particles is spread over several SiPM channels. For an optimal zero suppression and noise reduction, the signals are assembled into clusters. The centre-of-gravity of the cluster is used to obtain the hit position estimate.

In the following, two different clustering algorithms are described. For the readout in LHCb, where only 2-bit information is available the algorithm is called "2-bit". For the characterisation and light output measurements of SciFi modules, the electronics provide 10-bit data. The clustering algorithm is then called "10-bit" [40].

**The 10-bit clustering algorithm:** It is based on multiple thresholds defined as following:

**Seed threshold** In a first step, the seed threshold is applied to find cluster candidates.

**Neighbour threshold** In a second step all neighbouring channels to the candidates are included if the neighbour threshold is reached.

**Sum threshold** A cluster is confirmed if the charge of the cluster is above the sum threshold.

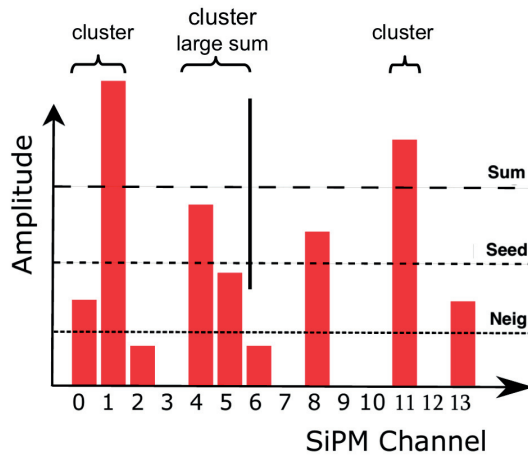


Figure 3.16: The 10-bit clustering algorithm.

The standard values for the thresholds for the LHCb SciFi are (neighbour threshold, seed threshold, sum threshold) = (1.5,2.5,4.5) for neighbour, seed and sum.

**The 2-bit clustering algorithm:** It is similar to the 10-bit algorithm described above. Due to the limited information on the amplitude of each channel, the sum cannot be calculated. As a replacement, a high threshold is introduced to allow the selection of large single channel signals. This basic algorithm has astonishingly almost the same performances as the 10-bit. The set of three thresholds can be described as following:

**1st threshold** This threshold is the equivalent of the neighbour threshold. All channels above the 1st threshold are candidates for inclusion into a cluster.

**2nd threshold** Takes the same role as the seed threshold.

**3rd threshold** Channels matching this threshold are sufficient to form a cluster.

Two conditions can lead to a cluster:

1. A channel has reached threshold 3.
2. At least one channel has reached threshold 2 and at least one threshold 1 in addition.

The encoding scheme is shown in Fig.(3.17).

### 3.6.3 Back-end electronic

The data sent by the front-end boards through the optical links are received and processed by the back-end electronic (TELL40 boards). Each TELL40 can handle 24 optical links and features up to 12 optical link outputs to the DAQ CPU farm [14].



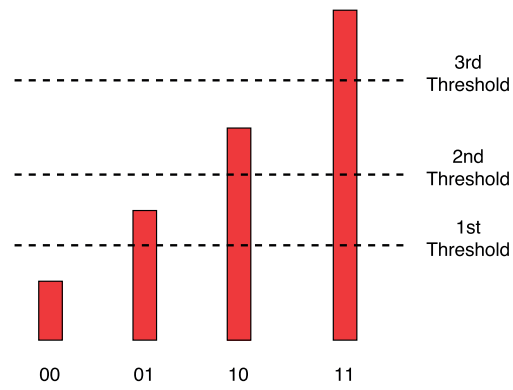


Figure 3.17: 2-bit signal encoding. "00" = noise and below all threshold, "01" = first threshold reached, "10" = second threshold reached and "11" = third threshold reached.



## 4 Photodetectors

Specialised photodetectors like the SiPMs considered in this thesis, are widely used in many variations for scientific, industrial, and medical applications. For high energy physics applications, the light sources are scintillators (Sec.(3.3)) or Cherenkov radiators. The most common detectors are sensitive to the wavelength range of 100 to 1000 nm. A photodetector converts incident photons to electric signals. The small signals generated is often amplified directly on the device. A gain of  $10^6$  is typically needed when single photon detection capability is required. The detection process involves [41]:

1. Generation of electrons, called photoelectrons (PE), by photoelectric effect. This process is detailed in Sec.(4.1).
2. Amplification by an electron multiplication process, e.g. high electric field (avalanche) or acceleration of electrons in vacuum.
3. Signal collection and electronic amplification.

A few definitions used for photodetectors are given below [41, 24]. The quantum efficiency (QE) is defined as the probability for an incident photon to generate a PE. The radiant sensitivity, or responsivity, is often used for photodetectors. It correspond to the output current I divided by the incident power P and G the gain of the detector. It is defined as:

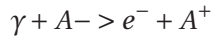
$$S_k[\text{mA/W}] = \frac{I[\text{mA}]}{P[\text{W}] \cdot G} = \frac{\text{QE}[\%] \cdot \lambda[\text{nm}] \cdot e}{G \cdot hc} = \frac{\text{QE} \cdot \lambda}{G \cdot 124} \quad (4.1)$$

The photo detection efficiency (PDE) combines the QE and the probability of the PE detection. As an example for SiPMs the PDE is given by  $\text{PDE}[\%] = \text{FF} \times \text{QE} \times P_{\text{Avalanche}}$  with FF the fill factor (ratio between the active and total area of the detector) and the avalanche probability for a single electron to trigger an avalanche.

### 4.1 Light interaction in matter

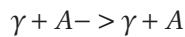
The most common interactions of light with matter are the following:

- **The photoelectric effect:** An incident photon absorbed by an atomic electron receives sufficient energy to escape the atom.



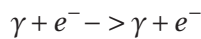
The ejected electron, in the detector context, is called "photoelectron" and has an energy of:  $E_e = h\nu - E_b$  with  $E_b$  the binding energy of the electron. This effect occurs when  $h\nu > E_b$ .

- **Rayleigh scattering or coherent scattering:** Elastic scattering of an incident photon by an atom.



The photon wavelength is almost unchanged.

- **Compton scattering:** The photon is scattered by the electron and part of its energy is transferred to the electron resulting in a deposit of ionisation energy.



- **Pair production:** The incident photon has sufficient energy to create electron-positron pair in the presence of the electromagnetic field of the nucleus.



The competing processes dominate at a different photon energy. The processes cross-sections in silicon for an energy range of 1 keV to 1 MeV can be seen in Fig.(4.1) . For visible light, the photoelectric effect and Rayleigh scattering are dominant (energy range of few electron-volts).

Two types of photoelectric effect can be distinguished:

- External photoelectric effect: where electrons are extracted from a surface by the energy of the incident photon. This effect is seen at the photocathode of photomultipliers.
- Internal photoelectric effect: where, in a semi-conductor, electrons are moving from the valence band to the conduction band by incident photon energy (change in energy state). Examples are photodiodes.

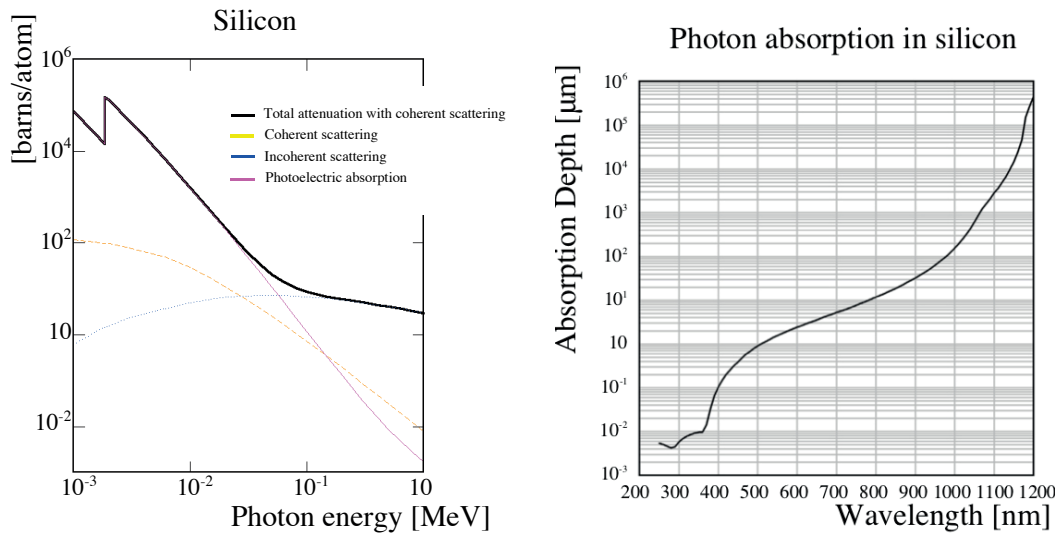


Figure 4.1: Left shows the total interaction cross section of photons in silicon. The contribution of each process is shown. Charts and data from XCOM database, courtesy of NIST [42]. Right shows the photon absorption depth in silicon as a function of the wavelength [43].

## 4.2 Vacuum based photodetectors

Vacuum photodetectors are based on the external photoelectric effect followed by an amplification stage.

### 4.2.1 Photomultiplier tubes (PMT):

A PMT is a vacuum tube consisting of an input window, a photocathode, a focusing electrode, an electron multiplier and an anode as shown in Fig.(4.2).

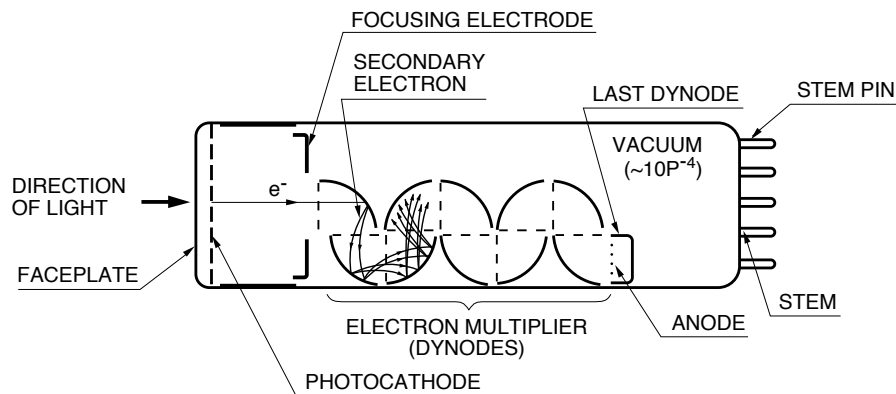


Figure 4.2: Illustration of a PMT. Image taken from [44].

The light entering the entrance window hits the photocathode. Electrons are ejected from the photocathode through external photoelectric effect. The freed electrons are accelerated and

## Chapter 4. Photodetectors

focused onto the first dynode and multiplied by secondary electron emission. Several dynode staggers to reach a gain of  $10^5 - 10^6$ . At the end of the multiplication chain, the electrons are collected by the anode. The gain of PMTs depends on the high voltage  $V$  applied and is given by:  $G = AV^{kn}$  where  $k \approx 0.7 - 0.8$  (depending on the dynode material),  $n$  is the number of dynodes and  $A$  is a constant. The Poisson statistical fluctuations on the 1st dynode dominate the amplification process. The pulse rise time can be less than one nanosecond. PMTs are unsuitable for applications in magnetic fields.

### 4.2.2 Hybrid photodetectors (HPD):

The HPD detector is a vacuum tube consisting of a photocathode, an accelerating region and a semiconductor diode [45]. The amplification is composed of an electron bombardment region and an APD (Sec.(4.4)) with a typical gain of  $10^5$  [46]. An illustration can be seen in Fig.(4.3).

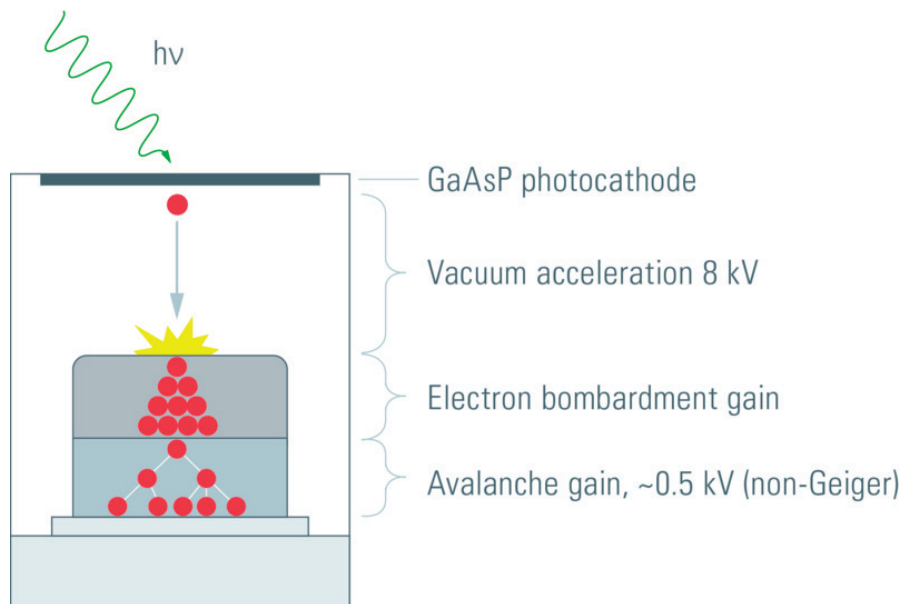


Figure 4.3: Scheme of a HPD: a photoelectron is released from the cathode upon interaction with a photon. This electron is accelerated by a high voltage and its energy dissipated in the semiconductor target. Electron bombardment creates many electron-hole pairs (first amplification). In a subsequent avalanche diode, these charges are multiplied (second amplification). Image taken from [47].

HPDs combine the sensitivity of PMTs (photocathode) with the spatial resolution of Si-detectors. In contrary to PMTs, HPDs have a low statistical fluctuation in gain due to the high amplification on the bombardment stage. On the other hand HPDs are also sensitive to magnetic fields.

An example application of HPDs are the Ring Imaging Cherenkov detector at LHCb [48, 49]. These HPDs have a diameter of 83 mm diameter with a photocathode sensitive region of 75 mm. Although the photodetectors are shielded against the magnetic field, a maximal field

of  $\sim 50$  mT can be tolerated.

#### 4.2.3 Microchannel plates (MCP):

MCP detectors consist of a thin glass plate perforated with a large number of holes with typical diameter of  $10\ \mu\text{m}$ . The glass plate is inserted between a photocathode and an anode plane. The inner surface of each capillary acts as a continuous dynode. A multiplication is obtained in the glass capillaries. For single channel MCPs, the typical gain is in the range of  $10^3 - 10^4$  [50]. MCPs are thin, offer good spatial resolution and reach an excellent time resolution ( $\sim 20$  ps) but they suffer from relatively long recovery time. They can tolerate up to 1 T magnetic field but show serious aging problems [41].

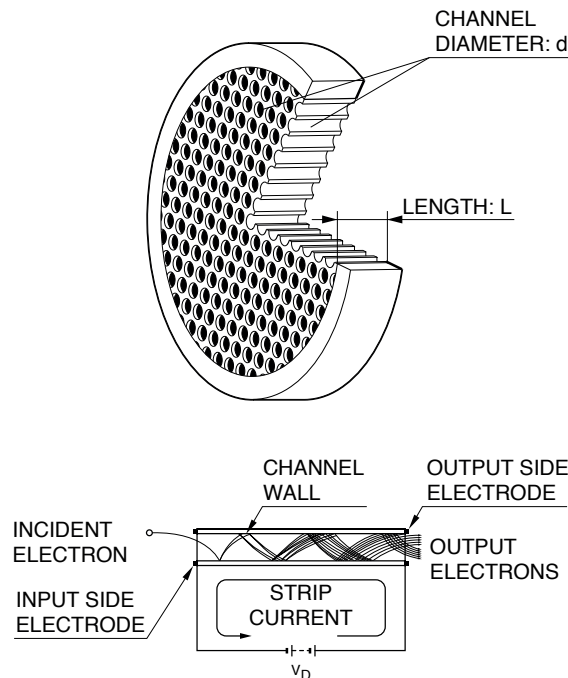


Figure 4.4: Scheme of an MPC: a photoelectron is released from the cathode and is multiplied in the glass channel. Image taken from [51].

### 4.3 Gaseous based photodetectors

In gaseous photomultipliers, the avalanche takes place in a gas under a high electric field. They can be divided into two types depending on the material of the photocathode. One type is based on solid photocathode materials, similar to PMTs and the other type on gases. Most of the gases have photoionisation work functions<sup>1</sup> above 10 eV which limits their wavelength sensitivity. However, gases like tetrakis dimethyl-amine ethylene (TMAE) or tri-ethyl-amine (TEA) have smaller work functions (5.3 eV and 7.5 eV respectively) and are suited to UV photon

<sup>1</sup>The work function of a gas is the average energy required to create one electron-ion pair

detection. Gaseous based photodetectors are insensitive to high magnetic fields, are relatively inexpensive and therefore often used in large area detectors. The typical applications are RICH detectors [41].

### 4.4 Solid-state photodetectors

Solid-state photodetector are more compact, magnetic field tolerant, allow fine granularity and can be operate at low voltage. On the other hand, they have temperature dependent gain/noise and suffer from dark noise. Different solid-state photodetectors are described below.

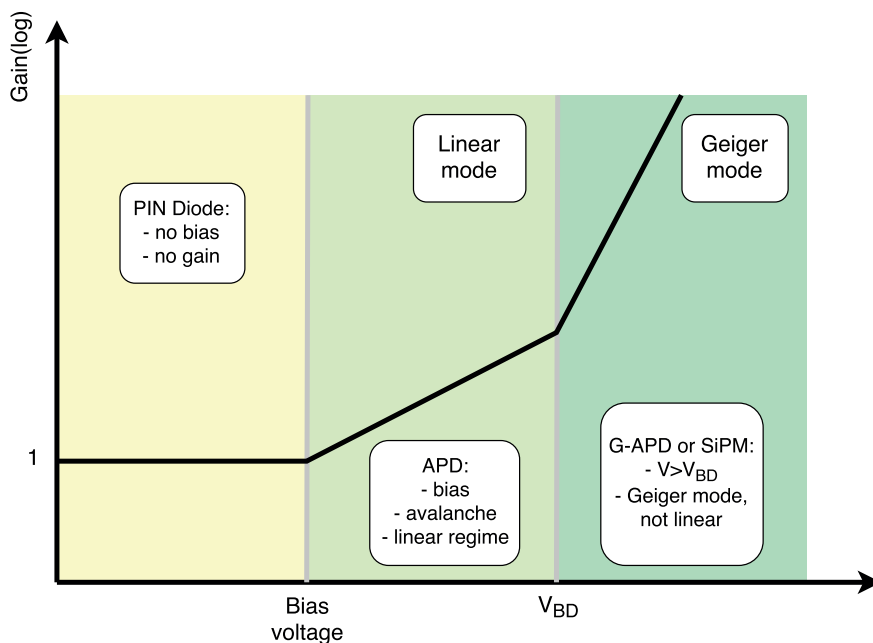


Figure 4.5: Gain regime for different solid-state photodetectors. For PIN diodes gain = 1. APDs can be operate in either a linear regime where the gain increases exponentially with the voltage or in Geiger mode (G-APD).

#### 4.4.1 PIN diodes:

PIN diodes are the simplest form of reverse biased  $p - n$  junctions [52]. A p-type semiconductor contains a large concentration of holes with few electrons and n-type contains a large concentration of electrons with few holes.

At a  $p - n$  junction, holes from the p-side diffuses into the n-side and electrons from the n-side diffuse into the p-side. The charge separation in the  $p - n$  region generates an electric field directed from the n-side to the p-side. An equilibrium is reached between the electric field and the diffusion and a zone without free carriers called depletion region is formed. In the depletion region, acceptor and donor ions are left without their opposite charged free charge



carriers as shown in Fig.(4.6).

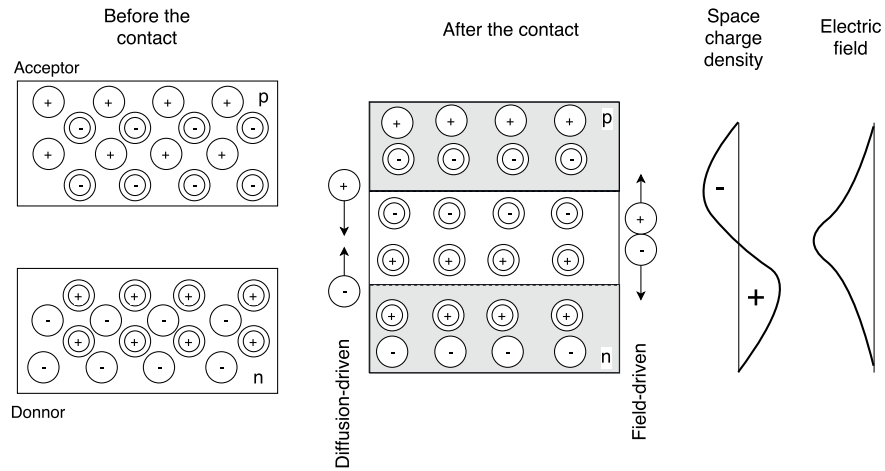


Figure 4.6: Scheme of a  $p - n$  junction with the depletion region.

Applying an external voltage in the same direction as the induced electric field increases the depth of the depletion zone. In this case the junction is reverse biased.

For the PIN diode, an intrinsic region (i.e. undoped) is produced between a high doped p and n-regions. Applying a reverse bias voltage allows to increase the thickness of the depleted region. A thicker depletion layer allows to enhance the sensitivity to larger wavelength (red, infrared). An illustration of a PIN diode can be seen in Fig(4.7).

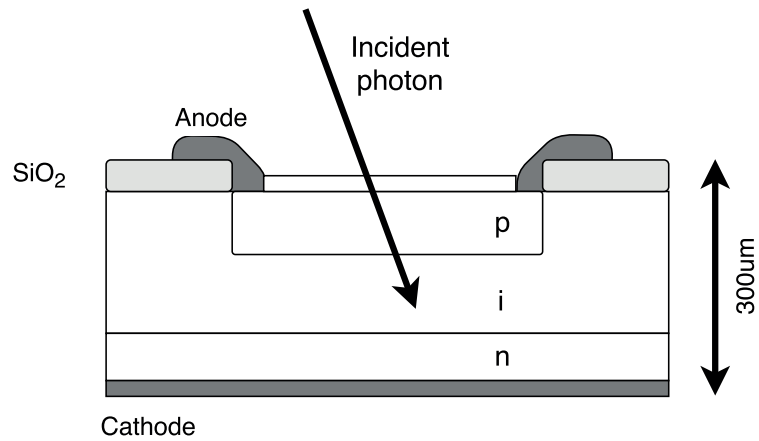


Figure 4.7: Illustration of a PIN diode cross-section.

Photons with  $E > E_{\text{Bandgap}}$  can be absorbed in the depletion region and create electron-hole pair. They drift to the anode and cathode. The drift of charge can be detected as a small current called the photocurrent.

PIN diodes have a very high QE (up to 80%), are insensitive to magnetic field and temperature

changes due to the absence of gain. The PIN structure in radiation suffers from surface and bulk damages. Surface damages are caused by ionising radiation. It induces charge build-up and QE losses. The dominating damage is bulk damage caused by the radiation from neutrons and charged particles. Bulk damages increases the dark current due to the displacement of the lattice atoms. These two effects are common to any silicon detector.

They are widely used for gain monitoring system for calorimeters and their spectral sensitivity is well matched to most scintillators. The drawback of PIN diodes is the very small signal. Single photon counting cannot be achieved with PIN diodes. They are also used for neutron radiation monitoring [53]. The equivalent 1 MeV neutron fluence  $\Phi_{eq}$  can be obtained from the diode's forward voltage at 25 mA. Typically the voltage from a 50 ms current pulse is measured to avoid heat-up of the device (annealing of the radiation defects).

### 4.4.2 Avalanche photodiode (APD):

In addition to the photocurrent generation as described for the photodiodes, APDs offer a multiplication of the generated carriers. A high electric field present in the so called multiplication region produces a high drift speed of the carriers. Only if the electric field is high enough, the carriers that escape collisions with the crystal lattice exhibit sufficient energy to generate a new electron-hole pair. An ionisation chain reaction takes place, known as the avalanche multiplication. As a result, a small but detectable signal is obtained. The depth at which the primary carriers are generated depends on the wavelength of the incident light. Different structures are implemented according to the wavelength to be detected [54]. Electron-hole pairs can also be produced by the passage of ionising radiation within the APD, called Nuclear Counter Effect [55].

An excellent junction uniformity is critical. A guard ring is added as protection against edge breakdown. The gain is typically 10-200 in linear mode and up to  $10^8$  in Geiger-Müller mode (G-APD). In linear mode operation, a close monitoring and stability of the temperature is necessary [41]. APDs operated in Geiger-Müller mode exist as single pixel detector (S-PAD) or as multipixel devices (SiPM Chap.(5)). An illustration of the avalanche multiplication inside an APD can be seen in Fig.(4.8).

APDs have a wide range of applications. In the CMS experiment [56] ECAL, they are located inside the super-conductive magnet, so they [57, 58]:

- Operate in strong magnetic field of about 3.8 T.
- Need an internal amplification due to low light yield.
- Need a large dynamic range, particles deposit energy between 40 MeV up to 2 TeV.
- Are operated in heavy radiation environment. The neutron fluence is of  $\sim 10^{13} - 10^{14}$  n/cm<sup>2</sup>.

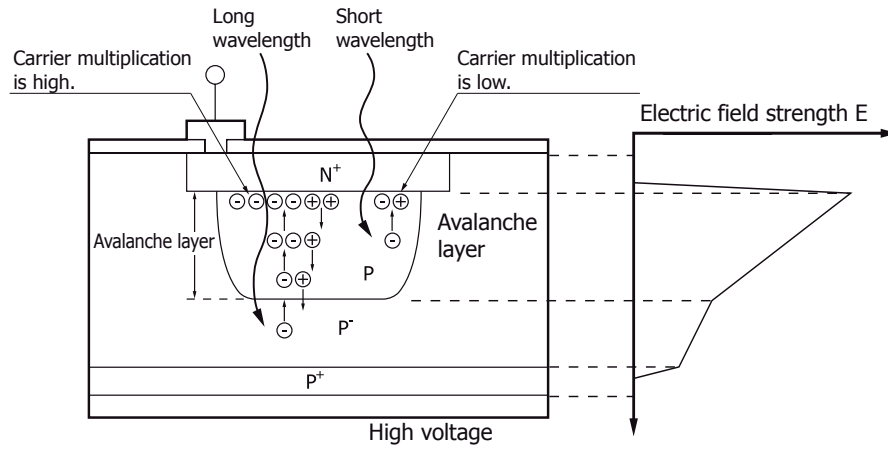


Figure 4.8: Schematic diagram of avalanche multiplication process (near infrared type). Image taken from [54].

APD from Hamamatsu with a customised silicon implementation were developed to reach the requirements.



## 5 SiPM characteristics and motivation for LHCb

SiPMs are photon-counting devices using multiple APD pixels operated in the Geiger-Müller mode. They feature high gain, high photo detection efficiency in the visible light spectrum, fast signal response, good time resolution, insensitivity to magnetic field and are robust against high illumination (no "burn-in" effect as for MCP). The main application is low light detection with a maximum of about  $10^5$  photons per event.

### 5.1 SiPM technology

SiPMs are arrays of APD micro pixels operated in Geiger-Müller mode. The operation principle of the APD is based on a reverse bias voltage ( $V_{\text{Bias}}$ ) such that an avalanche produced has a linear relationship between the number of primary electron-hole pairs and the total photocurrent. The avalanche process is localised and the process is automatically stopped once no primary electron-holes are present. The SiPM operation is with an even higher  $V_{\text{Bias}}$ , where a non-linear regime is reached (Fig.(4.5)). The avalanche extends to the full pixel volume (avalanche region) and the total charge present in the signal,  $Q_A$ , displays a linear dependence,  $Q_A \propto \Delta V = V_{\text{Bias}} - V_{\text{BD}}$ , where  $V_{\text{BD}}$  is the voltage necessary to start the process of a self-sustained avalanche known as breakdown voltage.  $\Delta V$  is called the "overvoltage". The process is extremely fast, in a sub-nanosecond range. To stop the avalanche, called "quenching", a voltage drop below  $V_{\text{BD}}$  is required [59]. In Fig.(5.1) a schematical view of the connection of an SiPM is shown. All micro pixels are connected to a common bias through independent quenching resistors ( $R_Q$ ). The role of  $R_Q$  is to quench the avalanche. These resistors are implemented as poly-silicon or, by Hamamatsu, as transparent metal thin film. Metal thin films are partially transparent and therefore allow for higher fill factor. Thin films are three times less temperature dependent than polysilicon. Another possibility is to use bulk integrated resistors which is a technology still under development. The output signal is the analogue sum of all individual pixel signals and is proportional to the number of detected photons. If multiple photons hit the same pixel, only the signal of one photon is measured. Note that the hit position is lost for the single pixel.

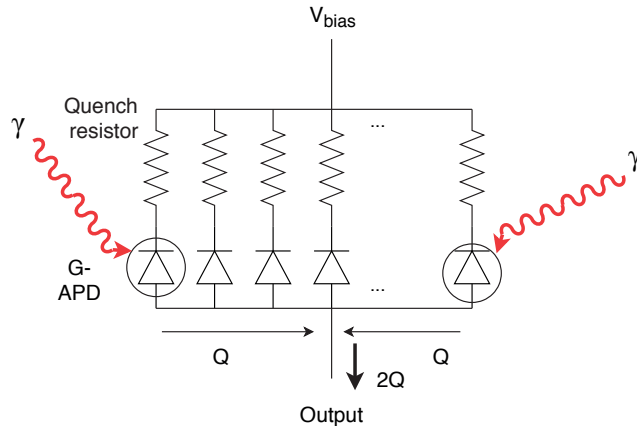


Figure 5.1: G-APD cells in parallel (SiPM pixels). Resulting signal at the output is the sum of all fired G-APD cells.

Depending on the wavelength to be detected, the micro-cells profile can have two types of implementations because electrons have a higher probability than holes of triggering an avalanche. A better efficiency is achieved when the photon interacts in the p-type layer [43]. For the blue/UV light with a short attenuation length in silicon, the PE is generated just beneath the surface. To reach the avalanche region the PE has to drift toward the avalanche region below. If the absorption takes place in the highly doped top layer, the electron-hole pair has a large probability to be lost due to the short recombination time. A p-on-n implementation is required to be efficient. Lower energy photons, which have long attenuation length, are absorbed in the bulk or even traverse the detector without interaction [60] and requires a n-on-p structure to be efficiently detected. To improve green light sensitivity, an additional epitaxial layer can be implemented between the p-doped entrance window and the n-substrate as shown for a KETEK detector in Fig.(5.2).

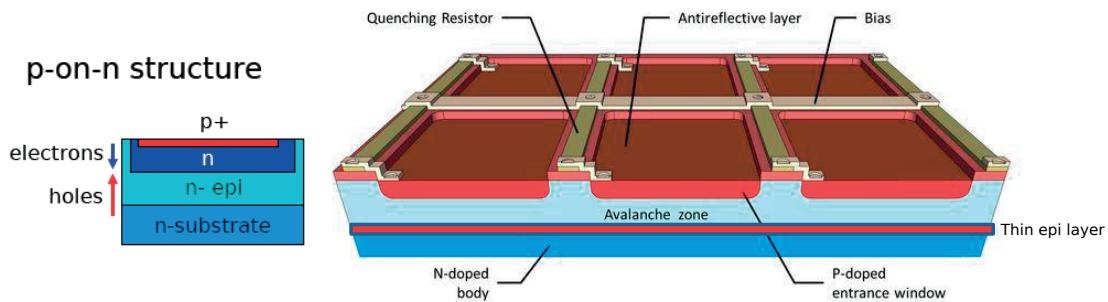


Figure 5.2: KETEK SiPM silicon implementation.

In addition to the improved green sensitivity, the epitaxial layer also lowers the gain of devices which has beneficial effects for pixel recovery time and noise.

### 5.1.1 Electrical SiPM models

Two equivalent SiPM electrical models are presented. Considerations on the avalanche quenching are also made.

#### Basic electrical model

The G-APD cell can be modeled with an equivalent electrical circuit and two probability functions [61, 62]. The following parameters are defined:

- $C_d$ : the diode capacitance.
- $R_S$ : the series resistance.
- $R_Q$ : the quenching resistance.

The basic electrical model is presented in Fig.(5.3). The rise time  $\tau_d$  is given by the product of the series resistance ( $R_S$ ) with the diode capacitance ( $C_d$ ) and is in the order of  $\sim 100$  ps.

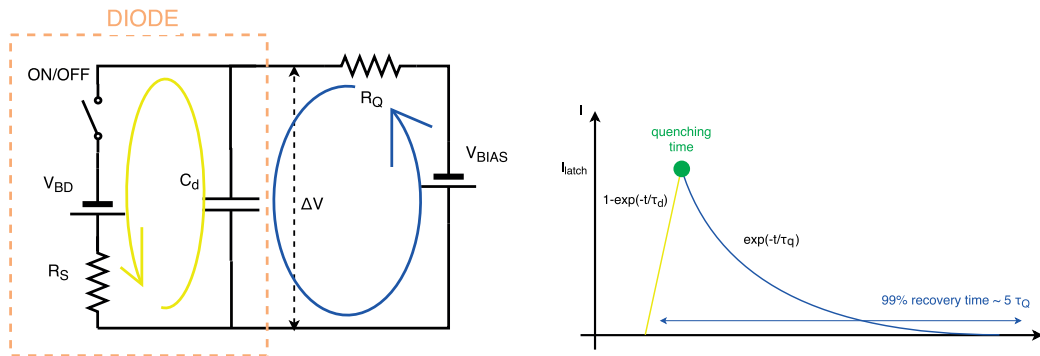


Figure 5.3: Basic SiPM electrical model (left) and its resulting pulse shape (right).

The fall time ( $\tau_q$ ) is given by the product of  $R_Q$  and the diode capacitance ( $C_d$ ). The typical range of  $\tau_q$  is between 10 to 200 ns depending on the quenching resistor value. The figure also shows the pulse shape from this basic model and the current generation follows the scheme of Fig.(5.4):

- $P_{01}$ : is the probability that an avalanche is triggered.
- **On condition**: the switch is closed,  $C_d$  discharges to  $V_{BD}$  with a time constant  $R_S \times C_d = \tau_d$  which produces a current  $\Delta V / (R_Q + R_S) \approx \Delta V / R_Q$ .
- $P_{10}$ : is the probability that the avalanche is stopped.
- **Off condition**: the switch is open and the capacitor is re-charged to  $\Delta V$  with a time constant of  $R_Q \times C_d = \tau_{rec}$  (recovery time).

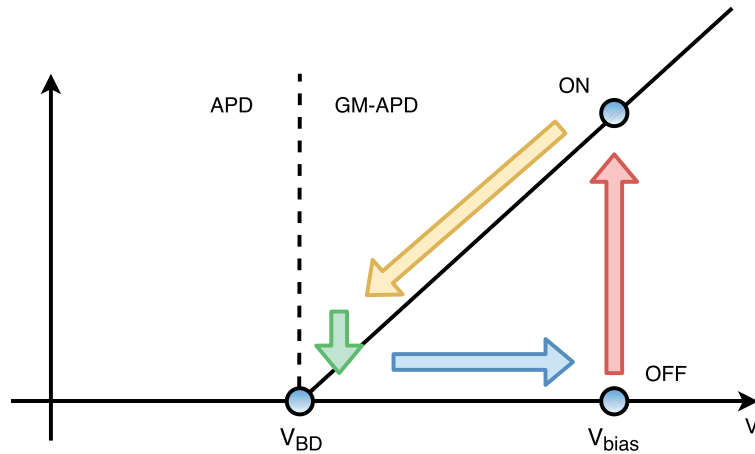


Figure 5.4: SiPM current generation steps. Image taken from [61].

The avalanche may be quenched by statistical fluctuations if the quench resistor is high enough. To allow a sub-nanosecond quenching time, the value of  $R_Q$  needs to be chosen properly.

The possible  $\Delta V$  operation is in the range:  $0 < \Delta V < R_Q I_{latch}$  where  $I_{latch}$  is about  $20 \mu A$ . For a given  $R_Q$ , this leads to a  $\Delta V_{max}$  value of a few volts.

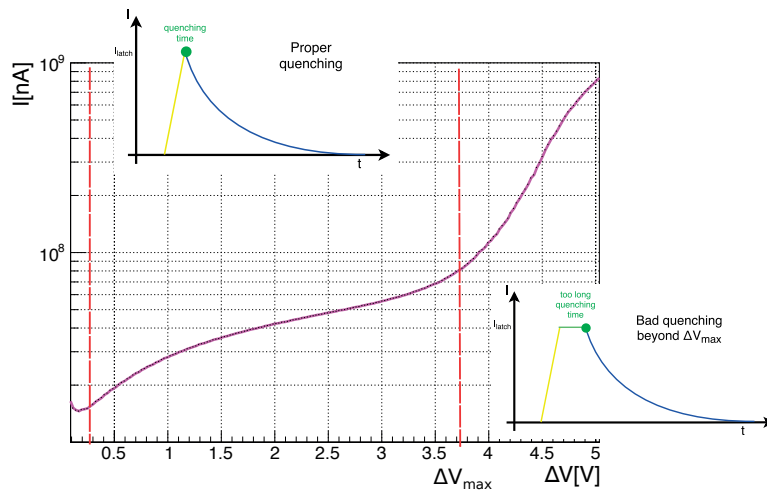


Figure 5.5: Illustration of the effect of a bad avalanche quenching when the SiPM (here a KETEK detector) is operated above  $\Delta V_{max}$ . For  $\Delta V$  above 3.5 V the effect of the bad quenching on the reverse IV characteristic is shown. The quenching time is too long. This effect is also referred as incomplete quenching. Image taken from [61].

The recovery time is temperature dependent through the  $R_Q$  variation. For a given  $\Delta V$ , the gain is simply  $G=C_d \cdot \Delta V$ .



**Detailed electrical model**

In modern SiPMs, a capacitor  $C_q$  parallel to  $R_Q$  is implemented to obtain a fast second decay component in addition to the long component already present in the basic model. This requires an extension of the model, Fig.(5.6). The model comprises the firing pixel, the  $N-1$  connected inactive pixels and a parallel grid capacitor representing the capacitance present due to the routing of pixels connections. A load resistor of  $50\ \Omega$  is added.

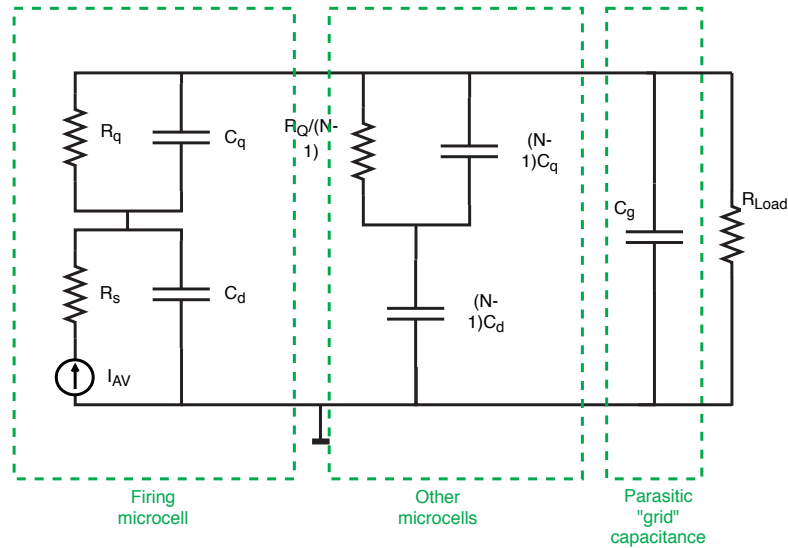


Figure 5.6: SiPM high frequency equivalent electrical circuit.

The current resulting from the avalanche of a firing cell has a typical rise time variation of about 100 ps and is given by  $\tau_d = R_S \times (C_q + C_d)$ .

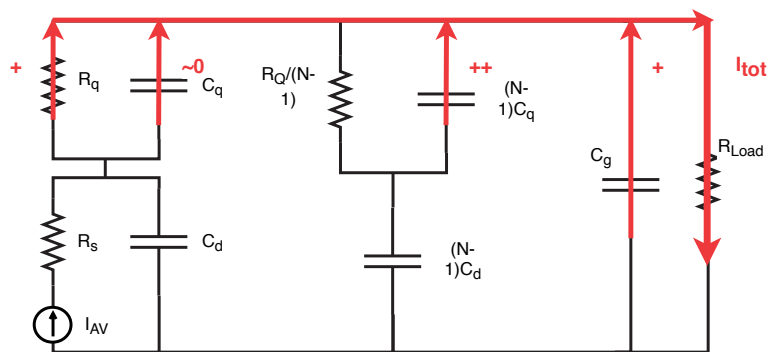


Figure 5.7: Current of the fast component flowing through  $R_{Load}$ .

The fast component delivered into the load resistor is the sum of the current delivered by the non-firing pixels and the current from  $C_g$ . The current from  $C_q$  (firing pixel) is neglected. The time for the fast component is typically from 2-3 ns.

The current for the long component is delivered by  $C_d$  and  $C_q$  of the fired pixel and is "slow"

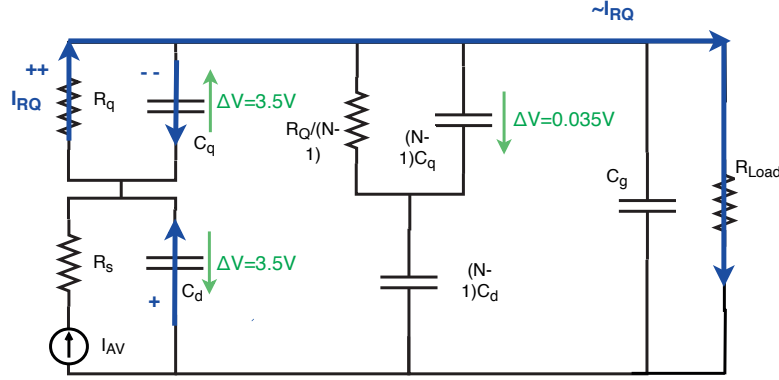


Figure 5.8: Current of the slow component flowing through  $R_Q$

because it is flowing through  $R_Q$ .

- $\tau_{short} = R_{load} \times C_{tot}$  with  $C_{tot} = C_d \times N_{pix} + C_g$  the total detector capacitance and  $R_{load}$  is typically  $50 \Omega$
- $\tau_{long} = R_Q \times (C_q + C_d)$ . Unlike the model, measurements show that  $\tau_{long}$  is better given by  $\tau_{long} = R_Q \times C_d$ .

The gain is:

$$G = Q/e = \frac{\Delta V(C_d + C_q)}{e} = \int dt \frac{V(t)}{e \cdot R_{load}} \quad (5.1)$$

Typical values for H2017 can be seen in Tab.(5.1):

H2017	
$C_d$	136 fF
$C_q$	34 fF
$R_Q$	525 k $\Omega$
G	$1.05 \cdot 10^6 V^{-1}$

Table 5.1: Typical SiPM values for model H2017 by Hamamatsu

## 5.2 Main characteristics of SiPMs

In this section the main parameters of an SiPM are detailed. The adopted characterisation methods are exposed in Chap.(6).

### 5.2.1 Temperature dependency of the breakdown voltage

The breakdown voltage,  $V_{BD}$ , is strongly temperature dependent<sup>1</sup> and is usually given for a temperature of 25°C. The temperature coefficient is defined as the  $V_{BD}$  change for 1°C. To obtain the  $\Delta V$  a good knowledge of  $V_{BD}$  is necessary. Many important characteristics as photo detection efficiency, noise or gain depend of  $\Delta V$ .

### 5.2.2 Gain

The gain of an SiPM is defined as the charge released by a photoelectron (PE) in an avalanche divided by the electron charge. It is independent of the primary source of the avalanche (a photon or a thermal avalanche). The gain is proportional to  $\Delta V$  and to the sum of  $C_d + C_q$  as defined in the model Sec.(5.1.1), and can be expressed in units of elementary charge  $G = \Delta V \cdot (C_d + C_q) / e$ . Typical values for a detector with  $(50 \mu\text{m})^2$  pixels are  $1 \cdot 10 \cdot 10^6$  at  $\Delta V = 1-7 \text{ V}$ . In the following  $G/\Delta V$  is used which has the dimension  $\text{V}^{-1}$  and only depends on detector capacitance. The detector capacitance  $C_d + C_q$  is dominated by  $C_d$  which is the pixel capacitance proportional to the pixel active surface and inversely proportional to the avalanche region thickness. It therefore allows to compare the avalanche region thickness of different devices and technologies.

### 5.2.3 Correlated and uncorrelated noise

In the pulse-shape analysis and noise characterisation, all pulse amplitudes are conveniently expressed in the unit of PE, as all detected photons generate pulses of the same amplitude. The 1 PE pulse amplitude  $A_{1PE}$  is extracted from the amplitude distribution of single photon pulses. A Gaussian fit is performed. The SiPM noise is categorised into correlated and uncorrelated noise.

#### Correlated noise

"Correlated" means that noises pulses are associated with an initial dark or light pulse. Three types of correlated noise are distinguished:

**Direct optical pixel-to-pixel cross-talk (DiXT):** Infrared photons are generated in a pixel when an avalanche is produced. The infrared photons may travel to a neighbouring pixel and create a secondary avalanche. This phenomenon is called optical pixel-to-pixel cross-talk and results in pulses produced simultaneously (or with a small time delay of the order of a few 100 ps) with respect to the primary pulse. For instantaneous cross-talk, the peak amplitude can reach 2 PE whereas with a small delay it is between 1 and 2 PE, as it can be seen in the left plot of Fig.(5.10). Higher amplitudes are possible due to

---

<sup>1</sup>A temperature increase makes the crystal lattice vibrations increase and slow down the charge carriers, reducing the probability of impact ionisation

multiple cross-talk.

**Delayed pixel-to-pixel cross-talk (DeXT):** Pixel-to-pixel cross-talk is also observed with significantly larger delays compared to DiXT. This phenomenon is explained by infrared photons absorbed deep in the bulk of the neighbouring pixels, releasing electrons that are amplified only after a significant drift time to the avalanche region. In this case, the secondary pulses have full amplitude (1 PE) but their time of arrival is distributed up to 100 ns, as shown in the right plot of Fig.(5.10). The DiXT and DeXT generation processes are illustrated in Fig.(5.9).

**After-pulse (AP):** In the pixel where a primary avalanche occurs, charge carriers can be trapped and released with some delay. The pulse amplitude depends on the recovery state of the pixel and ranges between 0 and 1 PE as visible in the bottom plot of Fig.(5.10). The time of arrival of AP is distributed over a few 100 ns<sup>2</sup>. The after-pulses can be used to measure the recovery time via a fit of the AP amplitude as a function of its arrival time.

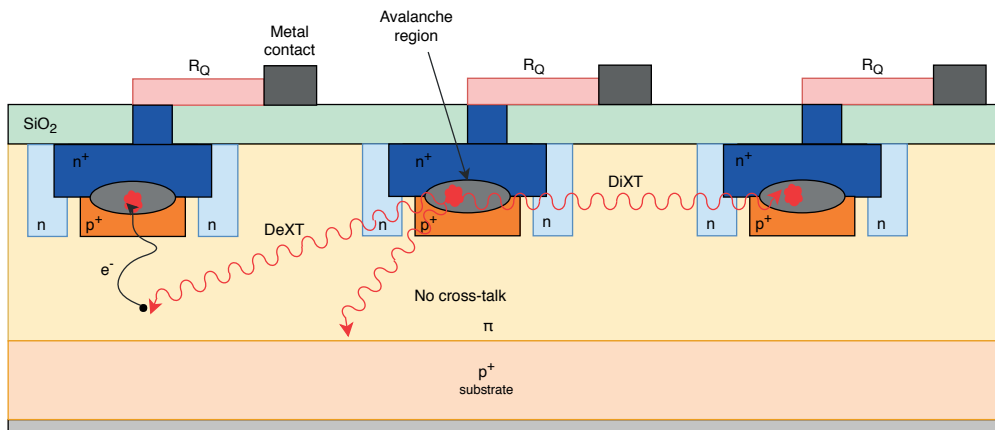


Figure 5.9: The processes of DiXT, DeXT are illustrated. The primary avalanche in the central pixel generates infrared photons that travels inside the SiPM. Some reach the avalanche region of a neighbouring pixel and trigger a simultaneous avalanche (DiXT). Others travel in the bulk of a neighbouring pixel where it can release an electron-hole pair. After a drift time the electron triggers an avalanche in the pixel (DeXT). Image inspired from [63].

To reduce DiXT, the active area of each pixel is isolated such that the photons produced in the avalanche region are contained within one pixel. The isolation is done using trenches filled with opaque material of several micrometers deep and with micrometer size width. The trenches are only partially efficient to avoid DeXT since the photon can be absorbed deep in the bulk and the consequent electron can drift to the neighbouring avalanche region.

<sup>2</sup> A much smaller contribution with longer time constant is also observed which can be neglected for the AP characterisation

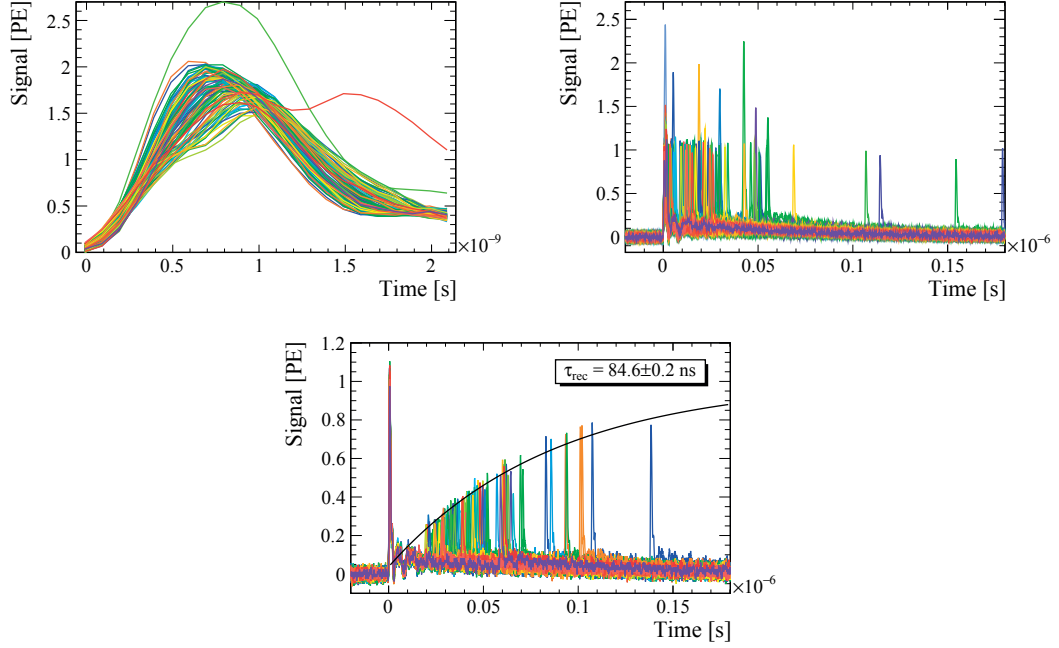


Figure 5.10: Example of SiPM correlated noise with DiXT (top left), DeXT (top right) and AP (bottom centre).

### Uncorrelated noise:

The arrival time of primary thermal noise pulses follows a random fluctuation. They produce avalanches that are indistinguishable from photon induced avalanches. The rate of the total random noise is called dark count rate (DCR). DCR depends on the temperature, the  $\Delta V$ , the total detector active area and on the quality of the silicon. The temperature change needed to reduce the DCR by a factor 2 is called  $K_{1/2}$ . This noise is produced in the high E field region and originate from two temperature dependent effects. For temperatures below 200 K tunneling noise is dominating while the Shockley-Read-Hall generation and recombination is dominating for higher temperature [61]. This dark current is produced by the bulk current (DCR) and the surface current is due to defects at the Si – SiO<sub>2</sub> interface. Both are  $\Delta V$  dependent [63]. Defect in the silicon lattice (as introduced in Sec.(4.4)) through radiation dramatically increases the DCR and so the dark current.

### 5.2.4 Photo detection efficiency

The photo detection efficiency (PDE) is defined as the number of detected photons over the number of incident photons. PDE is wavelength and  $\Delta V$  dependent and is the given by [60]:

$$\text{PDE}(\lambda, \Delta V) = \text{FF} \times \text{QE}(\lambda) \times P_{\text{Avalanche}}(\lambda, \Delta V) \quad (5.2)$$

with the following definitions:

**Fill factor (FF)** is the ratio between the active area of the detector and its total area. Pixels have dead areas necessary for routing lines, optical trenches and quenching resistors. The ratio  $FF = \text{active} / \text{dead area}$  is higher for larger pixel size.

**Quantum efficiency (QE)** is the probability that an electron-hole pair is created by a photon entering the depletion region. The QE depends on the incident photon wavelength.

**Avalanche probability ( $P_{\text{Avalanche}}$ )** is the probability for a single photoelectron to trigger an avalanche. The avalanche probability depends on  $\Delta V$  and reaches a plateau. The PDE inherits this behaviour.

The PDE is also affected by absorptions and reflections at the entrance window. Non reflective materials are used to improve the efficiency of the light transmission.

### 5.3 SiPM for the LHCb SciFi: requirements and development

A custom designed multichannel-array SiPM was developed for the LHCb SciFi tracker. The SiPM array is composed of 128 individual channels. These devices offer a good reliability due to a simple mechanical structure and provide high PDE in a large wavelength range. They are well suited to low light application with their high gain. The next two sections focus on their requirements and the development process.

#### 5.3.1 LHCb SiPM requirements

The optimisation of the photodetector to fulfil the requirements for the SciFi tracker application has many aspects and requires compromises.

**Maximisation of hit efficiency:** The most challenging requirement of the SciFi tracker is to reach 98% hit detection efficiency and low noise while keeping a low material budget. To achieve the requirements for the hit detection efficiency, the signal to noise ratio has to be optimised. For the signal it requires high PDE at the emission spectrum of the fibre (Fig.(3.8)). For the noise, the radiation hardness of the detector is required. The Fig.(5.12) illustrates a typical amplitude spectrum of a SciFi response with a cut to sufficiently reject noise while preserving over 98% efficiency to the signal. Note that distribution evolves with irradiation as presented later.

**Pixel size and recovery time:** The pixel size is a crucial parameter as it impacts various SiPM characteristics like PDE (via the FF), pulse shape, recovery time, cross-talk, AP and limits the number of pixels. The pixel size was chosen such that  $4 \times 26$  pixels cover the active area of

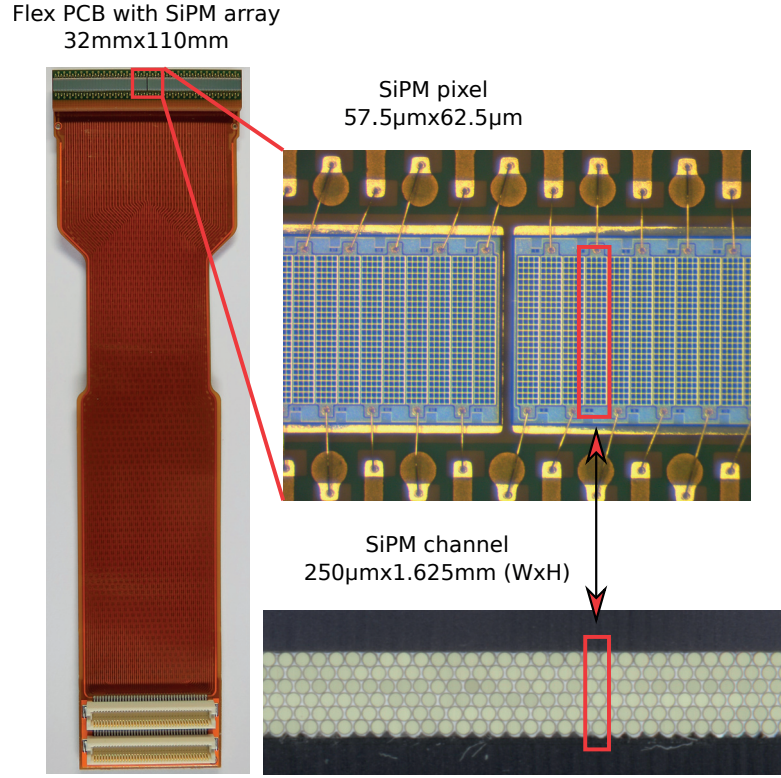


Figure 5.11: SiPM array mounted on a flex PCB on the left, zoom into the single channel size and the fibre mat on the right.

one channel of  $250\ \mu\text{m}$  wide and  $1.625\ \text{mm}$ . This leads to 104 pixels of  $57.5 \times 62.5\ \mu\text{m}^2$ . This large pixel allows for a high PDE ( $\approx 45\%$ ) and allows the implementation of optical isolating trenches to suppress cross-talk. The small number of pixels per channel has a negligible impact because inefficient events provide very little photons. Higher recovery time leads to a higher dead time of the pixel. Assuming 3 clusters per 128 channels (highest occupancy regions) with 16 PE per cluster at 30 MHz the signal per channel is  $f_{\text{sig}} = 12\ \text{MHz}$ . The DCR per channel is about 10 MHz. For pixels with a recovery time of 70 ns the average number of dead pixel is:

$$N_{\text{pix\_av\_dead}} = \frac{f_{\text{sig}} + \text{DCR}}{(1/\tau_{\text{rec}})} = 1.5 \quad (5.3)$$

resulting an inefficiency of:  $\epsilon_{\text{ineff}} = \frac{N_{\text{pix\_av\_dead}}}{N_{\text{pix\_total}}} = 1.6\%$

**Spatial resolution:** The requirements for the resolution is  $100\ \mu\text{m}$  for each detection plane. The binary resolution of a SciFi tracker with perfect alignment is  $250\ \mu\text{m}/\sqrt{12} = 72\ \mu\text{m}$ . For cluster of size two (typical events) and three the resolution is improved. The linearity and the

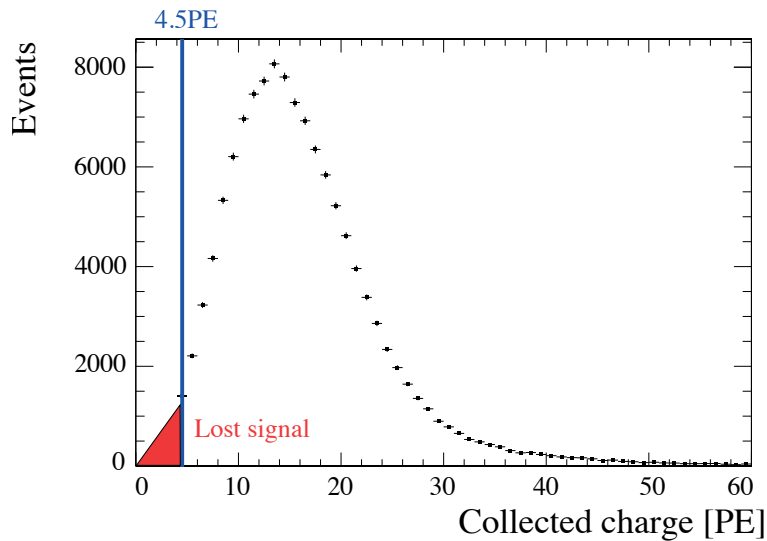


Figure 5.12: Example of amplitude distribution. The vertical line indicates the noise cut applied. The shaded area contains signals leading to inefficiency (signal cut).

dynamic range are found not to be critical.

**Minimisation of dead zones:** Due to manufacturing constraints, dead zones are introduced between the active region. Two silicon dies of 64 channels are packaged into one SiPM array of 128 channels of  $32.54 \pm 0.05$  mm width to minimise the dead areas. SiPM dead regions can be seen in Fig.(5.13).

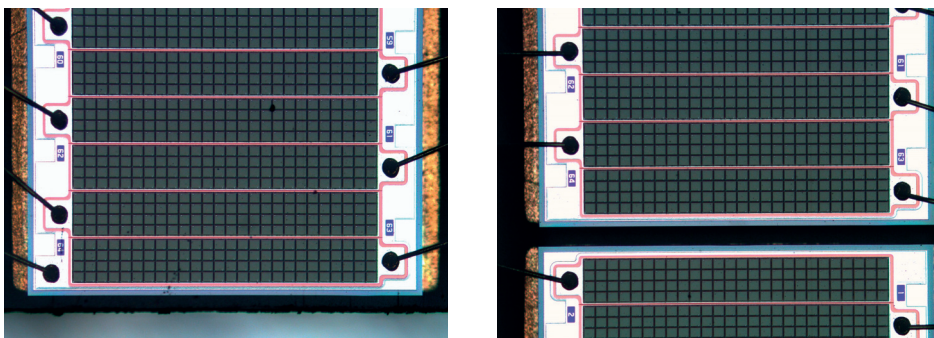


Figure 5.13: Dead zone at the edge of the SiPM array (left) and in between two dies (right)

### 5.3.2 SiPM technology evolution since 2011

Two companies have manufactured customised multichannel arrays for the LHCb SciFi, Hamamatsu (Japan) and KETEK (Germany). The customisation of the Hamamatsu multichannel array started in the context of a tracker development for a balloon experiment called PEBS([64, 65]) in 2011. In 2013 KETEK entered the R&D for this project. The major steps of the



### 5.3. SiPM for the LHCb SciFi: requirements and development

---

SiPM development by these two companies are described in the following.

#### **Hamamatsu technology customisation and prototypes:**

**H2011** First 128 channel array from Hamamatsu. This detector had no trenches and allowed only a small operation range. The operation point was typically  $\Delta V = 1.3\text{V}$ , had a very high cross-talk and low PDE (30%). The channel size was  $250\ \mu\text{m}$  wide and  $1.32\ \text{mm}$  height with 84 pixels.

**H2014** 128 channel array with trenches (the corresponding technology was named LCT3) and a channel size of  $250\ \mu\text{m}$  wide,  $1.5\ \text{mm}$  high and 96 pixels. The overvoltage was typically  $\Delta V = 3.5\text{V}$ , had much lower correlated noise and higher PDE (39%). PDE also increased thanks to the quench resistors implemented in a thin film technology.

**H2015** Second generation of multi-channel array with trenches (LCT5 technology) with an increased channel size of  $250\ \mu\text{m}$  wide and  $1.625\ \text{mm}$  height and 104 pixels. The cutting tolerances and assembly were improved to reduce the dead zones. The overvoltage was typically  $\Delta V = 3.5\text{V}$ . This type has a large after-pulse and delayed cross-talk.

**H2016** Third generation of multi-channel array including trenches (LCT3). Has the identical geometrical layout as H2015. It was expected to have improved correlated noise, slightly lower PDE, but showed in the end a similar correlated noise as H2015. The trench type was changed to an old version because of the increase of correlated noise in H2015 (this phenomenon was not understood).

**H2016\_HRQ** Third generation of multi-channel array including trenches (LCT5) but with increased quench resistor by a factor of three. The detector is stable over a large range of  $\Delta V$  and has low total correlated noise and excellent PDE (about 45%). The recovery time has increased by a factor three.

**H2017** Final version, identical technology as H2016\_HRQ.

**KETEK technology customisation and prototypes:** A development started in 2013 has led to the development of several multi-channel arrays prototypes. The latest generation received in April 2016 showed promising properties. Several problems caused by the packaging process and the change of foundry has introduced important delays and did not allow to make a fully functional chip for LHCb available in time. The major concerns are the reproducibility of the silicon process and the transition to an automated packaging process. The KETEK devices have some advantages over the Hamamatsu and at the same time promising features. The technology has shown very low correlated noise (2-3%) which is at least a factor two lower compared to Hamamatsu and the peak PDE is in the range of 43%. An advanced dicing process has also reduced the dead zones.

## Chapter 5. SiPM characteristics and motivation for LHCb

---

- K2014** Detectors with series of different implementations for trenches and pixel size. The channel size is  $250\ \mu\text{m}$  wide and  $1.625\ \text{mm}$  high. The overvoltage is typically  $\Delta V = 3.5\text{V}$ . Difficulty with packaging (humidity protection) caused a large number of dead channels. It shows a higher DCR after irradiation than Hamamatsu at cold temperature operation.
- K2015** Detectors with  $60 \times 63\ \mu\text{m}^2$  pixel surface. The active surface per channel is  $252\ \mu\text{m}$  wide and  $1.625\ \text{mm}$ . It has trenches, thin glass coating ( $5\ \mu\text{m}$ ) and very low correlated noise. First packaged chips arrived in April 2016 due to delays caused by the foundry and were not ready for mass production in time.

# 6 SiPM characterisation methods and results

## 6.1 SiPM characterisation methods

This chapter presents the four complementary setups used for the complete characterisation of an SiPM as a function of  $\Delta V$ , temperature and irradiation dose.

The first setup is used to collect data on an oscilloscope for a pulse shape statistical analysis. A similar setup featuring a monochromatic light source is used for PDE measurement. In both cases the data consists of recorded pulses and a pulse frequency measurement for the PDE determination at different bias voltage points. A third setup allows IV characteristics measurements in order to obtain  $R_Q$ , DCR and  $V_{BD}$ . Finally, a setup uses a short SciFi module and beta particles to obtain the light yield. This setup is also used for noise measurements.

The results obtained by applying these methods for two different SiPM technology are shown.

### 6.1.1 Pulse shape time dependent measurement

The analysis of pulses recorded on an oscilloscopes allows to measure the correlated noise probabilities DiXT, DeXT and AP as a function of  $\Delta V$ , as well as a statistical determination of the most important time constants, namely the long decay time ( $\tau_{long}$ ), the recovery time ( $\tau_{rec}$ ), the DeXT and AP mean lifetime. The principle is to acquire a large number of "dark" pulses (i.e. pulses obtained when the photodetector is in the dark), which are analysed off-line. As a first step, to have a precise value of  $\Delta V$ , the  $V_{BD}$  value needs to be measured simultaneously.

The pulse shape measurements are performed inside a dark enclosure, electromagnetic interference (EMI) shielded, to ensure high signal-to-noise ratio. The detector is read out with a high bandwidth voltage, 20 dBV, preamplifier and an oscilloscope. The detector is mounted on a PCB avoiding wire pins or cables to minimise serial inductance and the associated ringing. An illustration of the setup can be seen in Fig.(6.1), more details can be found in App.(A.1)

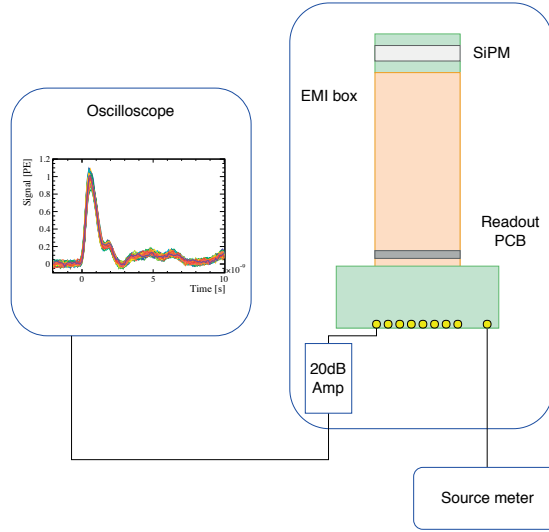


Figure 6.1: Illustration of the pulse shape measurement setup.

**Measurement of the  $V_{BD}$ :** The procedure to calculate  $V_{BD}$  is illustrated in Fig.(6.2). For each bias values, the 1 PE pulse amplitude ( $A_{1PE}$ ) is estimated by a Gaussian fit of the recorded amplitude distribution. The obtained values are then fitted with a linear function and, given that  $G \propto \Delta V$ ,  $V_{BD}$  is calculated as the bias voltage corresponding to zero amplitude. The value of  $V_{BD}$  depends on the temperature, but since the duration of the measurement is sufficiently short to avoid significant temperature changes, the  $V_{BD}$  obtained in this way can be used without further temperature corrections.

The  $V_{BD}$  obtained with this method is called  $V_{BD}^{Amp}$ , to differentiate it with the  $V_{BD}^I$  value obtained with the IV scan method presented in Sec.(6.1.3). The uncertainty on  $V_{BD}^{Amp}$  is typically between 10 and 50 mV with a reproducibility better than 5 mV.

An alternative method is to use the recorded waveforms for a numerical integration leading to the total charge. A linear fit of the charge measured at each bias voltage point is performed and its extrapolation to zero charge is called  $V_{BD}^{Int}$ .

The  $V_{BD}$  can also be extracted from a low light amplitude spectrum using a multichannel readout electronics (charge integrator and amplifier ASIC). For the characterisation of a large number of channels, this is the only viable option. This setup built in our lab can perform the data acquisition of 1024 channels simultaneously. The method is illustrated in Fig.(6.3), but a full description is given in App.(B.1). The  $V_{BD}$  value obtained with this method is called  $V_{BD}^G$ .

**Pulse shape analysis and pulse categorising algorithm:** The trigger amplitude and voltage scale of the oscilloscope are adjusted for each  $V_{bias}$  to avoid triggering on electronic noise or saturation. The time window selected for the measurement is  $[-20, 180]$  ns, where the

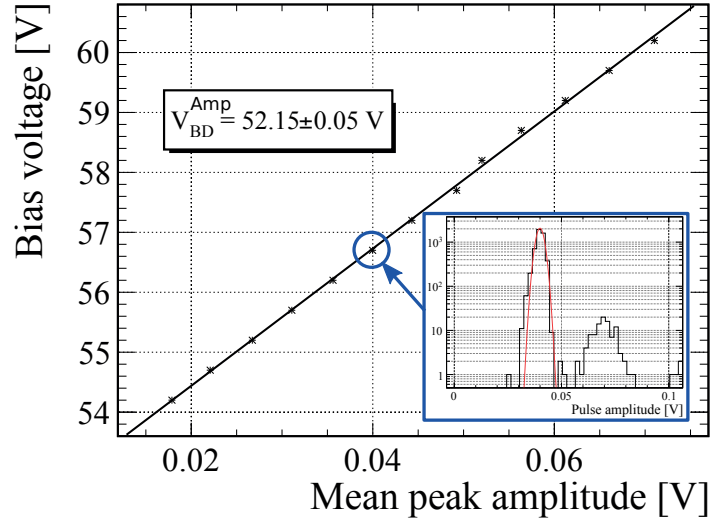


Figure 6.2: Illustration of  $V_{BD}^{Amp}$  determination procedure. The 1 PE amplitude is obtained from a fit of the primary pulse amplitude distribution. Note that mean amplitude value suffers from DiXT and cannot be taken. A linear fit of  $V_{bias}$  as a function of  $A_{1PE}$  is then performed, where  $V_{BD}^{Amp}$  is calculated.

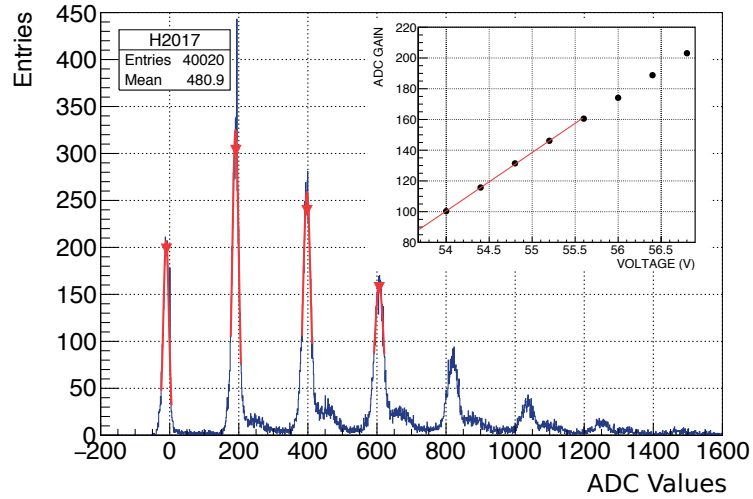


Figure 6.3:  $V_{BD}^G$  determination principle. The low light spectrum is obtained by injecting light pulses. The gain in the light spectrum is measured in units of ADC (digitised charge amplifier) and is obtained from the distance of two photon peaks.  $V_{BD}^G$  is obtained by extrapolating the gain for different bias point to zero. The fit of the gains was restricted to the first 5 lower points to improve robustness in the peak finding.

primary dark pulse is triggered at 0 ns. To distinguish DiXT, DeXT and AP, the sorting algorithm uses amplitude thresholds and time windows. The amplitude thresholds are set after the

## Chapter 6. SiPM characterisation methods and results

calibration in PE units for each  $V_{\text{bias}}$  points. The time window is set relative to the rising edge of the primary triggered pulse. Depending on the SiPM technology and size, the amplitude thresholds and time windows may be adjusted differently to account for the specific electronic noise level. Note that the serial inductance of the SiPM package induces ringing after the fast transient. Typical threshold values are 1.17 PE in a time window from 0 to 1 ns for DiXT, 0.85 PE for times above 1 ns for DeXT, and 0.25 PE for times above 10 ns for AP<sup>1</sup>. The time threshold for AP rejection helps to avoid wrong categorising of AP. Examples of pulses categorisations based on the different amplitude thresholds and time windows can be seen in Fig.(6.4). The limitations of the pulse sorting method are illustrated in Fig.(6.5).

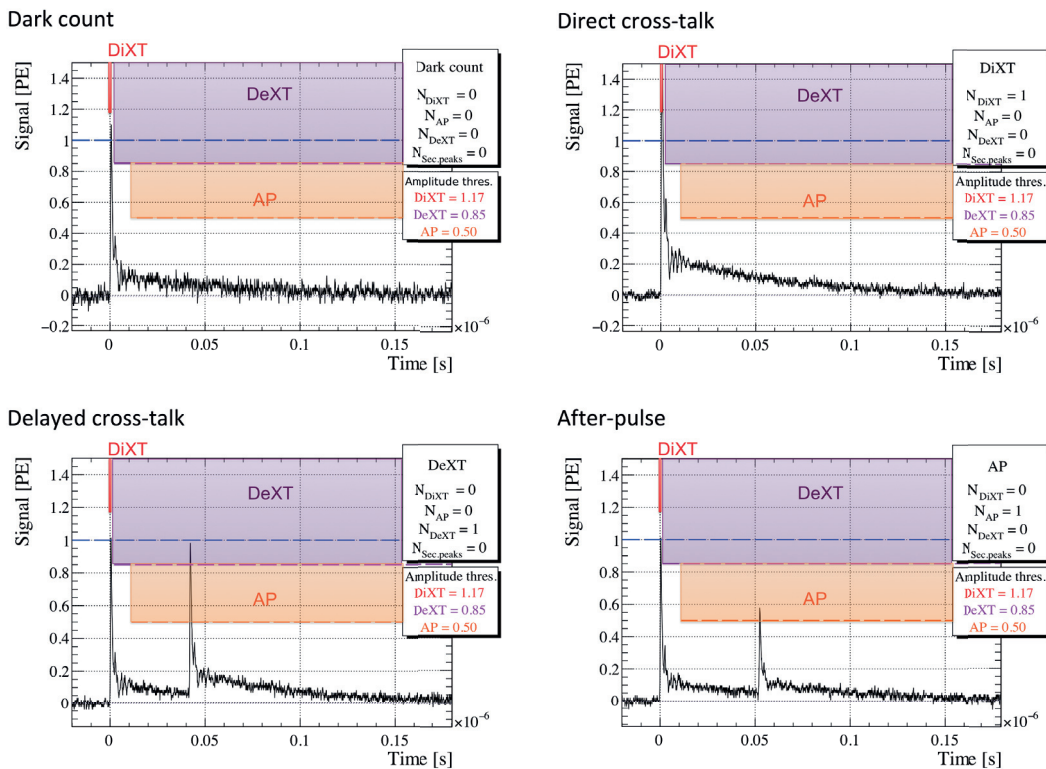


Figure 6.4: Example of peak categorisations with dark count (top left), DiXT (top right), DeXT (bottom left) and AP (bottom right).

The ratios of the classified pulses give the probabilities of the different sources of correlated noise. Each waveform may contain either only the primary noise pulse (called "clean events" or "dark count"), or a single or several correlated noise pulses. Every event containing correlated noise peaks is classified as DiXT, DeXT or AP, according to the nature of the first correlated noise pulse detected. If for a single recorded waveform more than one correlated noise peak is detected, the additional peaks are counted as "higher order" (noise of noise) correlated noise. The higher order noise is getting significant with increasing correlated noise rate. The

<sup>1</sup>To compare the AP probability with the manufacturer specification, the threshold is set to 0.5 PE

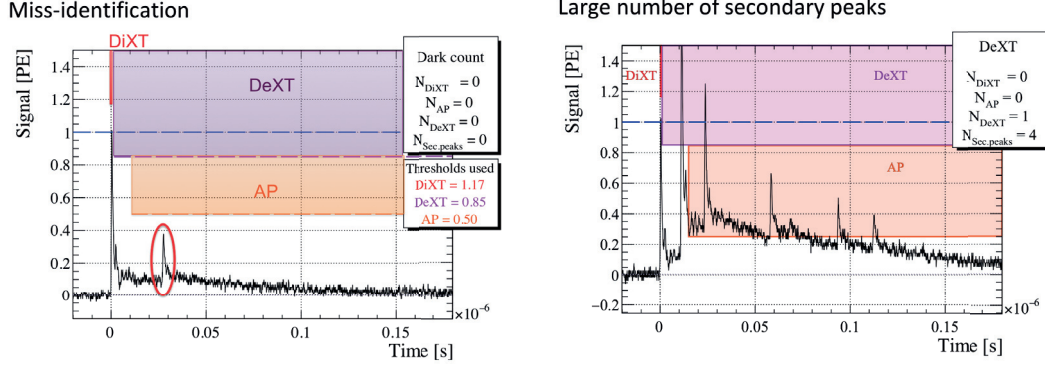


Figure 6.5: Limits of the peak sorting algorithm with AP miss-identification (left). The algorithm can also be used to categorise higher order noise peak (right).

probability of correlated noise of the kind X (DiXT, DeXT or AP) is the ratio of the number ( $N_X$ ) of waveforms classified as X to the total number ( $N_{ev}$ ):  $p_X = \frac{N_X}{N_{ev}}$ .

The procedure has nevertheless some limits. After a time of  $2 \cdot \tau_{rec}$ , the AP pulse amplitude reaches the DeXT amplitude threshold of 0.85 PE. At this point the pulses are indistinguishable and classified as DeXT. This effect is however small since the number of APs decreases exponentially with time. For detectors with high DCR, random dark pulses can occur in the sampling window and the algorithm accounts these pulses as DeXT. The level of contamination of DCR to the DeXT can be evaluated from the distribution of the arrival time. As an example for H2017 it is in the order of 1%.

For clean waveforms, a double exponential function fits the fast and slow components of the falling edge of the pulse, with time constants  $\tau_{short}$  and  $\tau_{long}$  respectively. For devices with small  $C_q$ , the slow and the fast components become indistinguishable. In our measurements, the observed fast component has a time constant of less than 1 ns and is dominated by the readout bandwidth of the oscilloscope.

$\tau_{rec}$  is measured from AP events as shown in Fig.(6.20). The amplitude is assumed to recover with time as  $1 - e^{-\frac{t-t_0}{\tau_{rec}}}$ , where  $t_0$  is the time needed for the recovery to start. A correction to the amplitude of the AP is introduced to compensate for the slow component of the primary pulse always present in the measurement. The fitted function is then:

$$A(t) = A_{1PE} \cdot \left(1 - e^{-\frac{t-t_0}{\tau_{rec}}}\right) + A_{slow} \cdot e^{-\frac{t}{\tau_{long}}}, \quad (6.1)$$

where  $A_{slow}$  is the amplitude of the slow component of the SiPM pulse. The two parameters  $A_{slow}$  and  $\tau_{long}$  are obtained by the pulse-shape fit while  $t_0$  is fixed to 4 ns<sup>2</sup>.

<sup>2</sup>The value for  $t_0$  has been fixed to the average observed value for robustness, it can be let free for verification

## Chapter 6. SiPM characterisation methods and results

The AP mean lifetime,  $\tau_{AP}$ , is obtained by an exponential fit of the number of AP pulses as a function of the arrival time as shown in Fig.(6.6). Using  $\tau_{AP}$  and  $\tau_{rec}$ , the fraction of APs missed due to the amplitude thresholds and time windows applied can be calculated. For a threshold of 0.5 PE, the fraction of missed APs is 93%. An exponential function is also used to describe the arrival time of DeXT pulses and allows to obtain  $\tau_{DeXT}$ , as shown in Fig.(6.6). The offset from the baseline is measured and attributed to random dark pulses present during the measurement. In this example approximately 180 pulses are interpreted as DCR for a total of 50k events, corresponding to a 6.5% contamination of the detected DeXT pulses. The probability of a random dark pulse falling in the measurement period is therefore 0.4%. Additional information can be found in App.(A.1).

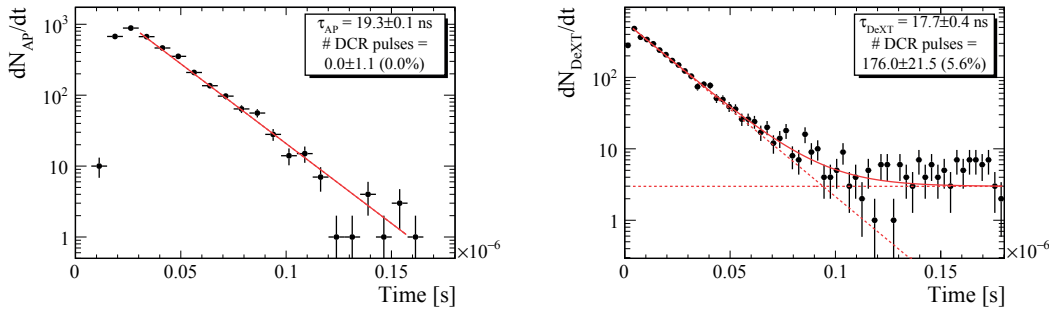


Figure 6.6: AP and DeXT mean lifetime determination and the DCR contribution estimate for the H2017 detector operated at  $\Delta V = 4.3$  V.

### 6.1.2 PDE and gain measurement

For devices with low DCR, the comparison of the PDE among different devices (relative PDE) can be made with a technique based on zero photon detection probability with low light illumination<sup>3</sup>. For more general case, the measurement of the absolute PDE is needed.

The measurement of the absolute PDE requires a precise determination of the gain and a correction for the correlated noise. The setup used to measure the absolute PDE is composed of a light source (Xe lamp) and a monochromator remotely controlled by a step motor. The monochromator allows a  $\pm 1$  nm wavelength region selection of the Xe lamp spectrum. The monochromator light is sent into an optical fibre to transport the light source to the detector. A light diffuser is used at a sufficiently long distance of the measurement point to homogenise the light beam. The calibration of the luminous power surface density ( $P_{lum}$ ) of the light beam is made by a calibrated photodiode. The setup is shown in Fig.(6.7).

The gain measurement methods and two independent absolute PDE measurements methods

purpose.

<sup>3</sup>This method is based on the Poisson probability  $P(0, \mu) = \exp^{-\mu}$  where  $\mu$  is the mean value of number of photons detected. Since only the component without photons needs to be measured, the gain and noise corrections are not required. Keeping the light intensity unchanged, the comparison of different devices is possible.



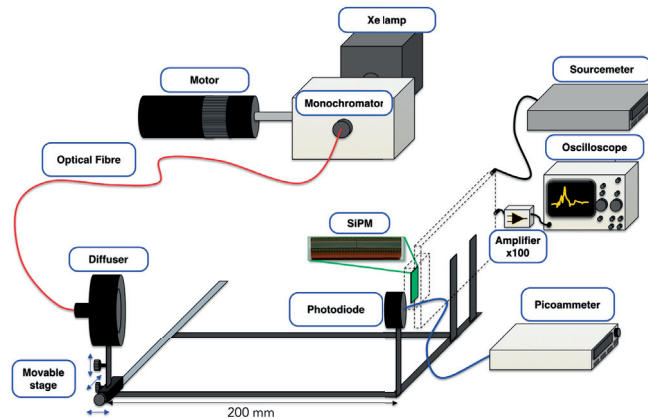


Figure 6.7: Illustration of the PDE setup.

(called "frequency" and "current" methods) are presented in this section while corrections, errors and a complete setup description can be found in the App.(A.2) and App.(A.3).

### Gain measurement

Measuring the gain of the SiPM with a voltage or charge amplifier requires a calibrated amplifier chain. The gain can be determined by a numerical integration of single dark or low light pulses. The measured integral  $\int U dt$  for a single pulse over time leads to the SiPM gain:  $G = 1 / (R_{\text{load}} \cdot G_{\text{Amp}} \cdot e) \cdot \int U dt$ , where the load resistance is typically  $50 \Omega$  (preamplifier input impedance). This method works better with low intensity light pulses where an external trigger is employed. The charge of single pulses is calculated and a linear fit is performed for different  $V_{\text{bias}}$ . The linear fit of the recorded values allows to extract  $G/\Delta V$  and evaluate the linearity of the measurement.

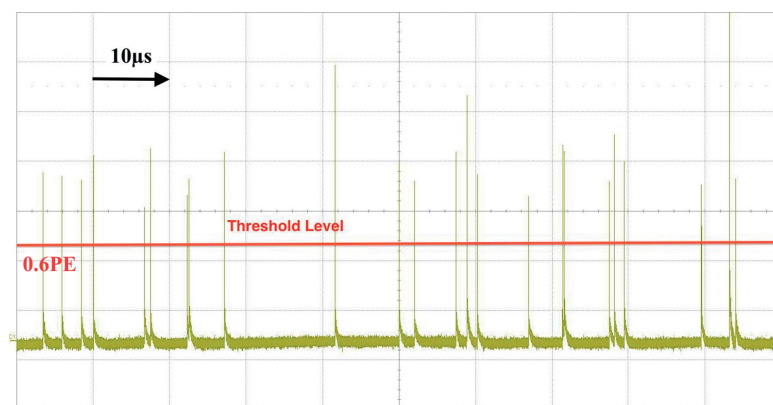


Figure 6.8: Illustration of the peak counting method.

The gain can also be calculated from the dark current  $I_{\text{dark}}$  and the DCR pulse frequency measurement, using  $I_{\text{dark}} = \text{DCR} \cdot G \cdot e$ . The method requires corrections for the correlated

noise. A statistical method of peak counting in a large interval of 100  $\mu$ s, with a given threshold is used and is illustrated in Fig.(6.8). The threshold is typically set to 0.6 PE knowing that AP pulses is partially below and partially above this threshold. A correction for the contribution of AP below threshold can be obtained by a numerical integration using AP mean lifetime and recovery time. The pulse frequency measurement is also corrected for DiXT. Note that the assumption of  $I \propto G$  is only valid over a restricted  $\Delta V$  range. Incomplete quenching (Fig.(5.5)) can be observed on devices with short recovery time or large pixel size. An additional current produces a deviation from the linear behaviour between the gain and the current. Fig.(6.9) shows the calculated gain as a function of  $\Delta V$  for one H2017 channel with this second method.

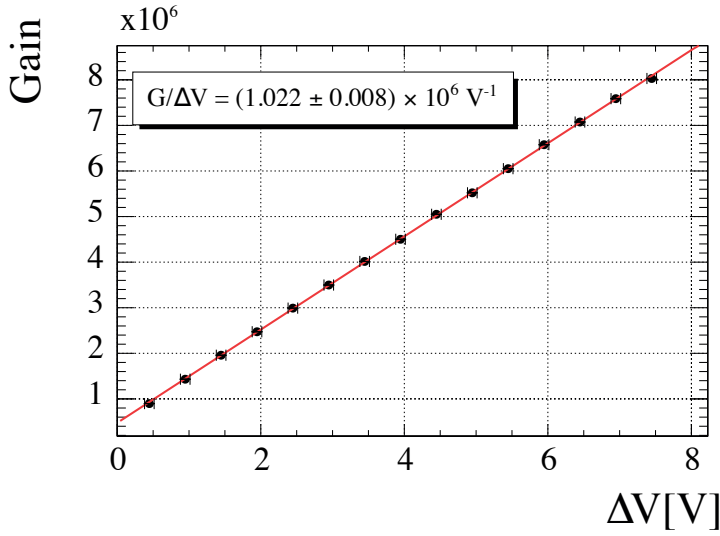


Figure 6.9: Gain as a function of  $\Delta V$  for one channel of H2017, the slope of the fit corresponds to  $G/\Delta V$  and shows in this case excellent linearity.

**PDE measurement:** The measured photo-current,  $I$ , in an SiPM in a light beam is, in first approximation, the product of the rate of detected photon ( $R$ ) with the SiPM gain and the elementary charge,  $I = R \cdot G \cdot e$ . In reality the total current  $I_{\text{total}}$  is the sum of the photo-current  $I_{\text{light}}^*$  and the dark current,  $I_{\text{dark}}^*$ . Both contributions can be corrected for any type of correlated noise by a correction factor. DiXT and DeXT contribute to the current with pulses of 1 PE and AP with a fraction of 1 PE. To correct for the amplitude of AP,  $w_{\text{AP}}$  is defined as the mean fraction of 1 PE pulse such that  $w_{\text{AP}} \cdot p_{\text{AP}}$  is equal to the total charge released from AP. More details on the correction can be found in App.(A.2). The PDE can be computed with the photo-current corrected for noise and is given by:

$$\text{PDE} = \text{QE}_{\text{PD}} \cdot \frac{I_{\text{light}}}{G \cdot I_{\text{PD}}} \cdot \frac{A_{\text{PD}}}{A_{\text{SiPM}}} \quad (6.2)$$

<sup>4</sup>The asterisk indicates in the following quantities that also contain correlated noise.

where  $I_{\text{light}}$  is the current measured on the SiPM with injected light ( $I_{\text{total}}$ ) corrected for dark current, correlated noise and higher order noise.  $G$  is the gain of the SiPM and  $A_{\text{PD}}$  and  $A_{\text{SiPM}}$  the active area of the photodiode and SiPM respectively.

The uncertainty in the gain measurement is due to the measurement uncertainty on the current and correction factors. To partially overcome this issue, the PDE can also be measured using a pulse counting method. This method depends on keeping the pulse frequency low to avoid random overlap. A homogeneous low intensity light beam is used and the frequency of pulses is recorded at a threshold of 0.6 PE. The PDE of the SiPM can be calculated by:

$$\text{PDE} = \text{QE}_{\text{PD}} \cdot \frac{f_{\text{light}}}{I_{\text{PD}}/e} \cdot \frac{A_{\text{PD}}}{A_{\text{SiPM}}} \quad (6.3)$$

where  $f_{\text{light}}$  is the frequency measured on the SiPM with injected light corrected for DCR, correlated noise and higher order noise. The current of the photodiode is used and its gain is  $G = 1$ .  $I_{\text{PD}}$  is the current measured on the photodiode.

### 6.1.3 IV measurement

The IV curve in reverse direction provides access to DCR as a function of  $\Delta V$  by calculating the ratio of dark current and gain [66]. For devices with high DCR, the pulse counting method fails due to the overlap of pulses. In this case, the IV measurement still provides valid results. The IV measurement allows to characterise irradiated detectors with DCR above 1 GHz/mm<sup>2</sup>. Self heating due to the current for devices with high DCR can limit the voltage scan range. The IV measurement also allows an alternative determination method for  $V_{\text{BD}}$ . The measurement of  $V_{\text{BD}}$  is not affected by self heating as long as only a small region around  $V_{\text{BD}}$  is scanned. The IV curve taken in forward direction allows to measure the quench resistor value.

The setup consists of a computer controlling both a multiplexer and a source meter to perform IV on multichannel devices. The detector is placed in a light shielded box. A temperature controllable enclosure is added to the setup for DCR temperature dependency characterisation. It is illustrated in Fig.(6.10) and complementary informations can be found in App.(A.4).

**Quench resistor measurement:** The IV characteristics in the region [-1,0] V shows the typical shape of a forward biased silicon  $p - n$  junction. For higher forward voltages the current is limited by  $R_{\text{Q}}$  and shows an almost linear characteristic. A linear regression is performed in the region from -1 V to -3.5 V and the slope,  $\frac{dV}{dI}$ , leads to:  $R_{\text{Q}} = N_{\text{pixel}} \cdot \frac{dV}{dI}$ , where  $N_{\text{pixel}}$  is the total number of pixels. Note that the result depends somehow on the fit region due to the non perfectly linear characteristics of the  $p - n$  junctions connected in series.

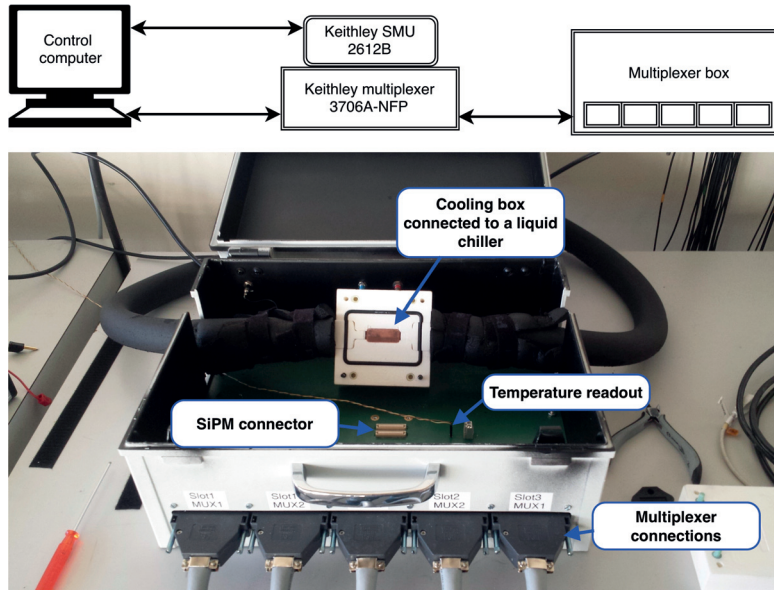


Figure 6.10: Illustration of the IV scan setup.

**Breakdown voltage measurement:** From the reverse bias region where a steep current increase is seen, the  $V_{BD}$  value can be extracted. Reference [66] presents the method in details. The assumption of an exponential current increase leads to  $I(V_{bias}) = \alpha \cdot (V_{bias} - V_{BD})^\epsilon$  where  $I$  is the measured current, and  $\alpha$  and  $\epsilon$  are constants determining the shape of the IV curve. A linear fit of "the logarithmic derivative":

$$\left[ \frac{d \ln(I)}{d V_{bias}} \right]^{-1} = \frac{(V_{bias} - V_{BD}^I)}{\epsilon} \quad (6.4)$$

is used to extrapolate the linear region to zero  $V_{bias}$ . The subscript "I" distinguishes the quantity  $V_{BD}^I$  from  $V_{BD}^{Amp}$  obtained from the gain measurement methods of Sec.(6.1.1). The fit region is typically in the range of  $(V_{BD} + 0.5 \text{ V to } V_{BD} + 1.5 \text{ V})$  as shown in Fig.(6.11). The reproducibility of the  $V_{BD}$  measurement is better than 10 mV. To improve the signal-to-noise ratio for  $V_{BD}$  measurement, a constant illumination can be added without affecting the result for  $V_{BD}$ .

The plot in Fig.(6.11) illustrates the procedure for four channels from a 128-channel array device. The minimal current observed in the IV measurement in the region below  $V_{BD}^I$  depends on the voltage increase rate. The detector and the detector package represent a capacitance which is charged as the voltage is increased inducing a current proportional to  $dV/dt$ .

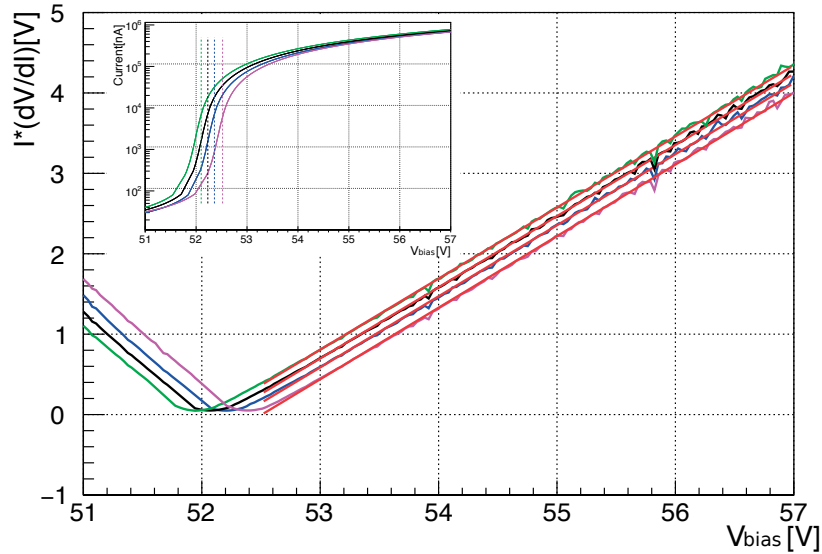


Figure 6.11: The logarithmic derivative and the linear fit with light injected is shown for 4 channels. The corresponding reverse IV curve are shown on the top.

**DCR measurement:** With the gain obtained in Sec.(6.1.2), the DCR can be computed with:

$$\text{DCR} = \frac{I}{G \cdot e} \quad (6.5)$$

where  $I$  is the current obtained from the IV measurement in the dark.

#### 6.1.4 Measurement with short SciFi module and electron-gun

A  $\beta$ -source in a small electron spectrometer (electron-gun) is used to inject electrons into a fibre module of 34 cm. The electron-gun is mounted on the x-y table to inject the beam over the full detection region. Injecting particles in this way is very close to a MIP. Nevertheless, cluster size and light yield are different since the energy deposited differs. This measurement is used in particular for light yield and noise cluster rate comparisons of irradiated and non-irradiated sensors, as explained in the following. A pictures of the setup can be seen in Fig.(6.12) and additional informations are given in App.(A.5).

**Light yield:** The signal is clustered using the 10-bit clustering algorithm described in Sec.(3.6.2). The cluster total signal (called "cluster sum") is expected to follow a Landau distribution [41]. The light yield is defined as the most probable value (MPV) of the cluster sum distribution for a MIP particle as shown in Fig.(6.13). The difference between electrons and MIP for the light yield is estimated to be less than 10%.

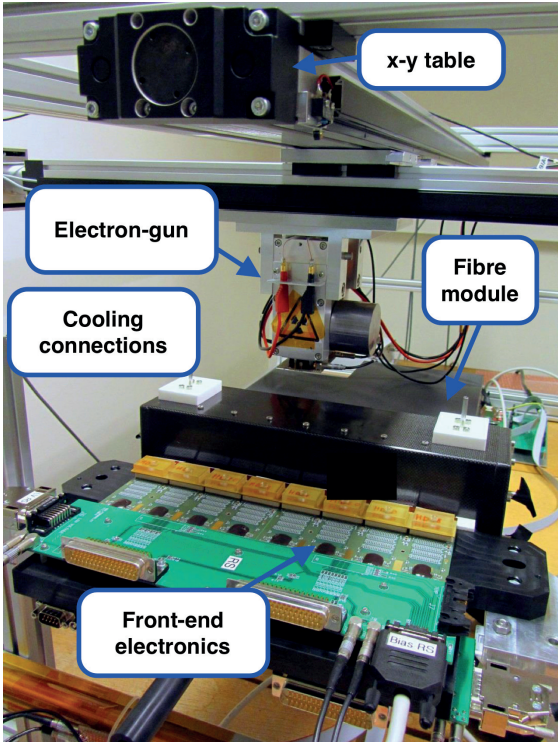


Figure 6.12: Picture of the short fibre module setup.

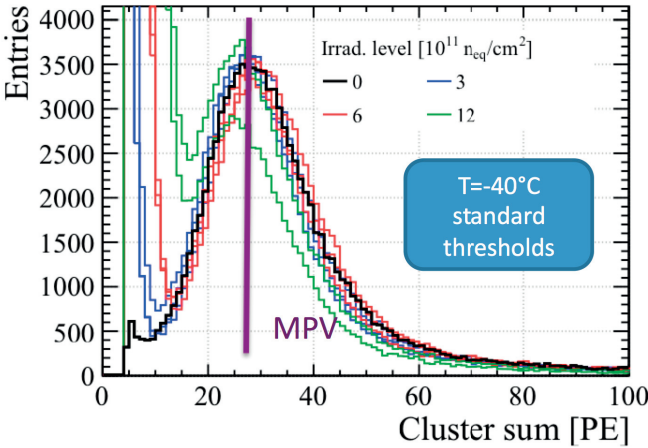


Figure 6.13: Illustration of the light yield determination procedure using the MPV of the distribution.

High DCR can influence the light yield because it is added to the light signal. The probability

of  $N_{DCR}$  noise pulses in the shaping window follows a Poisson distribution:

$$P(N_{DCR}) = \frac{e^{-\lambda} \cdot \lambda^{N_{DCR}}}{N_{DCR}!} \quad (6.6)$$

where  $\lambda$  is the ratio of the peaking time and the mean time between two noise pulses  
 $\lambda = \tau_{peakingtime} / \tau_{DCR} = \tau_{peakingtime} \cdot DCR$ . A correction for the contribution of DCR to the amplitude of a cluster of size CS is given by:

$$\langle N_{DCR} \rangle = \lambda \cdot CS = \tau_{peakingtime} \cdot DCR \cdot CS \quad (6.7)$$

The response of the shaper circuit for pulses arriving within the shaping time shown in Fig.(6.14). The superposed model is rectangular of width  $\tau_{peakingtime}$ .

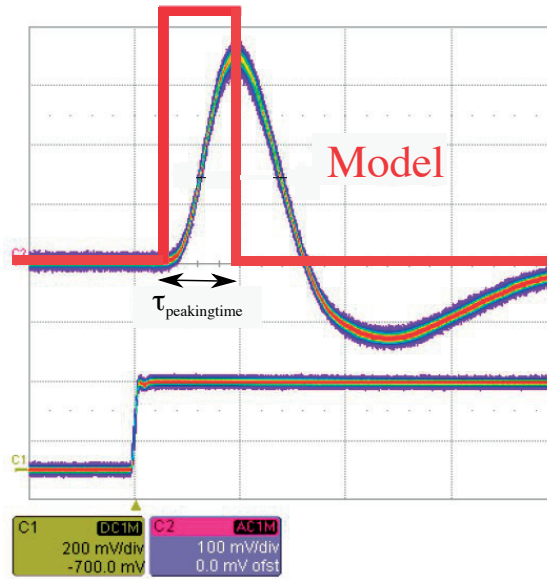


Figure 6.14: SPIROC pulse shape measured at the analogue output. The chip is set in the fast shaping mode. The  $\tau_{peakingtime}$  is about 100 ns. The shaped pulse assumed by the model is shown in red.

To be more accurate, the DCR measured in the dark spectrum can be used. Equation (6.7) is still valid with  $\lambda$  given by  $\lambda = \langle ADC \rangle / G_{ADC}$  with  $\langle ADC \rangle$  the mean amplitude measured in the dark and  $G_{ADC}$  the gain in ADC.

**Noise cluster rate (NCR):** The noise clusters are produced through two different mechanisms occurring for the SiPM readout:

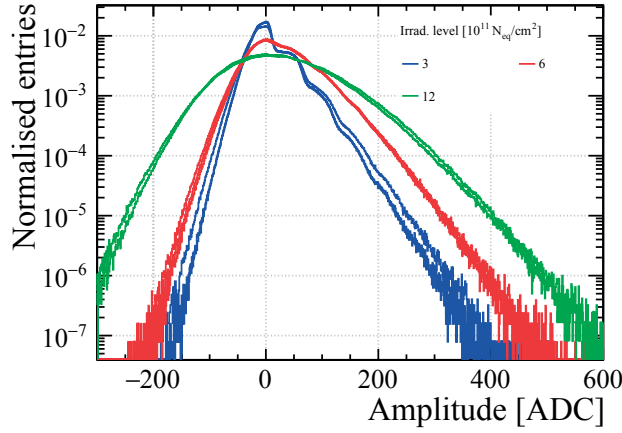


Figure 6.15: ADC (digitised charge amplifier) dark spectrum at  $\Delta V = 3.5$  V for detectors with high DCR.

- **Correlated noise in the SiPM:** DiXT, DeXT and AP adds up to a total dark signals reaching the thresholds.
- **Random overlap of dark pulses in the electronics:** for high DCR, a random overlap of dark pulses within the shaping time window can occur and results in a large signal. Its probability depends on the shaping time and on the DCR rate.

The NCR value strongly depends on the clustering thresholds. Applying the clustering algorithm to a dark spectrum of the SciFi, the noise cluster rate can be calculated for 128 channels devices readout at 40 MHz:

$$f_{\text{NCR}} = \frac{N_{\text{NC}}}{N_{\text{ev}}} \cdot 40 \text{ MHz} \quad (6.8)$$

with  $N_{\text{NC}}$  the number of noise clusters and  $N_{\text{ev}}$  the number of events recorded.

## 6.2 Results for the Hamamatsu H2017

**Breakdown voltage:** The breakdown voltage measurement for H2017 was performed using the methods introduced earlier.  $V_{\text{BD}}^{\text{I}}$ ,  $V_{\text{BD}}^{\text{G}}$ ,  $V_{\text{BD}}^{\text{Int}}$  and  $V_{\text{BD}}^{\text{Amp}}$  are compared in Fig.(6.16).

$V_{\text{BD}}$  typically changes by  $\pm 300$  mV within one array and follows a repeating patterns of 64 channels. These variations are due to manufacturing differences during the silicon processing. Small geometrical differences can produce electric field variations. Hamamatsu selects pairs of chips with almost identical  $V_{\text{BD}}$  profiles which originate from the same wafer region.



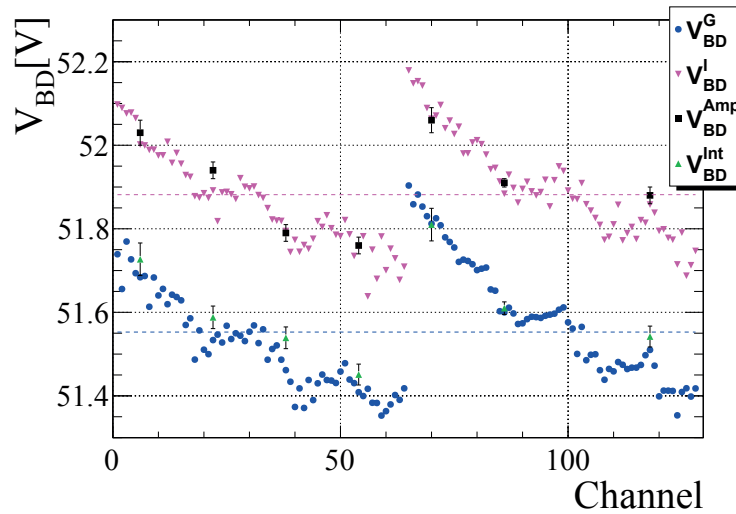


Figure 6.16: Comparison of the results for  $V_{BD}$  obtained by four different methods for a 128-channel array device.  $V_{BD}^G$  and  $V_{BD}^{Int}$  obtained by the charge integration methods yield compatible results.

A systematic difference of 300-400 mV is found between  $V_{BD}^{Amp}$  and  $V_{BD}^{Int}$  measurements based on charge integration was found. A possible explanation is a deviation from the linearity of  $A_{1PE}$ . The linearity of  $A_{1PE}$  as a function of  $V_{bias}$  is maintained up to high  $\Delta V$ . However, in the region from 0 to 0.3 V, a deviation is observed which explains the offset in  $V_{BD}$  measurement results. It has been found that when measurements are taken with bandwidth limitation, which suppresses the SiPM fast component,  $V_{BD}^{Amp}$  converges to the  $V_{BD}^{Int}$  and  $V_{BD}^G$  values.

The distribution of  $V_{BD}^G$  over 20 detectors from the production batch can be seen in Fig.(6.17).

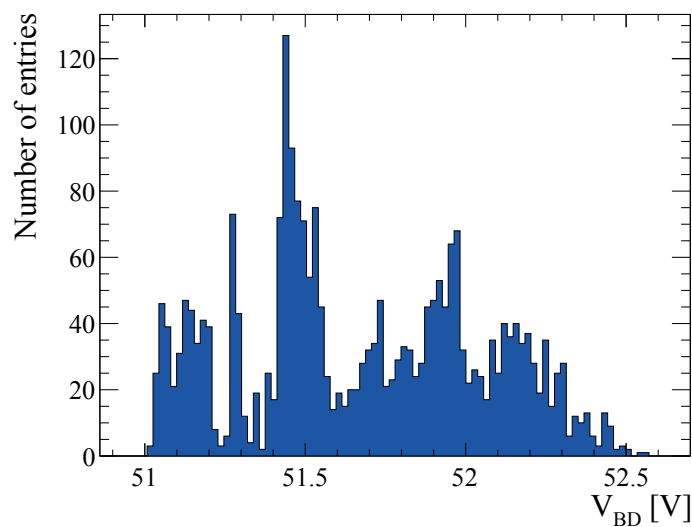


Figure 6.17:  $V_{BD}$  spread over the 128 channels of 20 detectors from the production batch.

## Chapter 6. SiPM characterisation methods and results

The  $V_{BD}^I$  measurement over a temperature range of  $70^\circ\text{C}$  is used to determine the temperature coefficient. For H2017, the temperature coefficient is found to be  $60 \pm 2 \text{ mV/K}$ . For such detectors operated at  $\Delta V = 3.5 \text{ V}$  a change in temperature of  $0.5^\circ\text{C}$  results in a gain changing by 0.8%.

**Quenching resistor:** The quenching resistor shows a relatively large spread between detectors (from 470 to 570  $\text{k}\Omega$ ) and within one detector between odd and even channels (typically 25  $\text{k}\Omega$ ). The  $R_Q$  value for the 128 channels of one SiPM can be seen in Fig.(6.18). Odd and even channels are readout from different sides of the die. Because of that,  $R_Q$  is implemented differently on the pixels for odd and even channels. This explains the structures seen in the  $R_Q$  profile from Fig.(6.18).

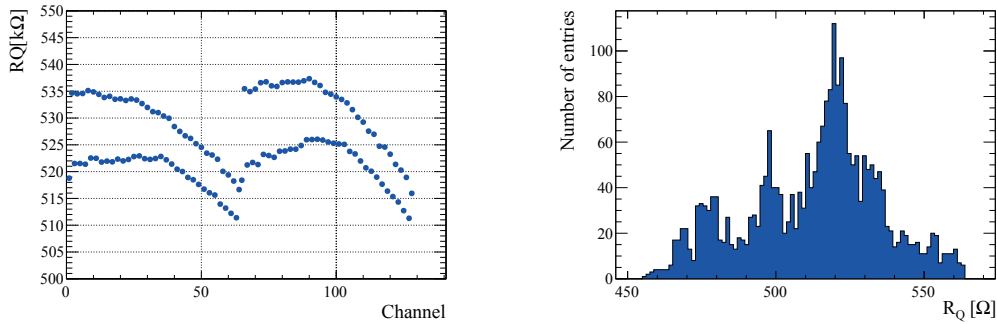


Figure 6.18:  $R_Q$  distribution within one SiPM (left) and of all 128 channels of 20 SiPMs (right).

The  $R_Q$  distribution of all 128 channels of 20 SiPMs can also be seen in Fig.(6.18). There is no simple correlation between  $V_{BD}$  and  $R_Q$  as shown in Fig.(6.19).

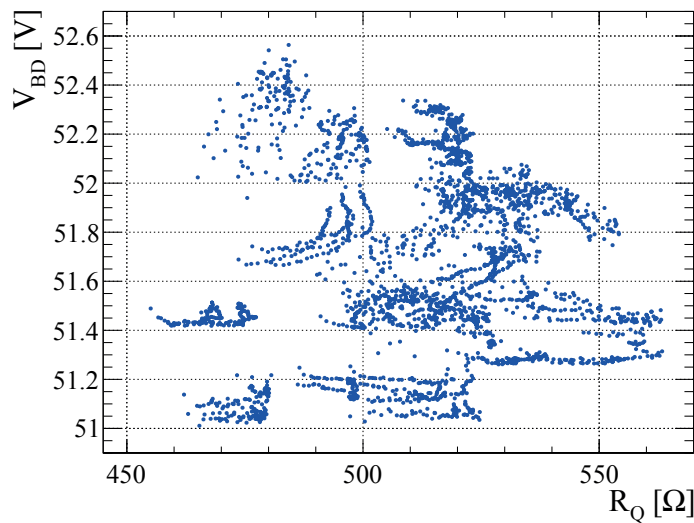


Figure 6.19: Scatter plot of  $V_{BD}$  as a function of  $R_Q$ . No simple correlation is seen.

**Time constants:** For the H2017 detector,  $\tau_{\text{rec}}$  is found to be 84.6 ns as illustrated in Fig.(6.20). In Fig.(6.21), several clean pulses have been averaged and the resulting waveform is fitted to find  $\tau_{\text{long}}$ . The average cancels the fluctuations of the baseline allowing to obtain a robust fit even for small amplitudes. The long time constants is found to be  $\tau_{\text{long}} = 68.0$  ns. The different time constants are found to be independent from  $\Delta V$  as shown in Fig.(6.22).

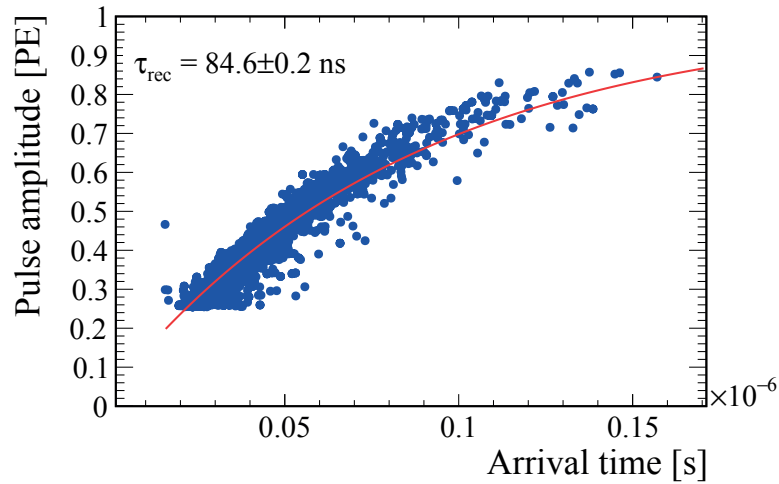


Figure 6.20: Recovery time measurement from the amplitude as a function of the arrival time for AP pulses.

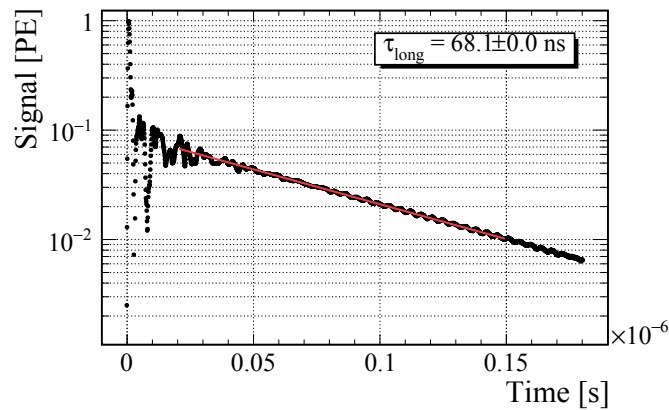


Figure 6.21: Long decay time constant extracted from a fit of clean events.

The previous results for the time parameters of the signal waveform allow to calculate the electrical model parameters. Taking  $R_Q = 503 \text{ k}\Omega$  the values for the capacitors of the model are calculated from the relation for  $\tau_{\text{long}}$  and  $\tau_{\text{rec}}$  of Sec.(5.1.1):  $C_d = 136 \text{ fF}$  and  $C_q = 34 \text{ fF}$ . With the two capacitor values, the gain can be calculated as  $G/\Delta V = (C_d + C_q)/e = 1.05 \cdot 10^6 \text{ V}^{-1}$  which is close to the value of  $1.02 \cdot 10^6 \text{ V}^{-1}$  obtained from pulse frequency and current measurement.

Fig.(6.6) shows the determination of the mean lifetimes for DeXT ( $\tau_{\text{DeXT}} = 17.7 \pm 0.4 \text{ ns}$ ) and AP

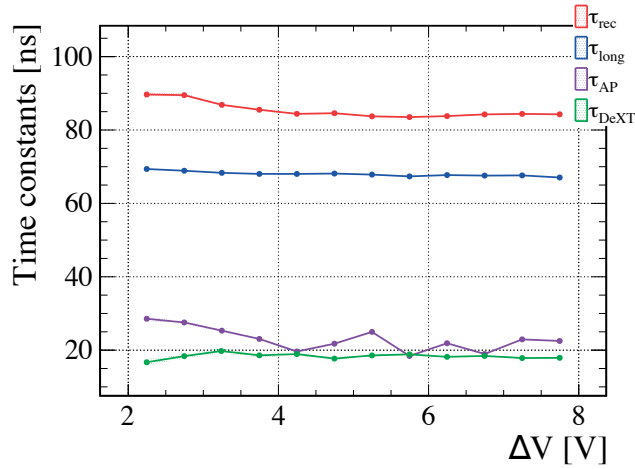


Figure 6.22: Fit results of the time constants for different  $\Delta V$ . The time constants do not depend of  $\Delta V$ .

( $\tau_{AP} = 19.3 \pm 0.1$  ns) as well as the DCR contribution (5.6%).

**Correlated noise:** As shown in the left plot of Fig.(6.23), the correlated noise of the H2017 detector has contributions from DiXT and DeXT. Higher order noise represents an important contribution if the primary correlated noise exceeds 20%, as shown in the example of the right plot of Fig.(6.23). The thresholds used are ( $th_{AP} = 0.5$  PE,  $th_{DeXT} = 0.85$  PE and  $th_{DiXT} = 1.2$  PE).

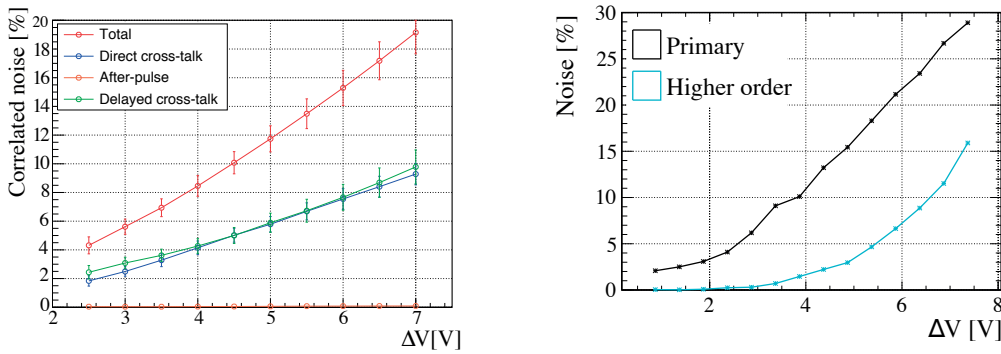


Figure 6.23: Correlated noise probabilities for a H2017 detector as a function of  $\Delta V$  with only primary correlated noise composition (left) and including secondary noise (right).

For illustration, Fig.(6.24) shows the amplitude versus time distribution of correlated pulses ("random overlap"). DiXT pulses are single pulse or multiple simultaneous DiXT pulses, with amplitude reaching up to 4 PE. The DiXT from DeXTs and APs with amplitude between 1-2 PE can be observed. The secondary pulses cover a relatively large region of amplitudes and time.

As shown in Fig.(6.25), large baseline fluctuations can occur from the superposition of many

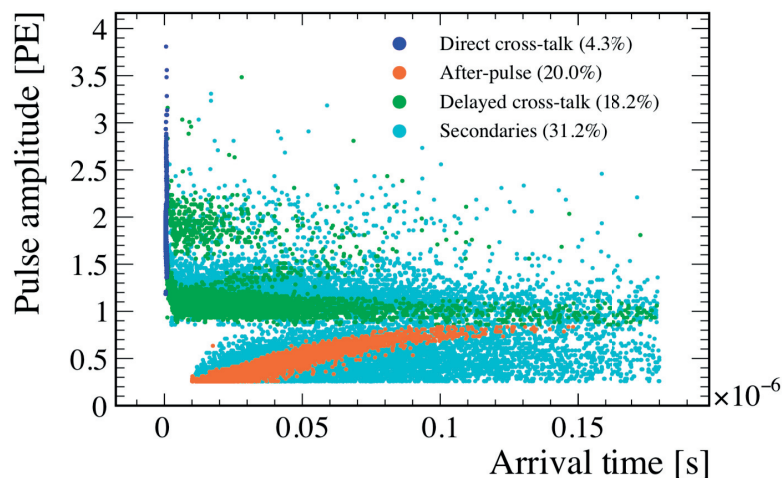


Figure 6.24: Amplitude of correlated pulses as a function of arrival time (H2017 at  $\Delta V = 8.0V$ ).

correlated pulses. Therefore the time windows and the thresholds must be adjusted carefully in order not to overestimate the secondary correlated noise probability.

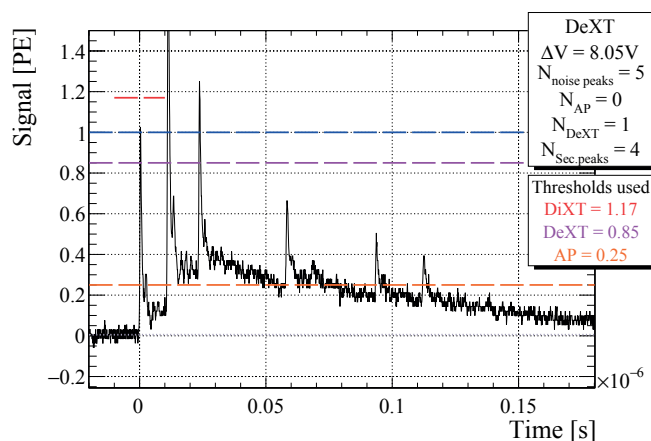


Figure 6.25: Pulse waveform classified as delayed cross-talk with additional secondary pulses recorded at high  $\Delta V$  (H2017 at  $\Delta V = 8.0V$ ).

Using the thresholds ( $th_{AP} = 0.5 PE$ ,  $th_{DeXT} = 0.85 PE$  and  $th_{DiXT} = 1.2 PE$ ), 160 channels from 20 different SiPMs were tested. In the results shown in Fig.(6.26), both DiXT and DeXT are the dominant source at the level of 3-4% for  $\Delta V = 3.5 V$ .

AP is negligible with the above thresholds set. The total correlated noise is always less than 10% at  $\Delta V = 3.5 V$ .

**Gain and photo detection efficiency:** Using the method exposed in Sec.(6.1.2), the gain per  $\Delta V$  is found to be  $G/\Delta V = 1.02 \cdot 10^6 \pm 1 \cdot 10^4 e/V$ . This result is fully compatible with the value of

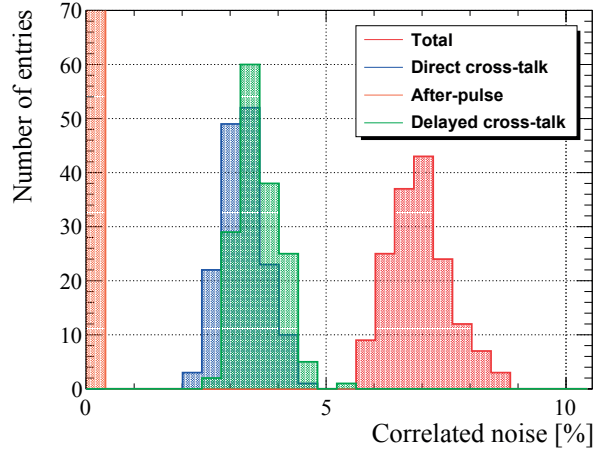


Figure 6.26: Correlated noise for 160 channels out from 20 different detectors with the standard thresholds ( $th_{AP} = 0.5$  PE,  $th_{DeXT} = 0.85$  PE and  $th_{DiXT} = 1.2$  PE) at  $\Delta V = 3.5$  V.

$1.05 \cdot 10^6$  e/V obtained previously estimated using  $\tau_{rec}$ .

The PDE as a function of wavelength and  $\Delta V$  obtained with the current and frequency methods are shown in Fig.(6.27) and (6.28) respectively. The results are compatible within uncertainties and differ by less than 2% from Hamamatsu values.

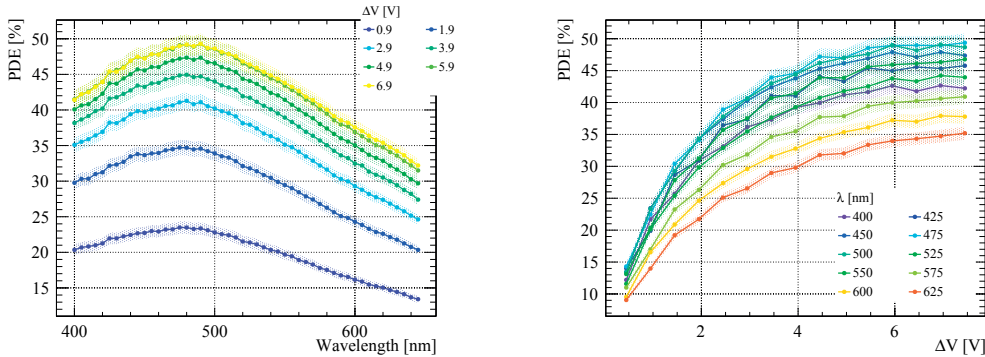


Figure 6.27: PDE measurement with current method. In the left plot different curves correspond to different  $\Delta V$ , in the right plot to different wavelengths.

### 6.2.1 Irradiation campaigns and results

As explained in the previous chapters, radiation creates defects in the silicon lattice which promotes the thermal excitation of charge carriers. The primary damage for the SiPMs in LHCb results from non ionising energy losses, with possible macroscopic effects such as higher depletion voltage, increase of DCR and decrease in PDE. The damage resulting from different particles and different energies is converted by means of the so called "hardness factor" (NIEL) to the effects caused by one neutron of 1 MeV  $n_{eq}$  per  $cm^2$  [67]. DCR seems to

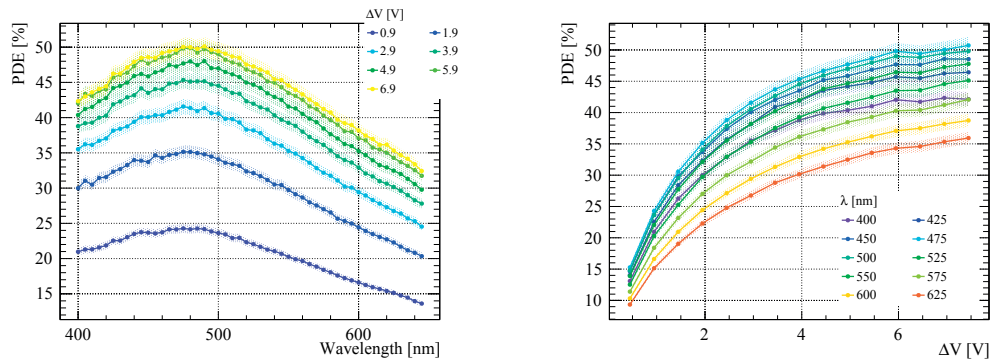


Figure 6.28: PDE measurement with frequency method. In the left plot different curves correspond to different  $\Delta V$ , in the right plot to different wavelengths.

be the only parameter affected by radiation up to the investigated neutron fluence for LHCb ( $12 \cdot 10^{11} \text{ n}_{\text{eq}}/\text{cm}^2$ ). Detectors were irradiated in two different irradiation facilities:

1. JSI at Ljubljana<sup>5</sup>, TRIGA MARK II reactor [68]. The spectral composition of the channel used is 37.9% thermal neutrons ( $<0.625 \text{ eV}$ ), 29.4% epithermal neutrons ( $0.625 \text{ eV} - 0.1 \text{ MeV}$ ) and 32.7% fast neutrons ( $>0.1 \text{ MeV}$ ). The total neutron flux is  $1.175 \cdot 10^{13} \text{ n}_{\text{eq}}/\text{cm}^2\text{s}$ . Samples of H2014, H2015, H2016\_HRQ and K2015 were irradiated to fluences of 3,6 and  $12 \cdot 10^{11} \text{ n}_{\text{eq}}/\text{cm}^2$ . An error on the dose of 10% is estimated.
2. Proton irradiation at Bern Swan Cyclotron facility. The beam energy is 18 MeV. The dose is converted according to the NIEL curve [69] with some uncertainties. This is an important verification of the radiation damage due to charged particles. H2016\_HRQ and H2017 were irradiated at this facility to doses of 50, 500 and 1 kGy (equivalent to  $9 \cdot 10^{11} \text{ n}_{\text{eq}}/\text{cm}^2$ ). The estimate dose uncertainty is 6% [70].

The DCR after irradiation can be reduced by an annealing cycle. Increasing the temperature to  $\sim 35^\circ\text{C}$  during several days reduces the DCR following a time distribution that can be fitted by a double exponential seen in Fig.(6.29). The DCR is typically reduced by a factor two compared to the value observed shortly after irradiation<sup>6</sup>. This process can be performed during the LHC shutdowns in order to increase the lifetime of the SiPMs.

Note that the results presented in the following are obtained after annealing to stabilise the DCR for the characterisation.

**Dark count rate** The expected linear relationship between leakage current and fluence [72] is confirmed by the measurements of DCR as shown in Figure 6.30. The correspondence

<sup>5</sup>This project has received funding from the European Union's Horizon 2020 Research and Innovation programme under Grant Agreement no. 654168.

<sup>6</sup>Note that the detector are irradiated and transported warm meaning the annealing is already taking place.

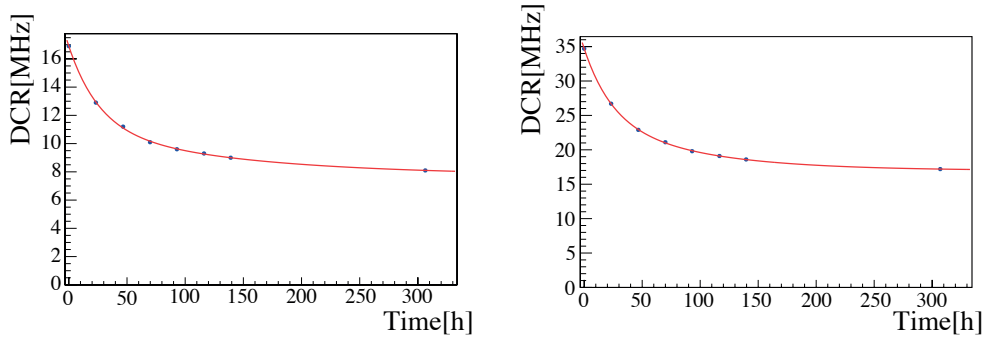


Figure 6.29: DCR as a function of time during the annealing process at 35°C for a H2015 detector irradiated to  $6 \cdot 10^{11} \text{ neq/cm}^2$  (left) and  $12 \cdot 10^{11} \text{ neq/cm}^2$  (right) and measured at -40°C. Image taken from [71].

between protons and neutrons [67] is expected but is less good at higher fluence. The observed difference is not explained.

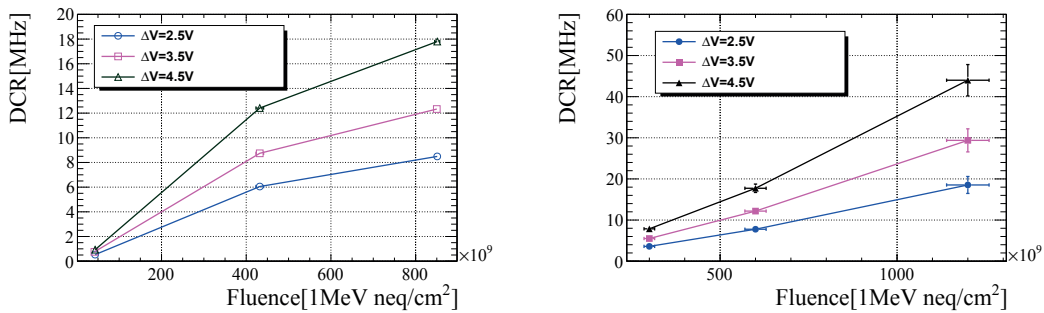


Figure 6.30: DCR for proton (left) and neutron (right) measured as a function of the fluence. Proton and neutron irradiation can be compared with a hardness factor of  $\sim 3$ . All measurements are performed at a temperature of -40°C.

The DCR temperature dependence coefficient  $K_{1/2}$  (defined in Chap.(5.2.3)) is measured in the temperature range of -50°C to -10°C. At higher temperature, pixel saturation strongly influence the DCR. Results can be seen in Fig.(6.31).  $K_{1/2}$  is found to be  $\sim 10^\circ\text{C}$  between -50°C to -10°C where no pixel saturation is present.

**Light yield and NCR results** The effect of radiation on the light yield was measured with the fibre module using the SPIROC front-end. Fig.(6.32) shows the comparison of the cluster sum for non-irradiated and irradiated SiPM kept at -45°C. A small decrease of the MPV at high irradiation dose is observed. The majority of the entries at low cluster sum are due to the noise. The ratio between the number of noise clusters compared to signal appears to be large. This can be explained by the fact that only one electron per event is injected while all channels can register random noise.

After correction for DCR using equation (6.7), the light yield is obtained by a Gaussian fit of the



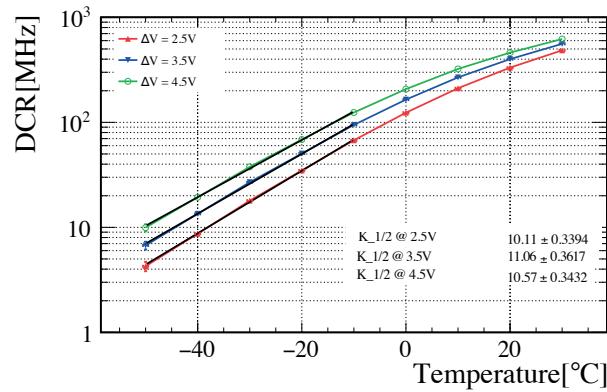


Figure 6.31: DCR measured as a function of the temperature.  $K_{1/2}$  is extracted from the fit in the range of  $-50^{\circ}\text{C}$  to  $-10^{\circ}\text{C}$ . Pixel saturation is present for DCR higher than 100MHz.

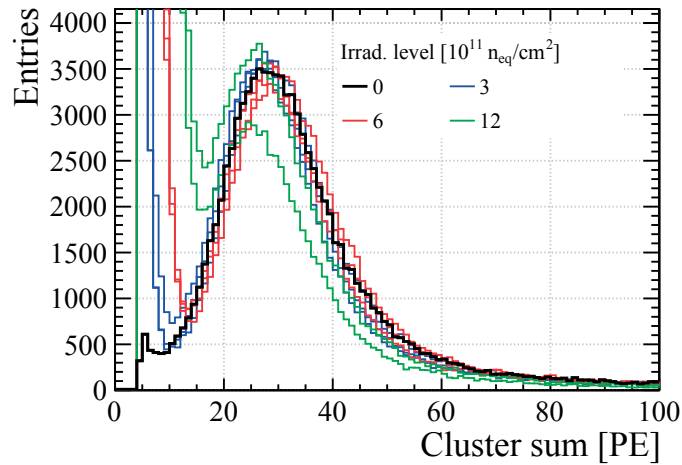


Figure 6.32: Cluster sum distribution for different irradiation level. Image taken from [73].

cluster sum distribution. For irradiation levels of  $3$  and  $6 \cdot 10^{11} \text{ n}_{\text{eq}}/\text{cm}^2$  the light yield decreases by less than 5% over the measured  $\Delta V$  range. For  $12 \cdot 10^{11} \text{ n}_{\text{eq}}/\text{cm}^2$  the observed decrease is 10%. However, this can also be caused by a gain decrease. For this radiation level the gain cannot be computed directly due to the absence of visible PE peaks.

Regarding NCR, its values strongly depends on the clustering thresholds and is shown as a function of the seed threshold in Fig.(6.33) for different irradiation levels. For H2017 using standard thresholds,  $\Delta V = 3.5 \text{ V}$  at  $-45^{\circ}\text{C}$ , the NCR obtained is 50 MHz.

In Fig.(6.34), the NCR as a function of the DCR for different  $\Delta V$  is shown. Each dashed line corresponds to one  $\Delta V$  value (constant total correlated noise) and each arrows indicates a constant irradiation level. In the region above 10 MHz all dashed lines converge indicating that the random overlap of dark counts is the dominant source. Below 10 MHz, the curves separate showing that the correlated noise becomes the dominant source of NCR since a

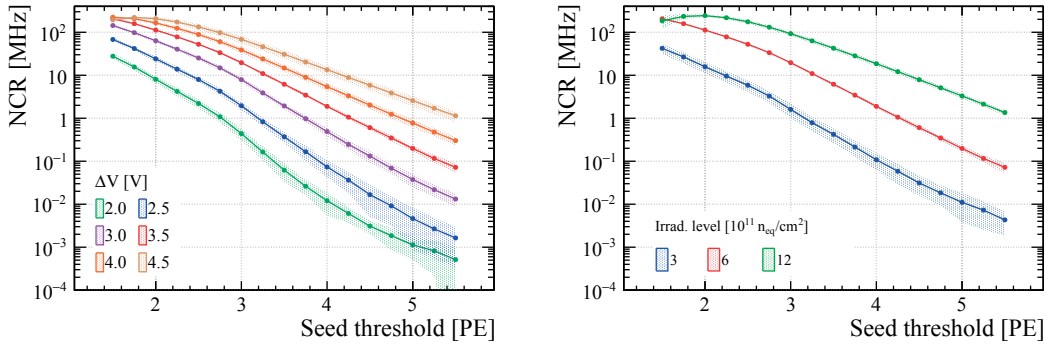


Figure 6.33: NCR for different  $\Delta V$  at  $6 \cdot 10^{11} \text{ n}_{\text{eq}}/\text{cm}^2$  (left) and irradiation levels at  $\Delta V = 3.5 \text{ V}$  (right) as a function of the seed threshold read out with the SPIROC ASIC at  $-45^\circ\text{C}$ . Image taken from [73].

small change in correlated noise results in a large NCR increase. This results demonstrates the strong interest to further improve the SiPM performances by reducing the total correlated noise and to use a fast shaping.

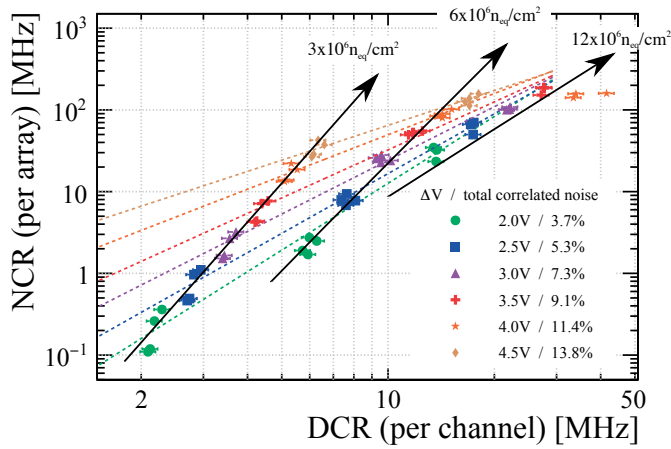


Figure 6.34: NCR as a function of DCR at threshold of 2.5/1.5/4.5 PE. Each dashed lines correspond to one  $\Delta V$  and therefore constant total correlated noise. Measurements taken with the SPIROC ASIC. Image taken from [73].

The variation of the NCR with the irradiation level is given in Tab.(6.1) for a readout with SPIROC and PACIFIC front-end shaping. The first has a 67 ns shaping and the second a 20 ns. It shows that the shaping time has an important effect on the NCR. It reduces the NCR by a factor 100 at  $3 \cdot 10^{11} \text{ n}_{\text{eq}}/\text{cm}^2$  and by factor  $\sim 60$  at  $6 \cdot 10^{11} \text{ n}_{\text{eq}}/\text{cm}^2$ .

<sup>7</sup>Noise saturation leading to noise clusters merging which reduces artificially the NCR

Irradiation level [ $10^{11} n_{eq}/cm^2$ ]	H2016_HRQ [MHz] @ $\Delta V = 3.5 V$	
	SPIROC	PACIFIC
3	11.4	0.1
6	50.8	0.85
12	157.9 <sup>7</sup>	4.06

Table 6.1: NCR comparison between SPIROC and PACIFIC for three different irradiation levels measured at  $\Delta V = 3.5 V$  and  $-40^\circ C$ . The effect of the fast shaping on the NCR is significant (factor 50-100 reduction).

### 6.3 Results for the KETEK K2015

The prototype run in 2015 was dedicated to test an additional epitaxial layer. The expected effect of a thin layer ( $0.4 \mu m$  or  $0.8 \mu m$ ) is a reduction in gain, a slight PDE shift toward the green and potential lower DCR after irradiation. The "wafer 4" is the reference, without epitaxial layer, implementation and "wafer 10" has an additional  $0.8 \mu m$  layer.

The  $V_{BD}$  for wafer 4 is  $34 V$  and its temperature coefficient  $34 mV/K$ . Its gain is  $1.73 \cdot 10^6 V^{-1}$  and can be seen in Fig.(6.35). Note that these values are significantly different from the Hamamatsu technology. The gain is 70% higher which causes a larger current (self heating for irradiated detectors) and a higher cross-talk. In comparison the  $V_{BD}$  of wafer 10 is  $43 V$  and has a temperature coefficient of  $39 mV/K$ . Its gain is  $1.55 \cdot 10^6 V^{-1}$ , which is smaller as expected.

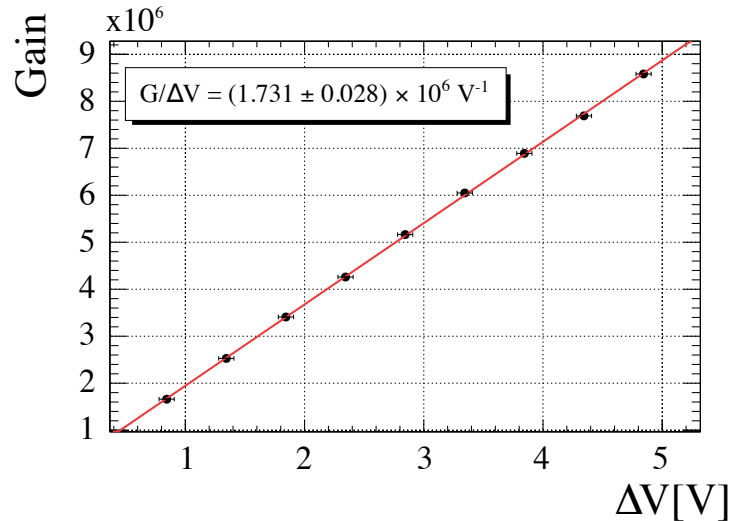


Figure 6.35: Gain as a function of  $\Delta V$  for one channel of wafer 4

Due to a manufacturing problem during the  $R_Q$  implementation, K2015 is unstable above  $\Delta V = 3.0 V$ . This results in a large increase of AP as shown in Fig.(6.36). Both wafers exhibit the same behaviour and have similar noise profiles.

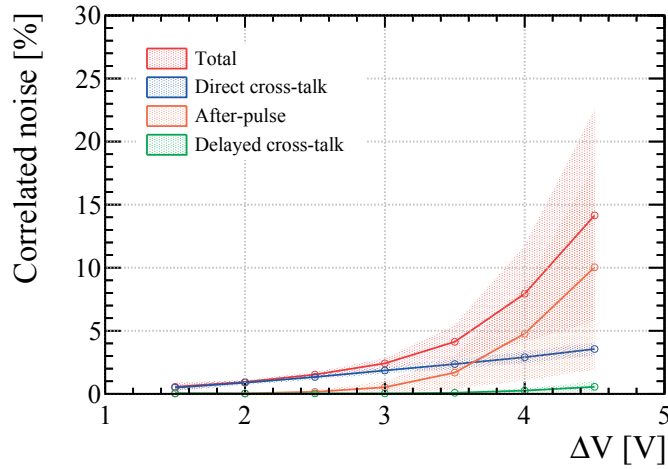


Figure 6.36: Wafer 4 noise characterisation. The noise characterisation has been performed at  $-10^{\circ}\text{C}$  to reduce DCR. No DeXT is seen in both wafer 4 and 10. The thresholds ( $\text{th}_{\text{AP}} = 0.5 \text{ PE}$ ,  $\text{th}_{\text{DeXT}} = 0.85 \text{ PE}$  and  $\text{th}_{\text{DiXT}} = 1.2 \text{ PE}$ ) are used.

Both wafers have a peak PDE of 45% at  $\Delta V = 3.5 \text{ V}$  at 420 nm. The sensitivity is less well matched to the fibre emission spectrum than H2017. An increased sensitivity for green light is still desired. The PDE for wafer 4 can be seen in Fig.(6.37).

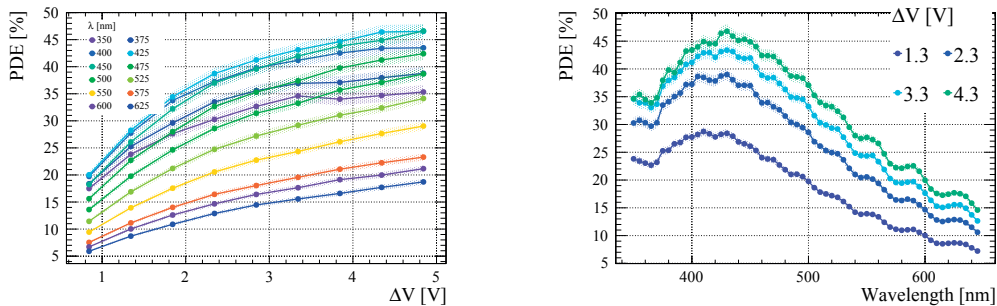


Figure 6.37: Wafer 4 PDE as a function of  $\Delta V$  (left) and wavelength (right). Wiggles in the PDE are resulting from the glass protection.

### 6.3.1 Irradiation results

Samples were irradiated with neutrons to a fluence of  $3 \cdot 10^{11} \text{ n}_{\text{eq}}/\text{cm}^2$  and annealed giving the results of Fig.(6.38) and Fig.(6.39) for wafer 4 and 10, respectively.

Wafer 4 is more stable at high  $\Delta V$  and allows operation up to 4 V. Comparing the DCR for different operation voltages and temperatures, a DCR saturation above 100 MHz is observed. This saturation is expected due to the relatively long recovery time (115 ns) and low number of pixels. This effect can be observed by the fit of  $K_{1/2}$  for wafer 4 at different  $\Delta V$ .

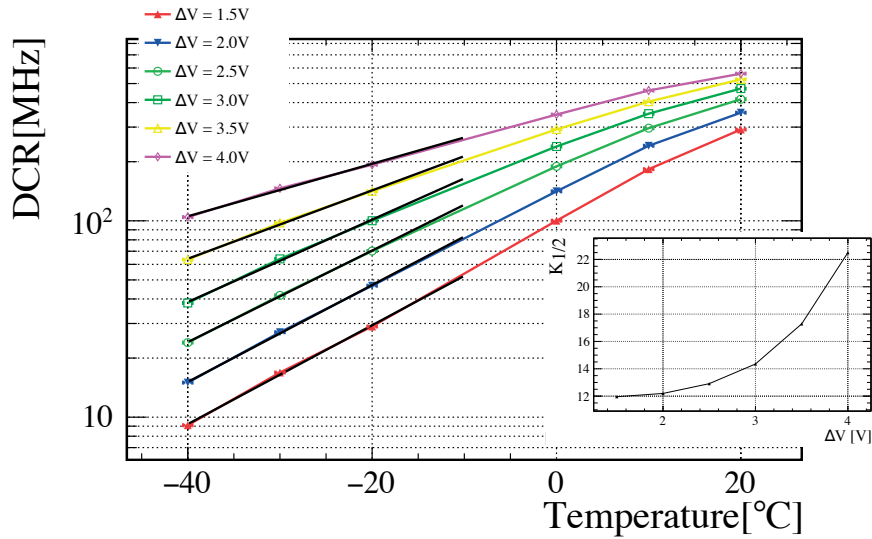


Figure 6.38: DCR measured as a function of the temperature for different  $\Delta V$  for wafer 4. The  $K_{1/2}$  as function of  $\Delta V$  is shown (right).

The DCR obtained for wafer 4 at  $-40^{\circ}\text{C}$  and  $\Delta V = 2.5\text{V}$  is 25 MHz which is a factor 2.5 higher compared to the 10 MHz of wafer 10 in the same conditions. It indicates that the epitaxial layer is efficient to reduce the DCR. For wafer 10, no pixel saturation is present at low temperature ( $-40^{\circ}\text{C}$  to  $-10^{\circ}\text{C}$ ) and low  $\Delta V$  leading to a  $K_{1/2}$  of  $10^{\circ}\text{C}$  identical to H2017.

The DCR for wafer 10 at ( $-40^{\circ}\text{C}$ ,  $\Delta V = 2.5\text{V}$ ) is a factor two higher than H2017 and DCR for wafer 4 is respectively five times higher.

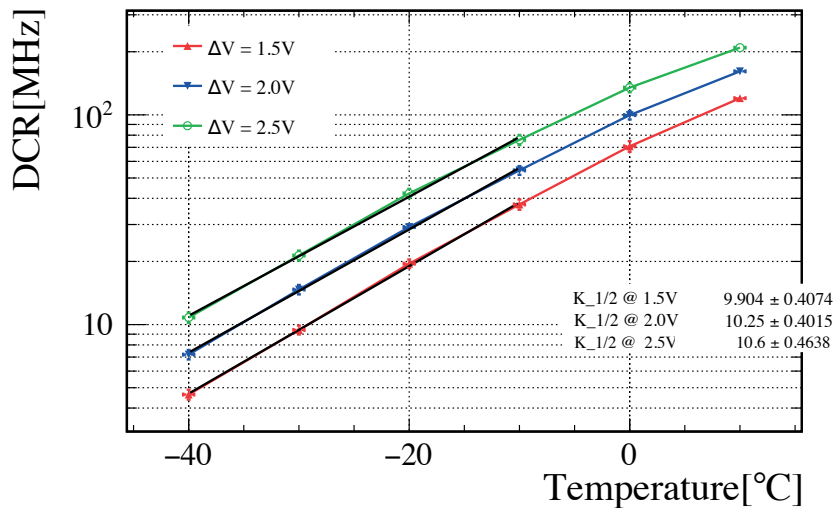


Figure 6.39: DCR measured as a function of the temperature for three  $\Delta V$  for wafer 10.



## 7 LHCb SciFi packaging and flex cable

This chapter describes the items interfacing the sensors with the readout electronics.

### 7.1 Kapton flex assembly



Figure 7.1: Kapton flex PCB assembly.

The Kapton flex PCB provides the connections to the front-end. The 128 channels SiPM array delivered by Hamamatsu is based on a small printed circuit board PCB hosting the two 64 channels SiPM dies. The package dimensions are  $6.5 \times 32.54 \times 1.6 \text{ mm}^3$  (L×W×H). The silicon dies are covered with a thin  $105 \mu\text{m}$  epoxy layer. On the front-end side of the flex PCB, two 80-pins, 0.5 mm pitch connectors<sup>1</sup> are placed. To reinforce the connector, an FR4 stiffener is glued on the backside and the pins are glued to the Kapton flex. On the detector side, a ceramic based stiffener is glued to the backside to reinforce the detector solder connections. A recess provides space for a Pt1000 temperature sensor as shown in Fig.(7.7). For bias voltage decoupling, the flex PCB hosts capacitors (two 0402 caps of 100 nF and 100 V) close to the detector as illustrated in Fig.(7.2).

---

<sup>1</sup>Hirose DV12-80DP-05V

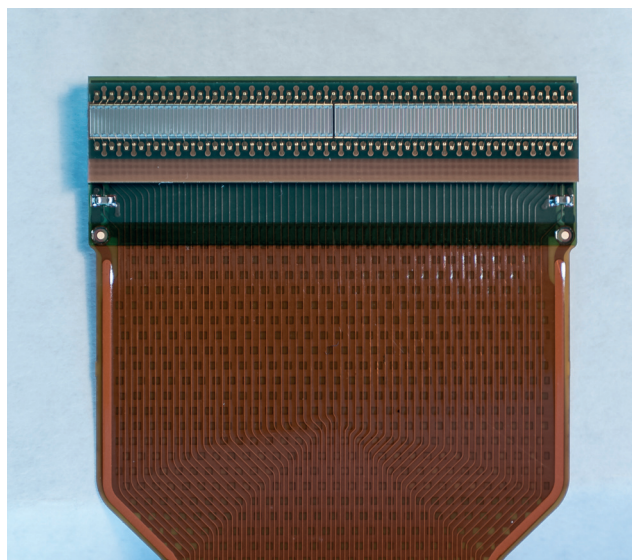


Figure 7.2: Decoupling capacitors close to the detector on the edges.

The Kapton flex PCB needs to fulfil the following requirements:

**Flexibility:** the flex cable undergoes vibrations and stress during the SciFi opening/closing for maintenance work. It needs to be sufficiently flexible to absorb the vibration without being damaged.

**Sufficient low heat conductivity:** the thermal transfers from the detector to outside has to be sufficiently low. The risk of water condensation must be minimised. It represents a large fraction of the total cooling power required (30%) for the present design.

**Temperature variation:** the flex has to cope with the thermal stress. The temperature changes between  $-40^{\circ}\text{C}$  during operation to  $+30^{\circ}\text{C}$  for annealing.

**Low impedance:** the traces need to have low impedance ( $50\ \Omega$ , single ended).

**Fast SiPM signal integrity:** the signal integrity for the fast signals has to be ensured while keeping the electrical cross-talk between adjacent signal lines below 10%.

**Bias voltage decoupling:** the bias voltage needs to be filtered. A decoupling capacitor close to the detector is required. The two bias lines serve the two 64 channel dies.

**SiPM temperature monitoring:** A Pt1000 temperature sensor is added on the detector back-side.

The flex PCB stack-up can be seen in Fig.(7.3). The ground plane in the middle is hashed to reduce the thermal conductivity and increase the flexibility. The flex circuits are produced in panels of eight for easier alignment and to simplify the soldering procedure and components



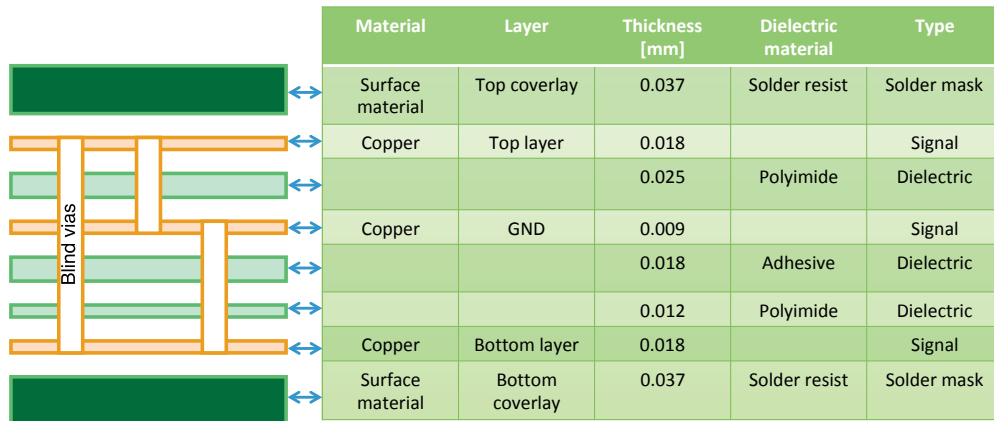


Figure 7.3: Kapton flex PCB stack-up and design.

placement. The top coverlay is removed in the region of the connectors and is replaced by a solder stop that can be aligned precisely.

A laser balling process ( $SB^2$ ) is performed by the company PacTech [74]. The balled detector, assembled on the flex PCB can be seen in Fig.(7.4). The 400  $\mu\text{m}$  diameter solder balls are made of an alloy (Sn63/Pb37). The balls are distributed and soldered on the SiPM with an infrared laser. The soldering process is illustrated in Fig.(7.5).

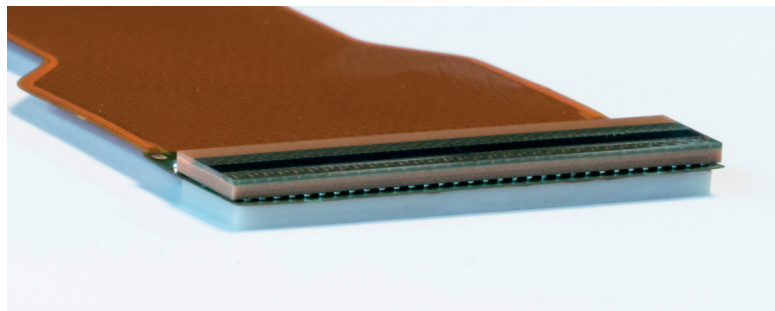


Figure 7.4: Assembled SiPM on the Kapton flex PCB using solder balls.

A total of 162 balls per SiPM chip are necessary. For the assembly of the balled SiPM on the flex, a Pb solder reflow process at 230°C is used. Shear tests and x-ray inspection are performed for quality control. An x-ray picture of the detector with the solder balls can be seen in Fig.(7.6). X-rays are able to detect short between adjacent solder balls. The optical window remain flat within 40  $\mu\text{m}$  as detailed in App.(B.2).

### 7.1.1 Ceramic stiffener and temperature sensor

A ceramic stiffeners is placed to ensure a good thermal contact between the cooling pipe and the SiPM while reinforcing the solder connection. The requirements for the stiffener are its flatness, a high thermal conductivity and a thermal expansion matching the silicon. A first test

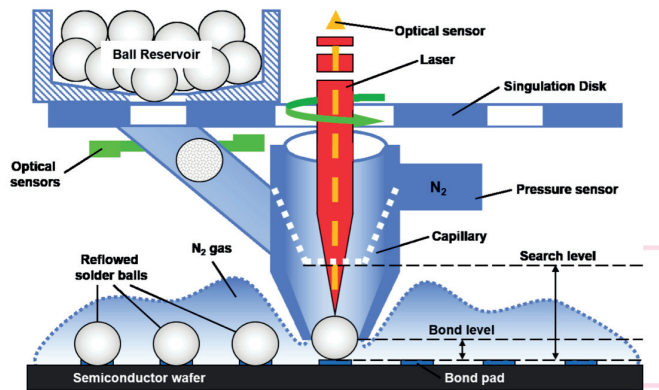


Figure 7.5: Illustration of the laser system used for the solder balling. Image taken from [74].

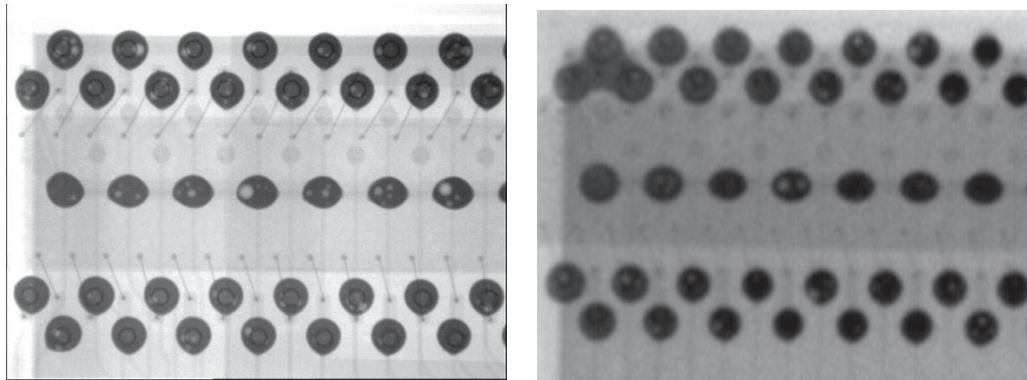


Figure 7.6: X-ray pictures of the solder balls. The bond wires of the detector are also visible. Right shows a short between three balls.

was performed with sintered MoCu (75/25). It was found that MoCu is difficult to machine, expensive, metal residual from machining were found and an oxidation layer made gluing unreliable. A ceramic stiffener based on aluminium nitride (AlN) was selected for the final packaging. It is a high thermal conductive sintered material (140W/mK) and has excellent mechanical properties. The glue used is Epotec (curing at 120°C) which supports a load up to 10 kg (limit established using the glue test presented in Sec.(7.2)).



Figure 7.7: Picture of the ceramic stiffener.

The choice of the temperature sensor is dictated by the temperature range of interest (-40°C

## 7.1. Kapton flex assembly

to +30°C) and by the required precision ( $\pm 1.0^\circ\text{C}$ ). A SMD mounting is also required. The sensor readout is performed with the GBT-SCA [75]. A constant current of  $100\ \mu\text{A}$  is applied and the voltage is measured with a 12-bit ADC in a range of 0 to 1 V. The voltage range limits the resistance value that can be measured. The difference between the true SiPM temperature ( $T_{\text{SiPM}}$ ) and the measured value ( $T_{\text{meas}}$ ) can be described by the following formula:

$$T_{\text{SiPM}} = T_{\text{meas}} - \Delta T_{\nabla} \pm \delta T_{\Delta R/R} - \Delta T_{\text{self.heat}} \pm \delta T_{\text{ADC}} \quad (7.1)$$

- $\Delta T_{\nabla}$  is due to the temperature gradient between the temperature sensor and the SiPM position. This term is neglected for the temperature sensor selection procedure.
- $\delta T_{\Delta R/R}$  is the tolerance on the value of the sensor resistance (given by the manufacturer).
- $\Delta T_{\text{self.heat}}$  is the increase of temperature due to self heating effects.
- $\delta T_{\text{ADC}}$  is the resolution of the 12-bit ADC on the voltage measurement where 1 LSB = 0.24 mV.

R(@-40°C) [Ω]	U (100μAA)	ΔR/R	Possible T range [°C]	ΔT <sub>ΔR/R</sub> [°C]	ΔT <sub>self.heat</sub> [°C]	ΔT <sub>ADC</sub> [°C]	ΔT <sub>tot.</sub> [°C]
Pt1K (Heraeus SMD 0603 Class B)							
842	84mV	0.12%	[-50,+50]	0.25	0.04	0.61	0.90
Pt10K (Heraeus SMD 0805 Class 2B)							
8.4k	840mV	0.24%	[-50,0]	0.50	~0.04	0.06	0.60
NTC 10k (TDK SMD 0603)							
190k	19V	1%	[+25,+50]	0.19	0.5	0.00	0.69
NTC 1k (TDK SMD 0603)							
34k	3.4V	5%	[-20,+50]	0.80	0.09	0.00	0.89
PTC 1k (Vishay SMD 0603)							
753	75mV	0.5%	[-50,+50]	1.70	~0.05	0.80	~2.6
PTC 5k (Vishay SMD 0805)							
3.77k	377mV	0.5%	[-50,+50]	1.70	~0.2	0.16	~2.1

blue = not optimal  
red = not acceptable  
green = selected probe

Figure 7.8: Comparison of temperature probes. The blue values are not optimal and the red are not acceptable.

Fig.(7.8) gives a comparison of probes based on the above parameters. The selected one is a Pt1000 from Heraeus.

## 7.2 Qualification and stress tests

The qualification and stress tests of the items supporting the SiPM are described in this section.

### 7.2.1 Thermal cycling of the flex PCB

This procedure was elaborated by the CERN bonding lab <sup>2</sup>. To test the reliability of a flex PCB it is recommended to perform 100 cycles between -55°C and +100°C. Three thermal cycling campaigns with 8 detectors each time were performed. No delamination or dead channels were found in any of the three test campaigns. During production, three cycles (-40°C to +80°C) are performed on all detectors for early failure detection by the assembly company (Valtronic).

### 7.2.2 Electrical cross-talk tests of the flex PCB

The electrical cross-talk is measured between two neighbouring channels on the flex. Both odd and even layers are tested. The full frequency spectrum is tested on 8 channel pairs out of 4 different detectors. A method has been developed where a DCR pulse is triggered and the signal in the neighbour channel is measured. This method uses the original SiPM pulse shape and gives a true cross-talk value.

All tests are performed at  $\Delta V = 3.5$  V. The results can be seen in Tab.(7.1) where the electrical cross-talk is found to be lower than 10% for all bandwidth as specified.

Bandwidth/x-talk	mean
Full bandwidth	(8.4±1.5)%
350 MHz	(7.7±1.6)%
200 MHz	(7.6±1.6)%

Table 7.1: Flex electrical cross-talk results for different bandwidth.

### 7.2.3 Mechanical tests of the connectors

To simulate the mechanical stress induced on the connectors during detector opening/closing, an x-y table is used. In the setup (shown in Fig.(7.9)) one side of the SiPM is connected to the readout electronic (VATA64) and the other side is clamped between two metallic piece attached to the moving head. The clamping is done at the same position as the SiPM clamping in the readout box. The expected maximal oscillation amplitudes are  $\pm 1$  mm in x and z direction and  $\pm 0.5$  mm in y.

Two flex prototypes were tested over 10,100 and 1000 cycles. The connector had no defects after all test cycles for x/y/z in the foreseen vibration ranges including x/y combined cycles. Crash

---

<sup>2</sup>We would like to thanks Florentina Manolescu from the bonding lab for her time and advices

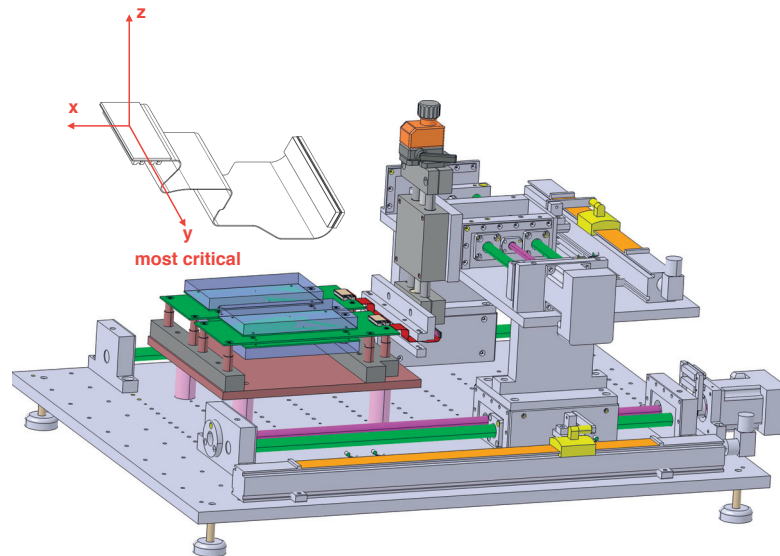


Figure 7.9: x-y table for vibrational tests. The detector is connected to the readout electronics for electrical contact verification. It is clamped between two metallic pieces attached to the moving x-y head.

tests were performed on the more critical y direction. After 700 cycles of  $\pm 1$  mm amplitude, broken channels were seen. For cycles of  $\pm 2$  mm, in less than 100 cycles more than 50% of the channels are disconnected.

#### 7.2.4 Scratch tests of the optical surface

The optical surface is pressed with a 10 N force against the fibres using springs attached to cooling bar. During temperature changes, the optical surface is expected to move with respect to the fibres. The consequences to the optical surface of such a movement was analysed.

The mechanical test setup presented in the previous section was modified to hold the SiPM at a fixed position. The fibre mat is attached to the x-y table and is pressed against the SiPM as shown in Fig.(7.10). A pressure of 14 N is applied to the SiPM against the fibre mat.

The test procedure consists of 20 cycles of  $100\ \mu\text{m}$  lateral displacement with a very slow movement speed to simulate the effect of temperature expansion. Colour-changing pressure contact paper<sup>3</sup> is used to check the quality of the contact between the fibres and the SiPM. An optical inspection was performed before and after the scratching test showing no visible marks on the detector.

<sup>3</sup>Surface pressure mapping sensors from Sensor Products inc.

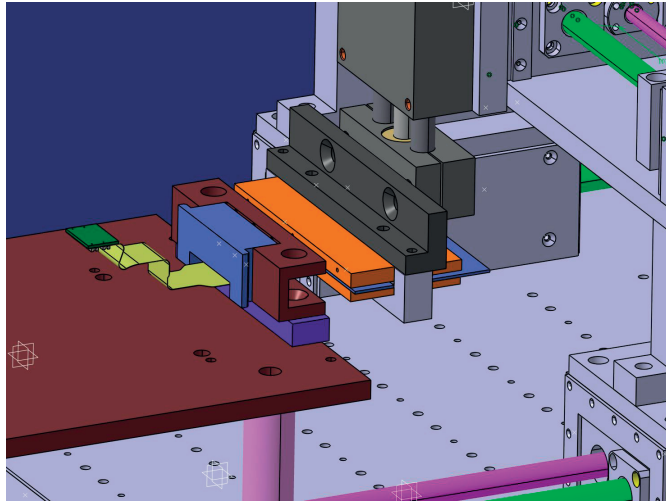


Figure 7.10: x-y table for the scratching test. Slow displacement of  $100\ \mu\text{m}$  are performed while the optical surface is pressed with a  $14\ \text{N}$  magnet against the fibres.

### 7.2.5 Glueing tests

The goal is to measure the resistance of the glue under traction and shearing forces. The setup shown in Fig.(7.11) was used to test different glues. The results for three different glues can be seen in Tab.(7.2)

Glue / Force	Traction	Shear
Transfer tape	$\sim 7.2\ \text{kg}$	$\sim 1.8\ \text{kg}$
Epotek 70E-4	No displacement up to $10\ \text{kg}$	No displacement up to $10\ \text{kg}$
Araldite 2031	No displacement up to $10\ \text{kg}$	No displacement up to $10\ \text{kg}$

Table 7.2: Glue test results. The Epotek 70E-4 and the Araldite 2031 successfully passed the stress test.

The Epotek 70E-4 glue has been selected for the SiPM production assembly.

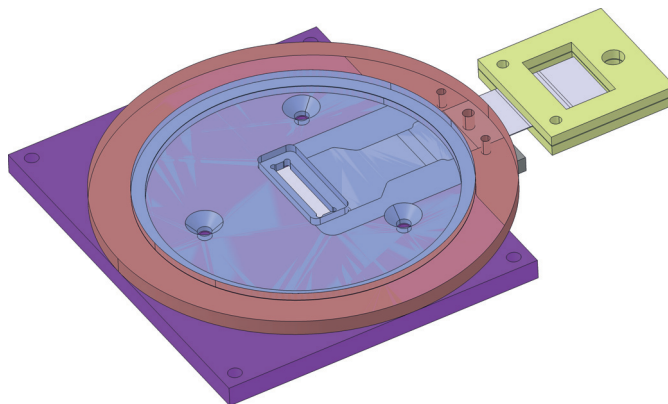


Figure 7.11: Glueing stress test setup.

### 7.3 Production quality control in Lausanne

The SiPMs undergo series of tests before being glued on the cooling bar and integrated in the cold box. The electrical connections are checked after the assembly (Valtronic) and at the delivery at EPFL. The  $V_{BD}$  is also measured for all 128 channels of each SiPM at EPFL. A light tight measurement box has been developed that allows a simultaneous measurement of 8 SiPMs. This setup allows a short measurement time (<10min) and a simple detector handling. It has an homogeneous light injection system and a temperature control system. The total thickness of the SiPM is measured using a microscope at three different points along the active surface (the two extremities and the center). The optical surface is inspected under a microscope. These tests include surface quality acceptance and qualification of the optical surface (scratches, hot drops, dirt particles). After the optical inspection, the devices are cleaned with isopropyl alcohol if needed. Detectors with similar mean  $V_{BD}$ ,  $V_{BD}$  spread and thickness are grouped in packs of four and sent to the assembly center to be glued on the cold bars.

A complete description of the production phases and the complete testing is given in App.(B). See also Fig.(7.12) for a flow-chart description.

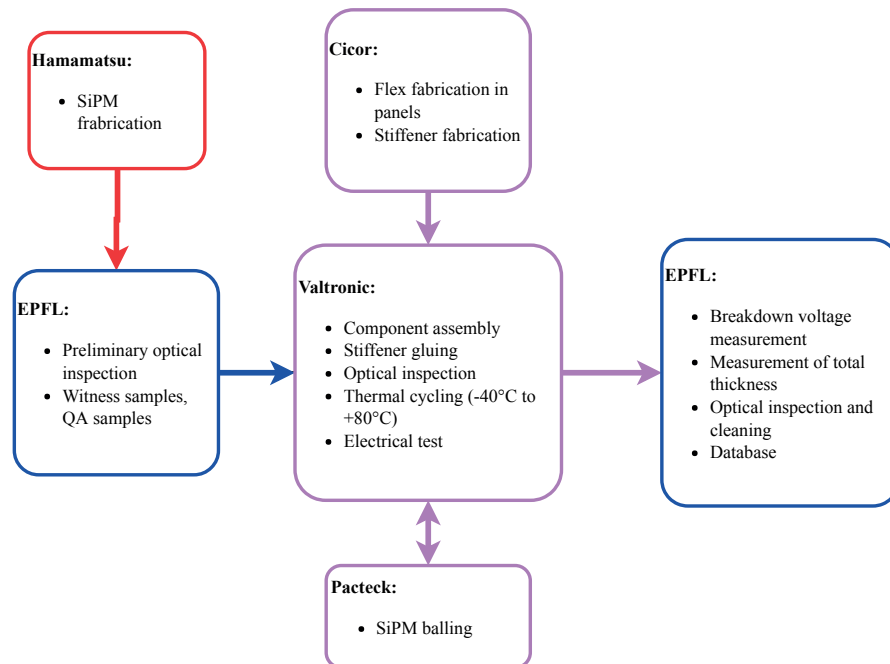


Figure 7.12: Main production steps for the different manufacturer companies and EPFL.





# 8 Improvements over the current detector

The SiPM packaging adopted for the LHCb upgrade can be improved to make the detector more mechanically robust and radiation hard. The following section presents possible improvements like micro-lenses, Through Silicon Via (TSV) and fast signal output. Micro-lenses improves the radiation hardness by reducing the active area for a given channel size. TSV allows for thinner optical entrance window and smaller mechanical tolerances leading to smaller chips. Finally the fast output acts as a filter for the slow component, reducing the current flowing in the front-end.

## 8.1 SiPM pixel implementation and micro-lens deposit

Previous sections have shown relations between active area, PDE and DCR. The only way the DCR can be reduced for a given channel size is to reduce the active area. To achieve this, micro-lenses can be deposit on the pixel to focus the light on the active area. A smaller area allows for lower gain (and so lower DiXT) and more space for trenches. A new pixel implementation with different geometries (round or hexagonal) can be considered. In a preliminary study, micro-lenses were deposited on a K2015 detector with a chequerboard geometry on the  $\sim 5 \mu\text{m}$  glass protective layer. The lenses are obtained by agglomerating liquid droplets of epoxy.

A preliminary simulation was performed to study the light collection from the lenses. The detector is modelled by a grid of  $3 \times 3$  pixels of size  $57.5 \mu\text{m} \times 62.5 \mu\text{m}$ . The fill factor is set to be 65%. The dead area is modelled as rectangles around the active areas as shown in Fig.(8.1). For the simulation, lenses are deposited directly on the silicon. To parametrise the lens, two parameters are needed,  $H_{\text{Lens}}$  and  $R_{\text{Lens}}$  which are illustrated in Fig.(8.2).

### 8.1.1 Micro-lens simulation

This section presents the main step of the simulation:

1. Generation of photons at the fibre end with the exit angular distribution of the SciFi

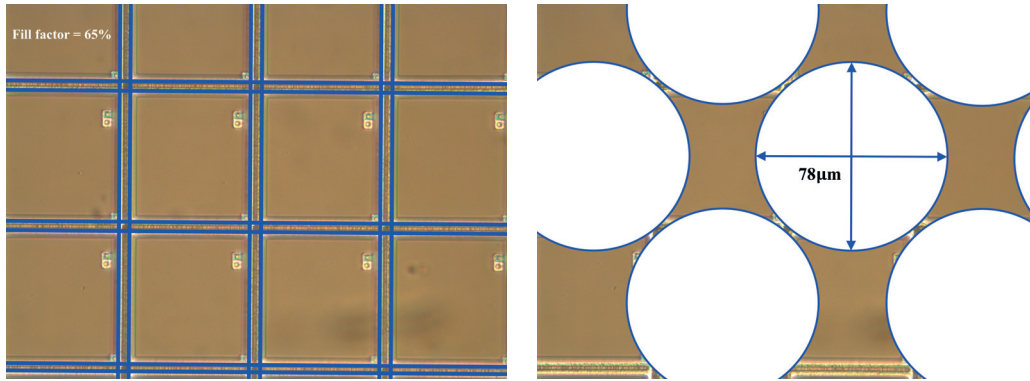


Figure 8.1: The fill factor and dead area definition of pixels (left) and chequerboard implementation of micro-lens (right).

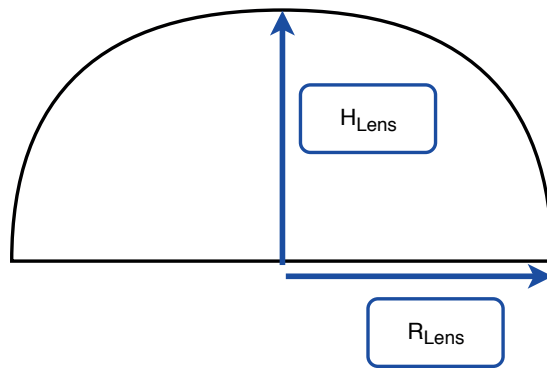


Figure 8.2: Simulated lens parametrisation using  $H_{Lens}$  and  $R_{Lens}$ . The lens is hemispherical when  $H_{Lens}$  and  $R_{Lens}$  are equal.

fibre [76].

2. Determination of the intersection points with the lens surface.
3. Transmissions or reflections at the lens surface and determination of the intersections with the silicon surface.
4. Determination of the hit positions on the pixel area (active or dead region).

All steps are described in details in App.(C).

The effect of the lens can be seen in Fig.(8.3). The lens has a focusing effect increasing the amount of detected light in the central pixel and depleting a circular region outside the active area. The radius and the ring thickness of the depleted ring can be tuned by changing  $H_{Lens}$  and  $R_{Lens}$ . Fig.(8.4) shows the light intensity for the active area and the dead area.

Tab.(8.1) summarises the corresponding fill factor (CFF) increase for different lens geometry. The highest CFF is obtained with  $39\ \mu\text{m}$  radius spherical lenses ( $H_{Lens} = R_{Lens}$ ). This results in

## 8.1. SiPM pixel implementation and micro-lens deposit

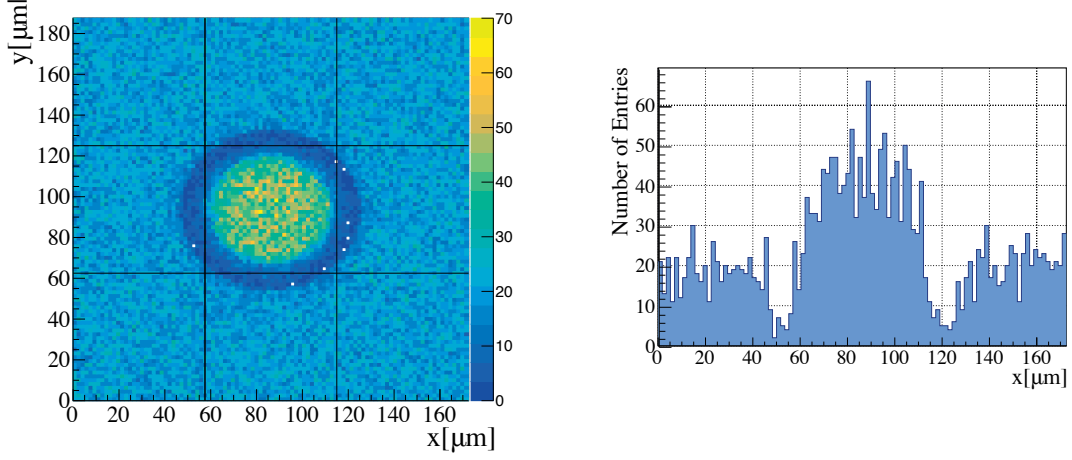


Figure 8.3: Distribution of photons on the  $3 \times 3$  pixel surface (left). The effect of the lens is seen as a depleted region around the central pixel as shown in the projection (right).

$R_{Lens} [\mu\text{m}]$	$H_{Lens} [\mu\text{m}]$	FF [%]	CFF 1 lens [%]	CFF 4.5 lenses [%]	Light increase [%]
36.0	36.0	65.0	69.17	83.76	28.86
37.0	37.0	65.0	69.26	84.17	29.49
38.0	38.0	65.0	69.31	84.39	29.83
39.0	39.0	65.0	69.33	84.48	29.96
39.0	34.4	65.5	68.67	81.51	25.40
39.0	29.6	65.0	67.99	78.45	20.69
40.0	40.0	65.0	69.17	83.76	28.85
41.0	41.0	65.0	69.09	83.40	28.30
42.0	42.0	65.0	68.53	80.88	24.43

Table 8.1: Results for different lens geometries. The best results are obtained with a half-sphere of  $39 \mu\text{m}$  radius (shown in green). The CFF increase drops significantly when the lens is not spherical (shown in orange).

a CFF of 84.5% corresponding to an increase of detected light in a SciFi tracker by 30%.

### 8.1.2 First iteration of lenses deposition

In collaboration with the microsystems laboratory (Prof. J. Brugger<sup>1</sup>, EPFL [77]) the deposition of micro-lenses on a KETEK detector was performed. A piezo-actuated inkjet printer was used for the deposition. The working principle of the inkjet printer can be found in [78]. The droplets are made of 100 pL of Ink-Epo (refractive index  $\sim 1.55$ ) and are deposited with a  $50 \mu\text{m}$  diameter nozzle. Six drops are required to obtain a lens of 134 pL volume since a shrinkage after the solvent evaporation is expected to be of 70%. The lenses must be separated or the

<sup>1</sup>We would like to thanks Prof. Brugger and his student Mohammad Mahdi Kiaee for their help to perform this first trial.

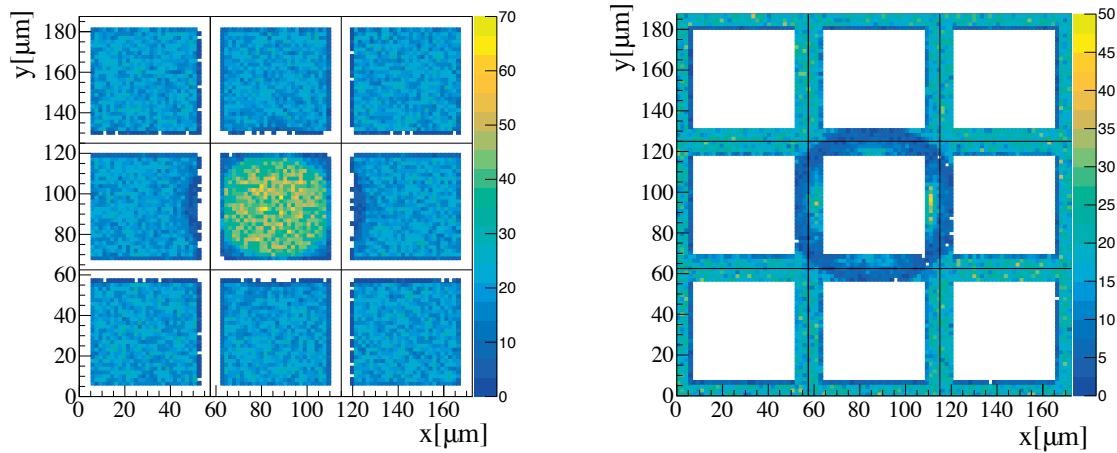


Figure 8.4: Light intensity on the active area (left) and the dead area (right).

droplets agglomerate before having the time to dry out.

Two SiPM samples were prepared for the first trial. The first sample had no surface treatment. The second sample was treated with trimethylchlorosilane (TMCS) in order to homogenise the surface and make it more hydrophobic. Both samples were cleaned in isopropyl alcohol and deionised water and dried with nitrogen. The result of the first deposit can be seen in Fig.(8.5)

The first deposit failed due to a non-flat surface. A profilometry study showed that the pixel structure is not flat but has a  $3\ \mu\text{m}$  groove structure as shown in Fig.(8.6). This structures constrained the droplet and prevented a good wetting of the surface.

In conclusion deposition with liquid droplets is not possible and other fabrication processes must be considered.

## 8.2 Through Silicon Via

The current bond wires impose a protection layer (optical window) of at least  $100\ \mu\text{m}$ . This window represents a technological challenge for the manufacturing and handling (cleaning and scratches). Micro-lenses require a very thin protection window ( $1\text{-}2\ \mu\text{m}$ ). The TSV technology is a solution to replace the bond wires. The process allows a package with small cutting tolerances and therefore small dead regions between adjacent SiPM arrays. It is compatible with a standard lead-free reflow solder process [79].

The electrical connection is implemented by passing to the backside through holes in the silicon. The TSV technology was not available for H2017 but it is the choice for future developments.

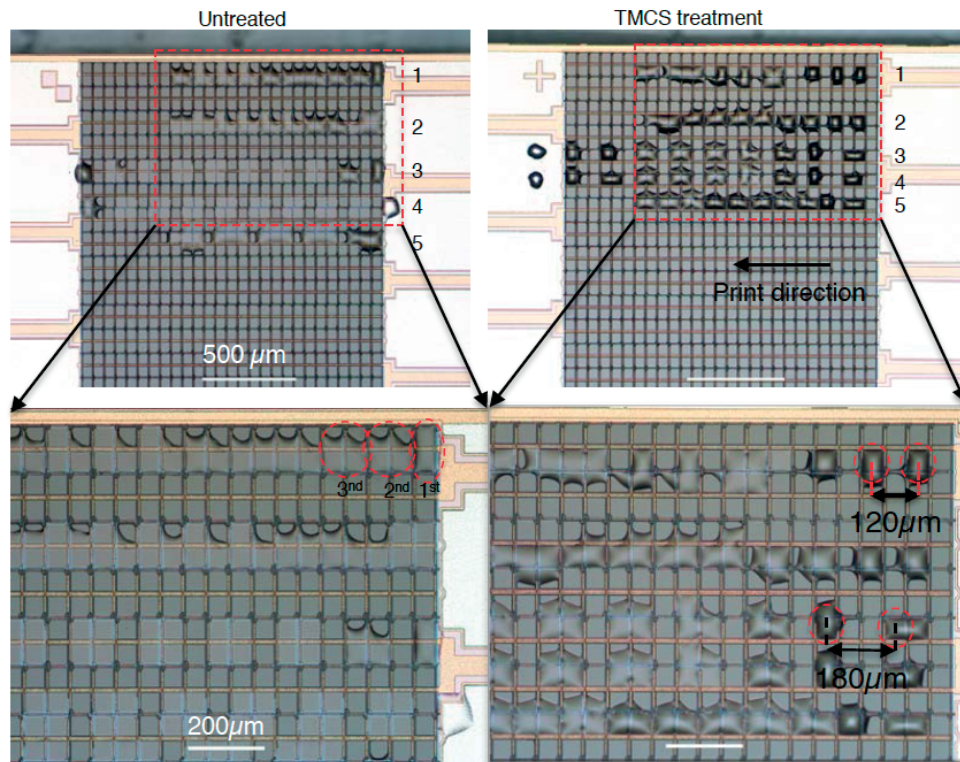


Figure 8.5: Results of the first micro-lens deposit on the two SiPM samples. Due to the pixel profile, droplets started to agglomerate. Image taken from [77].

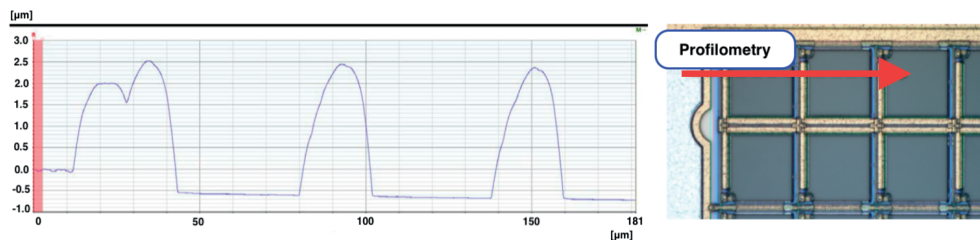


Figure 8.6: Profilometry showing the surface height along a scanned line. Grooves of  $3\ \mu\text{m}$  are present. Image taken from [77].

Without the epoxy protection, the silicon still has to be passivated to avoid corrosion from humidity. This can be performed by a lithographic glass deposit technology successfully tested with the KETEK detectors.

### 8.3 Fast pulse output

Only the fast part of the signal of the SiPM can be used in our application, timed by the 40 MHz LHCb frequency. To remove the slow component a filter is implemented in the PACIFIC chip. SensL has developed a fast readout of the signal with a capacitive coupling [79]. An

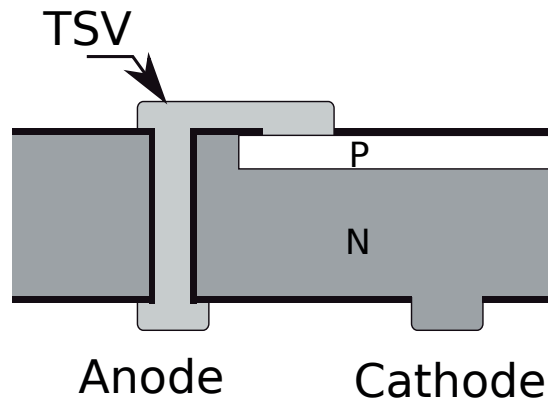


Figure 8.7: TSV cross section illustration. Image taken from [80].

illustration of the fast output can be seen in Fig.(8.8). This feature is interesting for SiPM timing applications. The FWHM of the fast output pulse width is in the 1 ns level . This implementation also allows to reduce the current sinking in the front-end electronic.

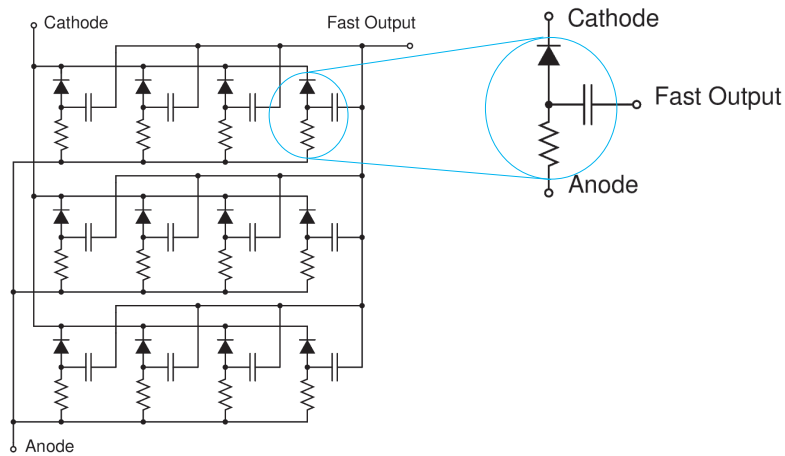


Figure 8.8: The capacitively coupled fast output illustration. Each SiPM pixel is illustrated as a diode. Image taken from [79].

## 9 Tests in beam and simulation

Our testbeam campaigns were aimed to understand the performances of the scintillating fibre modules in terms of light yield, attenuation length, spatial resolution and hit efficiency [81].

A SciFi based beam telescope was developed and build for beam instrumentation. Its conception, construction and calibration as well as the subsequent data analysis was a major contribution of my PhD thesis work.

The SciFi beam telescope and the main results obtained during the testbeam campaigns are presented in this chapter and the results are compared with a simulation.

### 9.1 The SciFi beam telescope

A modular beam telescope based on scintillating fibres is used to reconstruct the particle tracks. This allows to measure the resolution and hit detection efficiency of a device under test (DUT). The DUTs were often the 2.5 m long LHCb-SciFi modules but other applications are presented in the following. The telescope is illustrated in Fig.(9.1) and a picture can be seen in Fig.(9.2).

It consists of two boxes each containing two tracking stations where one is placed upstream and the other downstream of the DUT. Each station consists of two 10 cm long SciFi planes oriented to measure x and y coordinates transverse to the beam. Each plane is read out by one H2017 SiPM resulting on an active detection area of  $32.5 \times 32.5 \text{ mm}^2$ . A light injection system based on LEDs is installed between each stations for gain calibration and time alignment. The SiPMs can be read out by either the VATA64 or the SPIROC front-end chip. The electronics limit the readout frequency to 1 kHz. A trigger system based on scintillators read out with wavelength shifter fibres are placed within the enclosure of the telescope at both the entry and the exit of the beam. The light detection uses single channel SiPMs<sup>1</sup>. The two trigger stations are working in coincidence.

---

<sup>1</sup>Hamamatsu S12571-050

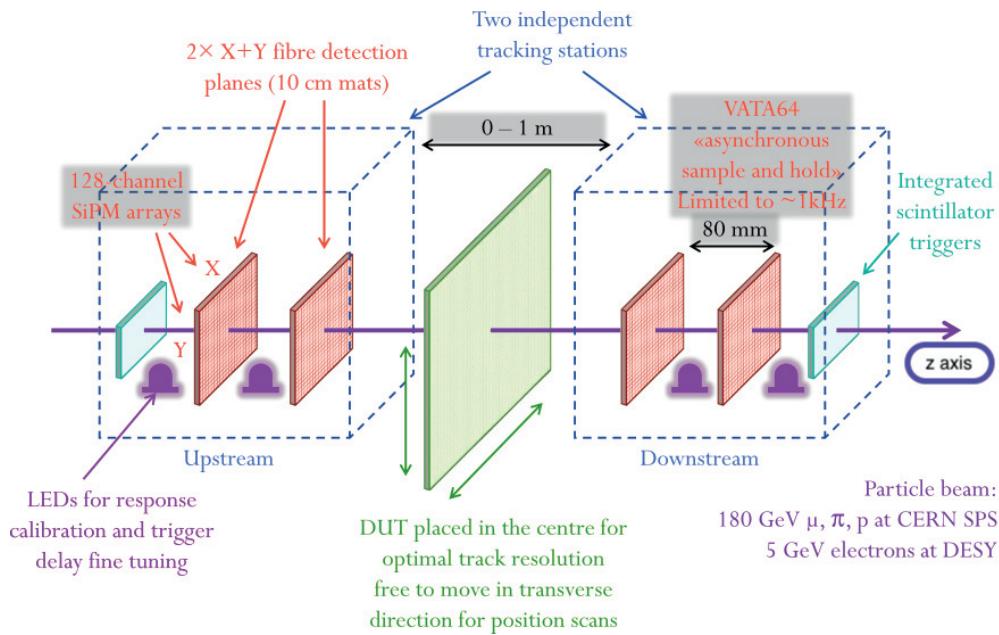


Figure 9.1: Illustration of the SciFi telescope showing the two trigger stations, the four fibre detection planes, the DUT plane and the LED calibration system. Illustration taken from [82].

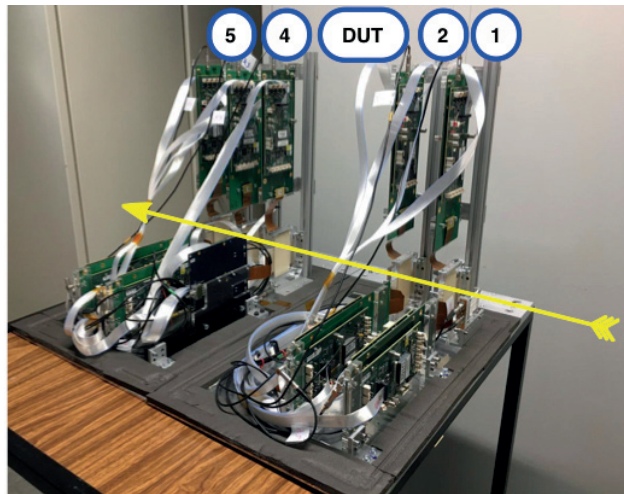


Figure 9.2: Picture of the SciFi telescope showing the 4 tracking stations. A fifth station is added as a DUT. The beam trajectory is illustrated with the yellow arrow. Picture taken from [83]

An alignment of the two telescope boxes is possible using a mechanical system. For a more precise alignment, an off-line alignment procedure calculates the shifts of the x and y planes in the x or y direction respectively, while the z position is fixed. The external planes (X1, Y1, X5 and Y5) are also kept fixed. Corrections for plane rotation are not implemented. The small mechanical tolerances during the construction and the small beam spot allows this approximation. A full description of the alignment procedure is presented in [71]. The 10-bit



clustering algorithm is used by default but a modified algorithm (called Anti-kt) has also been studied. The performances of different clustering algorithms can be found in [84].

### 9.1.1 Hit detection efficiency and spatial resolution

The telescope was used to characterise small DUTs identical to the stations of the telescope. The measurement were performed at the CERN SPS facility with 180 GeV proton, pion and muon beams.

**The hit detection efficiency:** is defined as the ratio between the number of events containing a hit at the expected position and the total number of events. The hits of the four stations in the telescope are used to reconstruct the track. The hit position at the DUT is computed from the track and is accepted if the corresponding cluster position is within  $\pm 0.5$  mm from the interpolated value. The hit efficiency is found close to 100% as expected even at low  $\Delta V$ , as it can be seen for the DUT results in Fig.(9.4).

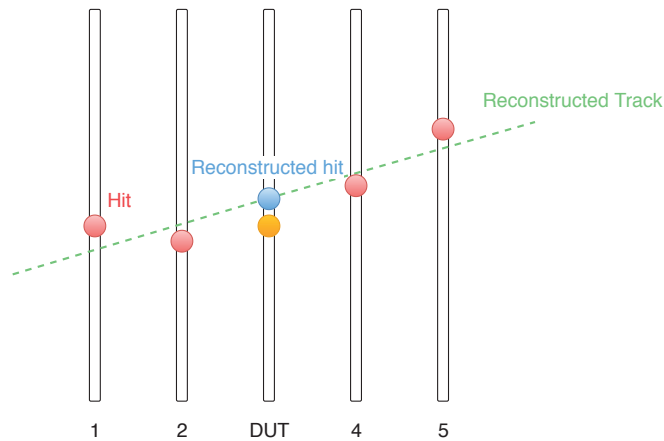


Figure 9.3: Scheme of the track reconstruction. The red hits are used for the track reconstruction, the orange hit represents the hit on the DUT and the blue dot is the hit computed from the reconstructed track.

A small inefficiency is observed at high  $\Delta V$  as well as a drop due to lower PDE (light yield) for smaller  $\Delta V$ . The main reason of a so high efficiency is the high light yield in such short fibres.

**The spatial resolution:** is computed from the residual, defined as the distance between the hit on the DUT station and the interpolated hit,  $R = x_{\text{hit}} - x_{\text{track}}$ .

The distribution of the residual is the convolution of the distribution of the hits, which has a standard deviation  $\sigma_h$ , and the distribution of the extrapolated hits, of standard deviation  $\sigma_t$ .  $\sigma_h$  corresponds to the spatial hit resolution and  $\sigma_t$  the track resolution. During the

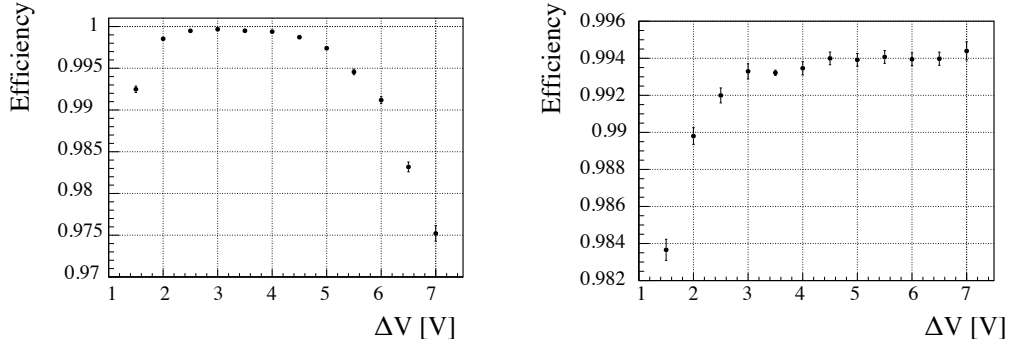


Figure 9.4: Hit detection efficiency of the x (left) and y (right) DUT planes as a function of  $\Delta V$ . All other stations are operated at  $\Delta V = 3.5$  V. The x station shows an efficiency drop for high  $\Delta V$ . This effect is caused by the VATA64 chip due to high current surge. In the right plot, the SPIROC was used to demonstrate the origin of this effect. The difference in maximum efficiency between the two stations is due to the SiPM die gap present in the injection region of the y station. Figure taken from [83].

measurement only the combined resolution:

$$\sigma_R = \sqrt{\sigma_h^2 + \sigma_t^2} \quad (9.1)$$

is accessible, with  $\sigma_R$  the standard deviation of the residual distribution (see example in Fig.(9.5)). The distribution is fitted with a double-sided Crystall-Ball function. A  $\Delta V$  scan was performed on the DUT station while leaving all other stations at  $\Delta V = 3.5$  V, i.e. keeping the telescope track resolution constant. The resulting  $\Delta V$  dependences of  $\sigma_R$  of the DUT can be seen in Fig.(9.5).

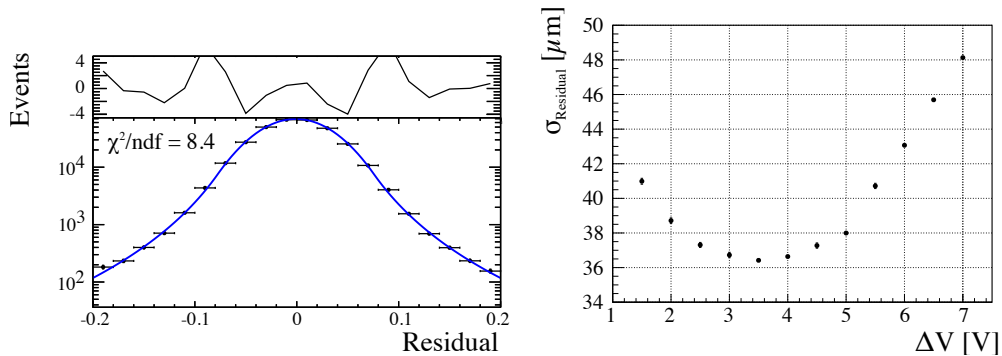


Figure 9.5: On the left the residual distribution of the x plane of DUT at  $\Delta V = 3.5$  V is shown. The distribution is fitted with a double Crystall-Ball function. On the right  $\sigma_R$  as a function of  $\Delta V$  is shown. The plot shows a minimum of  $\sim 36$   $\mu\text{m}$  at  $\Delta V = 3.5$  V. Figure taken from [83].

For low  $\Delta V$  (low PDE) the single hit resolution decreases and as a consequence the thresh-

olds for neighbour channels is not reached. For high  $\Delta V$ , the calculated cluster position is significantly affected by the effect of the correlated noise and electronic saturation.

$\sigma_h$  can be calculated from  $\sigma_t$  using equation (9.1), where  $\sigma_t$  is found to be  $16\ \mu\text{m}$  from the simulation described in [85]. This results in a  $\sigma_h$  of  $33\ \mu\text{m}$  at  $\Delta V$  of  $3.5\ \text{V}$ .

## 9.2 SciFi Testbeam campaign

This section focuses on the latest testbeam results obtained on the LHCb long fibre modules at CERN and DESY. For the measurements taken at the SPS H8 beamline located in the North Area of CERN (Fig.(2.1)), the beam is about 1 cm wide and is composed of 180 GeV pions and protons [86]. The particle rate is  $10^5 - 10^6\ \text{Hz}$  but the data acquisition rate is limited to 1 kHz. The DESY facility in Hamburg provides a  $\sim 1\ \text{cm}$  wide beam of electrons with an energy from 1 to 6 GeV at a rate of 1 kHz.

Various beam telescope were used during the testbeam campaigns. These telescopes are silicon strip detectors of the type of the AMS silicons strip ladders, the VeLo TimePix telescope and the SciFi telescope presented previously. A summary of the measurement performed is presented App.(D).

### 9.2.1 Testbeam latest results

This section shows the results obtained during the 2017 DESY testbeam campaigns. Presented results are taken from [86, 87, 88, 89]. Light yield measurement using SPIROC on irradiated and non-irradiated modules have been performed as well as tests with the PACIFIC chip. To synchronise the asynchronous beam to the synchronous 40 MHz PACIFIC clock, an additional TDC is required to select in-time events. This leads to a loss of 95% of the recorded tracks. The setup can be seen in Fig.(9.6)

Two 2.5 m LHCb modules were installed between the two SciFi telescope boxes. One of the module had been irradiated with protons at the CERN PS accelerator to reproduce the expected maximal LHCb irradiation profile and dose close to the beam-pipe. The setup was installed on an adjustable table for the module scanning.

**Light yield of irradiated and non-irradiated modules comparison:** The light yield with thresholds (0.5, 1.5, 1.5) was measured with the SPIROC only since the PACIFIC readout does not allow amplitude measurements. Note that the set of threshold chosen is unrealistic regarding noise for the SciFi operation and would need to be set higher resulting in a loss of light yield. The background was suppressed by selecting tracks from the beam telescope with the following conditions:

- All layers of the telescope have exactly one cluster.

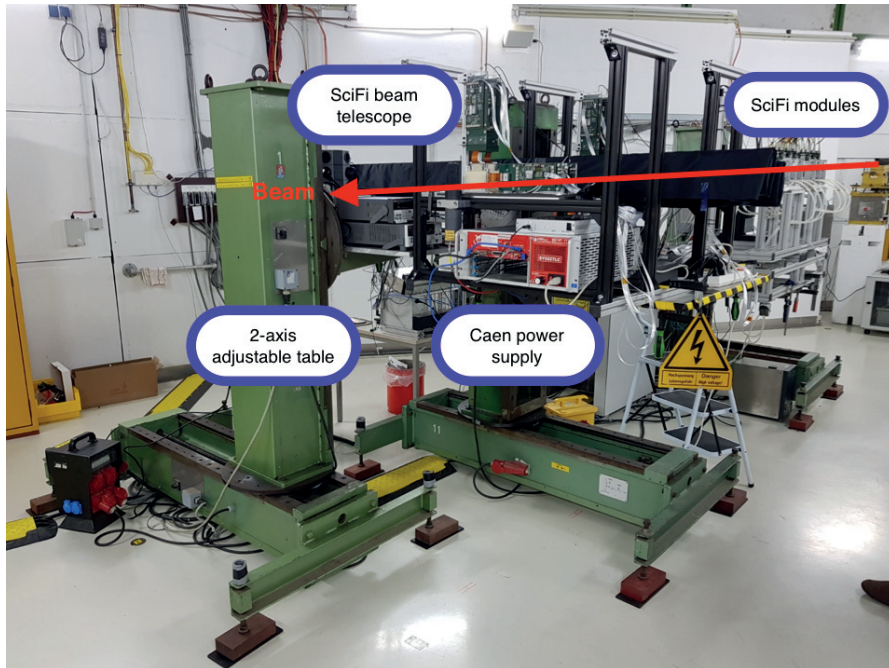


Figure 9.6: DESY testbeam setup. Two long fibre modules were installed between the two SciFi telescope boxes. Image taken from [87].

- The fit  $\chi/\text{ndf}$  on the track is better than 4.
- The cluster is within  $\pm 1$  mm of the interpolated position.

With this tight selection, 50 % of the tracks are rejected.

The light yield for irradiated and non-irradiated modules can be found in Fig.(9.7). It is 18.5 for non-irradiated modules at  $\Delta V = 3.5$  V close to the mirror. Note that the light yield for protons in the same condition was found to be 16.3 [81].

For an irradiated module, the observed light yield is 40% lower (11.0) as expected from preliminary measurements. Note that the light yield is depending on the annealing of the fibres, a 60% drop is expected without annealing.

**Hit detection efficiency using SPIROC and PACIFIC:** The hit detection efficiency was measured using the SPIROC and PACIFIC at three different thresholds sets: (0.5, 1.5, 2.5), (1.5, 2.5, 3.5) and (1.5, 2.5, 4.5). Tracks were obtained using the SciFi telescope with the same conditions applied for the light yield measurement. Fig.(9.8) shows a comparison between the hit efficiency for SPIROC and PACIFIC on the irradiated and non-irradiated fibre module as a function of  $\Delta V$ . The difference is given in Tab.(9.1).

A baseline shift was observed for high light injection intensity. This effect is related to the

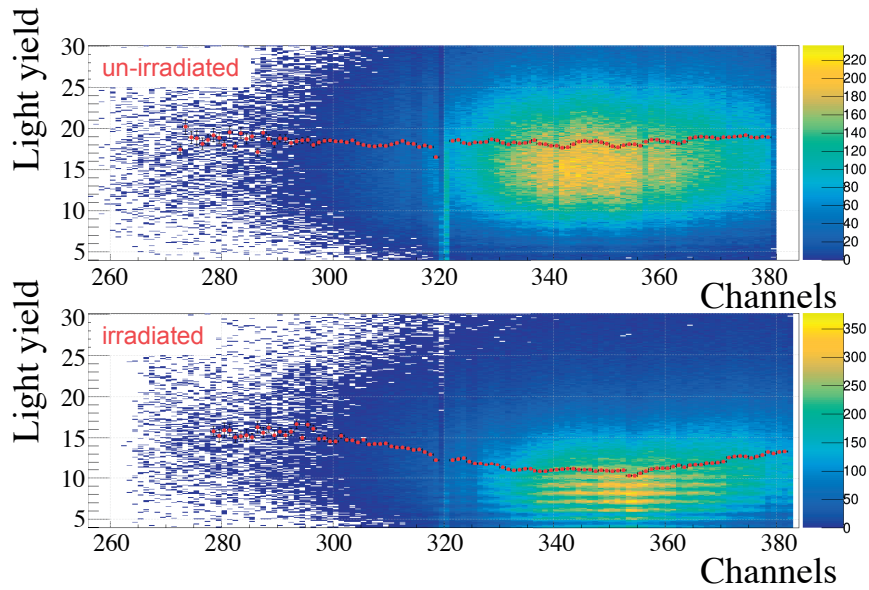


Figure 9.7: Irradiated and non-irradiated long fibre module readout by SPIROC. The light yield drops from 18.5 to  $\sim 11.0$  at  $\Delta V = 3.5$  V. A set of low threshold were used (0.5, 1.5, 1.5) and electrons injected close the mat mirror. Image taken from [87].

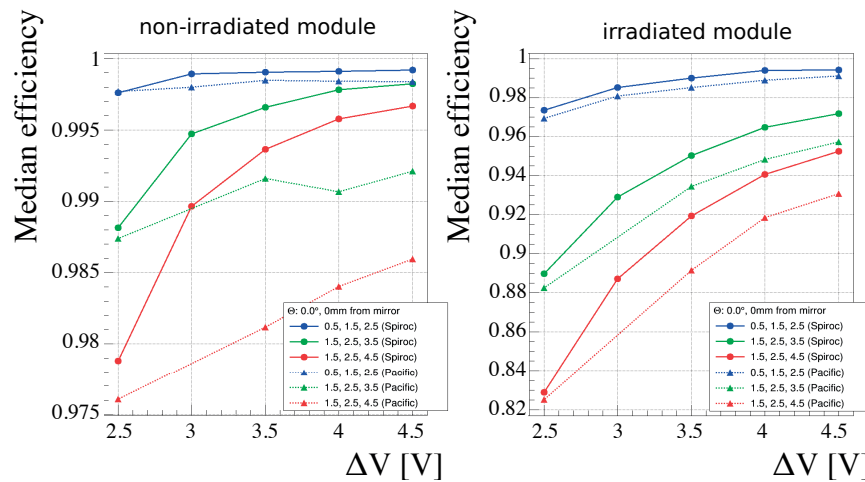


Figure 9.8:  $\Delta V$  scan of the hit efficiency for the non-irradiated (left) and irradiated (right) module using the SPIROC and PACIFIC readout for different sets of thresholds. Figure taken from [87].

decoupling of the bias power supply of the SiPM. Filtering capacitors were subsequently added in the final flex versions, as seen in Chap.(7). The efficiency as a function of the light yield, obtained by combining results from irradiated and non-irradiated mats, is shown in Fig.(9.9).

**Spatial resolution:** The residuals for irradiated and non-irradiated modules are shown in Fig.(9.10). The weighted cluster position was calculated with the 2-bit clustering algorithm

Threshold	SPIROC	PACIFIC
0.5, 1.5, 2.5	99.92%	99.89%
1.5, 2.5, 3.5	99.67%	99.19%
1.5, 2.5, 4.5	99.38%	98.19%

Table 9.1: Hit efficiency for a non-irradiated module for three threshold sets. The 1% lower hit efficiency for the PACIFIC has been explained by a wrong photon calibration.

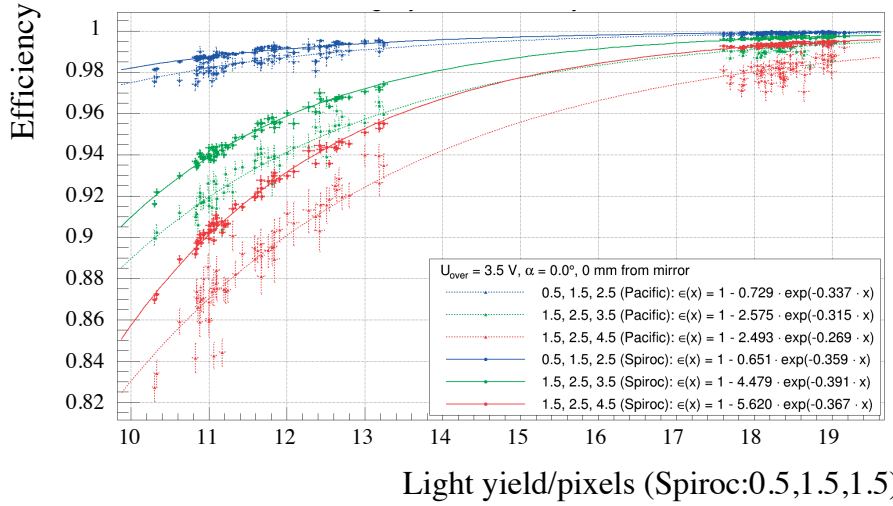


Figure 9.9: Hit efficiency as a function of the light yield. The light yield is computed using the SPIROC at thresholds (0.5,1.5,1.5) and is compared to the efficiency for different threshold sets and readout electronics at  $\Delta V = 3.5$  V. Figure taken from [87].

identically for the PACIFIC and the SPIROC. The residuals are fitted with a double Gaussian and are comparable for both readouts and are found only weakly  $\Delta V$  dependent.

The testbeam campaigns with protons in 2015 showed residuals of  $\sim 64 \mu\text{m}$  compared to the  $\sim 100 \mu\text{m}$  with the electrons at DESY. The residuals are affected by the contribution of multiple scattering.

### 9.3 Simulation of a SciFi detector and comparison with experimental results

The simulation framework is written in C++ to reproduce the SciFi detector behaviour, from the particle energy deposit in the fibre to the particle position reconstruction. The simulation program can be tuned for specific detector geometries, fibre characteristics, SiPM technologies and readout electronics. Note that sometimes the parameter values do not represent physical values but are effective values. The main steps of the simulation are:

**Particle generation and energy deposition in the fibres:** Each simulated event corresponds

### 9.3. Simulation of a SciFi detector and comparison with experimental results

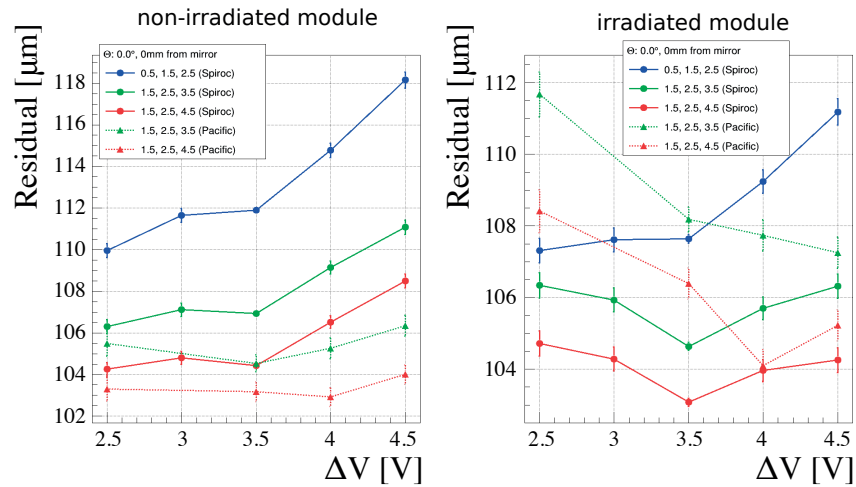


Figure 9.10: Residuals for the non-irradiated (left) and irradiated (right) module using the SPIROC and PACIFIC readout for different set threshold as a function of  $\Delta V$ . Figure taken from [87].

to an incident particle traversing the fibre mat. Particles are generated with an initial position and an incident angle. The number of generated photon is proportional to the path length in the active region of the fibre. Only the core of the fibre is active while 6% of the fibre radius corresponding to the double cladding is inactive. The mean number of photons generated in the fibre follows a Landau distribution defined by the mean and the FWHM of the distribution.

**Light transmission in the fibres:** The number of trapped particles is given by the Brewster angle. Only 10.8% of the photons are trapped in the fibres. To simulate the UV photon cross-talk, non trapped photons can interact with neighbouring fibres with a given probability. A higher probability value is given to photons travelling to "diagonal" fibres, which are closer to the emitting fibre, due to the limited amount of absorbing glue as depicted in Fig.(9.11). The mirror reflectivity is simulated by a Poisson process.

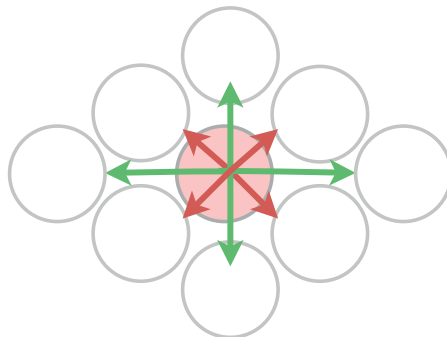


Figure 9.11: Illustration of the fibre cross-talk. Red arrows are the dominant source of fibre cross-talk.

**Light transmission to the detector:** The photon exit angle distribution from the fibres follows the distribution presented in App.(C.1). The light is propagated through a thin air gap and traverses the epoxy layer of the SiPM entrance window. Dead zones of the photodetector are implemented.

**Noise generation in the SiPM and signal shaping:** DiXT, AP and DCR are simulated in detail. The DeXT noise (known since H2015) is neglected. The correlated noise arrival time is tuned following the results shown in Sec.(6.2). The goal is to be able to simulate irradiated detectors including its noise and the response of different readout electronics. Random overlap is important to fully simulate the behaviour of irradiated detectors.

**Analysis and noise clusters:** The simulated data can be used to compare with experimental light yield, cluster size, efficiency and resolution. Both 10-bit and the 2-bit clustering algorithm can be selected.

The simulation results are compared to the testbeam data for 2.5 m long fibre module from May 2015. The mean of the energy deposit and the fibre cross-talk parameters are varied to find the best match with the testbeam data at all three injection points. Examples can be seen in Fig.(9.12). One set of parameters (represented in yellow in the figures) models accurately the light yield and the cluster size from the testbeam. Data taken with the beam at three different points on the fibre module (2.50 m, 1.25 m and 0.30 m from the SiPM position) are used. The noise has almost no effect for non-irradiated detectors and is neglected. The data differences compared to simulation in cluster size, can be explained by the model used for the light output angle. For measurement points closer than 30 cm to the SiPM, the short attenuation length start influencing the results. This effect was neglected in the simulation.



### 9.3. Simulation of a SciFi detector and comparison with experimental results

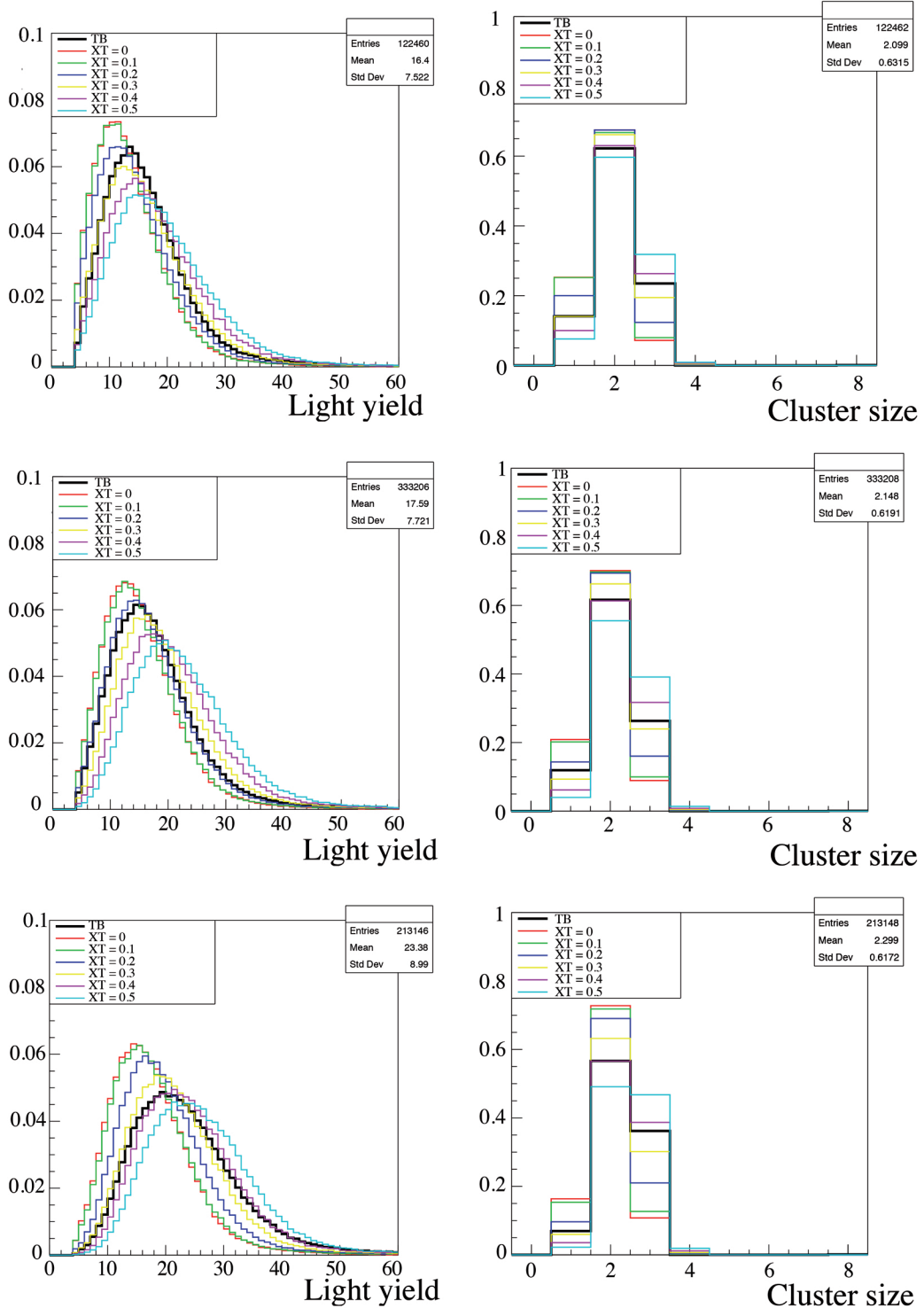


Figure 9.12: Light yield and cluster size comparison for a measurement point distant from the SiPM of 225cm (top), 125cm (middle) and 30cm (bottom). The testbeam data is shown in black as a reference. The cross-talk probability of 0.3% fits the light yield and cluster size for 225 cm and 125 cm. Only for the 30 cm point, the short attenuation length results in slightly worse results.



## 10 Conclusion

This work has presented the different SiPM technologies developed for the LHCb SciFi Tracker Upgrade. Methods to measure the electrical and mechanical properties of the sensors have been described. The results on devices from two companies, Hamamatsu and KETEK, have been discussed. In the end the SiPMs by Hamamatsu have been preferred. By its high intrinsic gain ( $10^6$ ) and photo detection efficiency of 45% over the fibre emission spectrum, the chosen devices are ideal for low light applications. The DCR obtained (14 MHz) at the end of the expected lifetime, corresponding to  $50 \text{ fb}^{-1}$  integrated luminosity in LHCb, the low total correlated noise probability (7%), the fast readout and the efficient noise suppression results in a NCR of 0.85 MHz which fulfils the LHCb requirements.

In LHCb, the SiPMs are mounted on a flex PCB. The quality control techniques have been discussed. At the time of this work, 20% of the total 5500 SiPMs have been tested and categorised as a function of their electrical and optical properties. No major defects have been seen. The LHCb SciFi tracker modules are in production and the commissioning of the detector is foreseen for end 2019.

This work has shown the potential of SiPMs in low light applications which is important in SciFi based tracking systems. An application for beam tracking instrumentation was presented. A single hit spatial resolution of  $36 \mu\text{m}$  and almost 100% hit detection efficiency were achieved.

A simulation program has been written to reproduce a SciFi detector behaviour, from the particle energy deposit in the fibre to the particle position reconstruction. The simulation can be tuned for specific detector geometries, fibre characteristics, SiPM technology and front-end electronics. The program was validated by testbeam data.

We have examined the possibility to improve the SciFi performance by adding micro-lenses to each pixel. A simulation has shown that micro-lenses have an excellent potential to improve the SiPM performances in a radiation environment. The DCR can be reduced for a given channel size by reducing the pixel active area allowing also space for more efficient trenches to reduce the correlated noise. The reduction of  $G/\Delta V$  is desirable to limit the sources of

## **Chapter 10. Conclusion**

---

noise DiXT, DeXT and AP which are proportional to the gain. The micro-lens implementation requires to replace wire bondings by a new connection scheme simplifying at the same time the packaging (TSV).

# A Experimental methods

## A.1 Pulse shape time dependent measurements

One of the key features to allow these measurements is to have a sufficient signal to noise ratio. The method was originally developed for small size SiPMs with a typical area of  $0.4 \text{ mm}^2$  and  $\text{DCR} < 50 \text{ kHz}$  ( $\tau_{\text{DCR}} = 1/\text{DCR} = 20 \text{ }\mu\text{s}$ ) at room temperature. In this case, the small DCR allows to acquire data in a sampling window of  $t_{\text{sample}} = 200 \text{ ns}$  with a low probability of a second random dark pulse falling in the same time window. The  $R_T$  value is  $R_T = 200 \text{ ns}/20 \text{ }\mu\text{s} = 1\%$ . To extend this method to larger devices with higher DCR it is necessary to work at low temperature. Changing the temperature affects the DCR but also, in a moderate way, AP. For certain devices, differences on the PDE are also observed [90]. Note also that the detector characterisation should be performed at relatively low rate to avoid significant contributions from random dark pulses in the sampling window.

**Additional details on the setup:** The pulse shape measurements are performed inside an electromagnetic interference (EMI) shielded enclosure to ensure high signal-to-noise ratio. The detector is read out with a high bandwidth voltage preamplifier ( $2.5 \text{ GHz}$ ,  $20$  or  $40 \text{ dBV}^1$ ) and a  $1 \text{ GHz}$  oscilloscope ( $20 \text{ GS/s}$ )<sup>2</sup>. The detector is mounted on a PCB avoiding wire pins or cables to minimise serial inductance and the associated ringing.

The bias voltage filtering is provided by a serial  $1 \text{ k}\Omega$  resistor and two parallel ceramic capacitors ( $100 \text{ nF}$  and  $1 \text{ }\mu\text{F}$ ) mounted close to the detector. The box containing the device is equipped with a cooling system which allows to reach  $-60^\circ\text{C}$  temperature at the SiPM location. The bias voltage sourcemeter<sup>3</sup> and the oscilloscope are controlled and readout using Python routines. The current and a large number of DCR pulses are recorded at different bias voltages  $V_{\text{bias}}$ . The recorded waveforms are analysed using a program in C++ and ROOT [91].

---

<sup>1</sup>FEMTO, HSA-X-2-20, HSA-X-2-40

<sup>2</sup>LeCroy, WAVERUNNER 104MXI

<sup>3</sup>Keithley 2400

## Appendix A. Experimental methods

---

The analysis of the data recorded at different  $V_{\text{bias}}$  allows to calculate  $V_{\text{BD}}$ . Since  $V_{\text{BD}}$  is calculated for every measurement, the characterisation does not require a specific temperature. Only DCR measurement, which strongly depends on the temperature, has to be made at standard 25°C.

### A.2 Correlated noise corrections for the PDE

PDE based on current measurements need a precise correction procedure to account for the correlated noise. The corrections can only be made accurate for high  $\Delta V$ , where correlated noise probabilities are more than 10%, only if the correction for higher order correlated noise are introduced (e.g. AP of DiXT and AP of DeXT). With the waveform analysis presented in Chap.(6), the higher order corrections can be determined. Events with two and more pulses after the primary avalanche are classified and counted as higher order contributions. The average charge  $w_{\text{h.o.}}$  in such pulses and the probability  $p_{\text{h.o.}}$  of their occurrence are made available. Note that the DiXT probability accounts for single and higher order DiXT. The mean amplitude can be used instead of a 1 PE if necessary.

The relation between the current measured on the SiPM,  $I^*$ , and the different noise contributions are expressed by the following equation<sup>4</sup>:

$$I^* = I \cdot [1 + (1 \cdot p_{\text{DeXT}}) + (1 \cdot p_{\text{DiXT}}) + (w_{\text{AP}} \cdot p_{\text{AP}}) + (w_{\text{h.o.}} \cdot p_{\text{h.o.}})] = \frac{I}{(1 - r_{\text{curr}})} \quad (\text{A.1})$$

where  $I$  is the current measured corrected for correlated noise and  $r_{\text{curr}}$  is the correlated noise correction factor (calculated from the waveform analysis results). Equation (A.1) is valid for a current produced by light or by dark noise.

The current produced by light is equal to the total recorded current corrected by the dark current leading to:

$$I_{\text{light}} = (I_{\text{total}} - I_{\text{dark}}^*) \cdot (1 - r_{\text{curr}}) \quad (\text{A.2})$$

In equation (A.2),  $I_{\text{total}}$  is measured with injected light and  $I_{\text{dark}}$  without light. The PDE can finally be computed with the photo-current corrected for noise by equation (A.2), the SiPM gain and the ratio of the active surfaces

$$\text{PDE} = Q_{\text{EPD}} \cdot \frac{I_{\text{light}}}{G \cdot I_{\text{PD}}} \cdot \frac{A_{\text{PD}}}{A_{\text{SiPM}}} \quad (\text{A.3})$$

---

<sup>4</sup>The asterisk indicates that these values also contain a fraction of correlated noise induced pulses

where  $I_{PD}$  is the current of the calibrated photodiode.

The most important aspects of the correction accounting for correlated noise are discussed in the following.  $p_{AP}$  is usually given in literature for 0.5 PE. Here it is calculated for a higher threshold of 0.6 PE in the waveform analysis to gain robustness for a multichannel automated measurement. To fully account for the current produced by AP, the following weight is applied:  $w_{AP}^{0.6} = 7.2$  for a cut at 0.6 PE, resulting from numerical integration.

A consideration has to be made regarding multiple direct cross-talk. As explained before, SiPM detectors with a signal shape with a pronounced fast component and an almost ten times smaller slow component, the amplitude of DiXT pulses rarely reaches 2 PE. Delays of 100 ps are sufficient to reduce the amplitude of the fast component significantly below 2 PE. A threshold of 1.17 PE is used to select DiXT pulses. The detection of multiple DiXT cannot be achieved by the amplitude selection because they rarely add up to a fast component larger than 2 PE. The estimated size reaches 1% for a  $p_{DiXT}$  of 10% and can be neglected.

The amplitude of delayed 1 PE pulses is baseline shifted by the slow component of the primary pulse. DiXT produced by these pulses cannot easily be discriminated. As a consequence, the effect of DiXT on delayed pulses is currently not taken into account for the corrections. The estimated error is of order of 0.5% for a correlated noise probability of 10%. With the above consideration,  $r_{curr}$  can be calculated from:

$$r_{curr} = \frac{N_{\text{delayed pulses}}}{N_{ev} + N_{\text{delayed pulses}}} + (w_{AP}^{0.6} - 1) \cdot p_{AP}^{0.6} + p_{DiXT} \quad (A.4)$$

where  $N_{\text{delayed pulses}}$  is the number of delayed pulses exceeding the threshold and  $N_{ev}$  is the total number of waveforms recorded.

For the PDE based on pulse frequency method corrections, similar considerations are made. The recorded frequency is the sum of the light induced pulses,  $f_{\text{light}}^*$ , and dark pulses,  $f_{\text{dark}}^*$ :

$$f^* = f \cdot (1 + p_{AP}^{0.6} + p_{DeXT} + p_{h.o.}) \quad (A.5)$$

where  $f$  is the frequency of the primary pulses (light or dark count) and  $p_{h.o.}$  is the probability for higher order delayed correlated noise to occur and pass the threshold. The frequency of primary photons  $f_{\text{light}}$  is therefore measured as:

$$f_{\text{light}} = f_{\text{light}}^* \cdot (1 - r_{\text{freq}}) = (f_{\text{total}} - f_{\text{dark}}^*) \cdot (1 - r_{\text{freq}}) \quad (A.6)$$

## Appendix A. Experimental methods

---

The parameter  $r_{\text{freq}}$  is the fraction of pulses due to delayed correlated noise. The DiXT pulses are only counted as one pulse and do not require any correction. Precise values for  $r_{\text{freq}}$  are obtained from the pulse-shape analysis applied on dark pulses. It is computed as:

$$r_{\text{freq}} = \frac{N_{\text{delayed pulses}}}{N_{\text{ev}} + N_{\text{delayed pulses}}} \quad (\text{A.7})$$

where  $N_{\text{delayed pulses}}$  is the number of delayed pulses exceeding the threshold and  $N_{\text{ev}}$  is the total number of waveforms recorded. The PDE of the SiPM can be calculated by:

$$\text{PDE} = \text{QE}_{\text{PD}} \cdot \frac{f_{\text{light}}}{I_{\text{PD}}/e} \cdot \frac{A_{\text{PD}}}{A_{\text{SiPM}}} \quad (\text{A.8})$$

which uses the current of the photodiode and its gain  $G = 1$  for the calculation.

### A.3 PDE measurement setup additional informations:

The light source is composed of a Xe lamp and a monochromator<sup>5</sup> remotely controlled by a step motor. The monochromator allows a  $\pm 1$  nm wavelength selection from the Xe lamp spectrum, which covers from 200 nm to 750 nm. The monochromator light is sent into an optical fibre (550  $\mu\text{m}$  diameter) to transport the light source into the EMI-shielded and thermally controlled enclosure. A light diffuser is used at a sufficiently long distance of the measurement point to homogenise the light beam. The calibration of the luminous power surface density ( $P_{\text{lum}}$ ) of the light beam is made by a calibrated photodiode<sup>6</sup>.

The photodiode is sensitive to the range of 160 to 900 nm and its current is read by a picoammeter<sup>7</sup>. It requires a relatively high luminous intensity compared to the high gain SiPM. The calibration of  $P_{\text{lum}}$  is more precise for higher photodiode current resulting from a higher luminous power. On the other hand, to avoid the SiPM saturation,  $P_{\text{lum}}$  has to be several orders of magnitudes lower than for the photodiode. The adjustment of the light intensity is made in such a way that the photodiode receives sufficient luminous power for the calibration while the SiPM much less to avoid saturation. For a wavelength range from 370 nm to 620 nm the available luminous power is sufficient when the detectors are spaced from the diffuser by 200 mm.

The large sensitive area of the photodiode (10.3 mm diameter) is necessary to reach 1% precision for a minimal optical power of 100 pW. The relationship between  $P_{\text{lum}}$  and the rate of

---

<sup>5</sup>H10-UV Yvon Jobin

<sup>6</sup>Newport 818-UV

<sup>7</sup>Keithley 6485



### A.3. PDE measurement setup additional informations:

incident photons  $R$ , is:  $P_{\text{lum}} = \frac{R}{A} \cdot \frac{hc}{\lambda}$ , where  $A$  is the sensitive area and  $\lambda$  the wavelength. The luminous power density can also be calculated from the measured photocurrent using the relation  $I = S_k \cdot A \cdot P_{\text{lum}}$ , where  $S_k$  is the radiant sensitivity, given by the manufacturer calibration curve. Instead of the radiant sensitivity, the quantum efficiency,  $QE = S_k \cdot \frac{hc}{\lambda \cdot e}$ , can be used. With a distance of  $d = 200$  mm, the surface of the photodiode  $A = 83.3$  mm<sup>2</sup>, the resulting  $P_{\text{lum}}$  is in the range of 1.25 to 5 pW/mm<sup>2</sup> depending on the wavelength.

During the measurement, the SiPM is placed vertically, in such a way that its center corresponds with the center of the light spot. The uniformity of the light intensity has been measured by displacing the light beam using a x/y/z positioning stage. In a range of  $\pm 10$  mm around the peak position,  $P_{\text{lum}}$  is changing less than 10% and less than 2% for  $\pm 5$  mm. The measurement was repeated at different wavelengths knowing that the optical coupling and diffusion has some wavelength dependency. In Fig.(A.1) the result for six different wavelengths is shown.

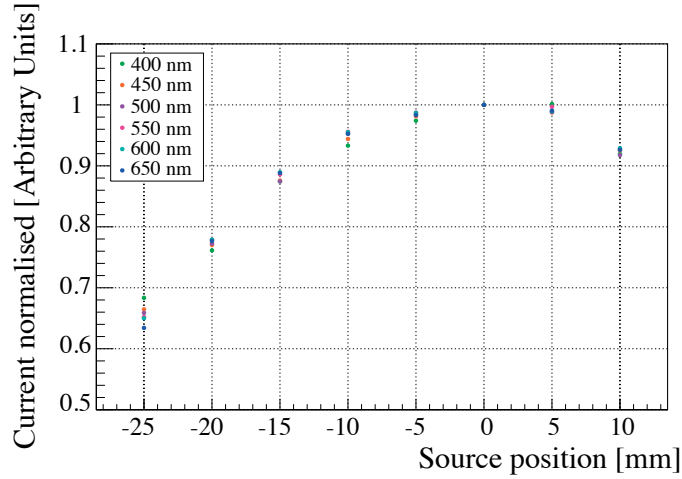


Figure A.1: Light intensity profile in the detection plane perpendicular to the beam. Measured with the Newport 818-UV photodiode at six different wavelengths.

**Light beam intensity:** As described in the section presenting the PDE setup above, a uniform and calibrated light beam is needed. A low intensity is kept sufficiently low such that saturation or the effect of pixel recovery time can be neglected. For devices with low number of pixels ( $\sim 100$ ) the light intensity has to be tuned such that less than one pixel at a time is recovering. As an example, for a recovery time of  $\tau_{\text{rec}} = 84$  ns, the rate of detected photons  $R = 1/(3 \cdot \tau_{\text{rec}}) \approx 4$  MHz should not be exceeded. For devices with large number of pixels ( $>1000$ ), the rate can be increased to the level where saturation due to pixel occupation is below the desired error. The pulse frequency method, already described, is a threshold depending counting method. It is well suited to devices with low number of pixel because it is based on single pulse counting. Since random overlap of pulses generate wrong counting, the intensity needs to be adjusted sufficiently low. For large devices, the measurement method based on the current is more suitable.

**Statistical and systematic uncertainties:** For the current-based PDE measurement method, two dominating sources of systematic uncertainties related to the setup and three for the corrections and the gain computation have been identified. The photodiode calibration has a 1% precision leading to a 1% uncertainty on the beam intensity. This value is estimated at the peak wavelength. In addition, the accuracy of the positioning of the photodiode and the SiPM in the light beam introduces the second major uncertainty. The accuracy of the positioning along the beam axis is crucial since the intensity depends quadratically on this distance. Assuming  $d = 200 \pm 2$  mm, a 2% uncertainty is obtained. The homogeneity in the plane perpendicular to the light beam has been evaluated and found that for a position accuracy of  $\pm 0.5$  mm the total systematic uncertainty is smaller than 1%. With a multichannel array the measurement for different channels displaced by 4 mm was repeated and confirmed the homogeneity measurement.

On the correlated noise computation side, the corrections suffer from growing systematic errors as the rate of correlated noise increases. For a total correlated noise below 10% the correction has a systematic uncertainty that influences the PDE by less than 1%. The uncertainty is expected to increase with correlated noise.

Finally, the dominant contribution to the uncertainty of the current based PDE measurement is linked to the gain measurement. With the method described, an accuracy of 1% can be achieved with the temperature stabilised at better than 0.5 K over the full measurement period. In the wavelength regions with high photon sensitivity, total systematic uncertainty is dominant over the statistical one, while in low sensitivity regions and low  $\Delta V$ , the statistical dominates. In conclusion, the current based PDE method has a total estimated error of 6% of which one third is caused by the gain measurement.

For the frequency based PDE measurement method, the sources of uncertainty are identical as for the current method but with two advantages regarding the systematic error. First, the correction for correlated noise is computed simply by counting pulses and the DiXT probability is not used. Second, the gain is not used in the PDE calculation which eliminates its error as well as its dependence to temperature. Overall, the total uncertainty is taken to be 3.5%.

### A.4 IV setup additional informations:

The IV characteristics measurement does not require a fast acquisition system and is implemented with standard test equipment. A Keithley 2612B<sup>8</sup> source meter together with a multiplexer system<sup>9</sup> is used to automatise the measurements for multichannel devices. The system is controlled via a Labview program. A temperature controllable enclosure is added to the setup for DCR temperature dependency characterisation. To reach  $-50^\circ\text{C}$  using a liquid

---

<sup>8</sup>The Keithley series 2600 is not a good choice for SiPM pulse shape measurements and characterisation. This series introduces significant noise spikes from its own power supply into the test equipment, the 2400 series are the preferred choice.

<sup>9</sup>Keithley 3706A-NFP

## A.5. Test setup with short SciFi module and electron-gun

chiller coupled to a heat spreader, the volume inside the cooling enclosure was reduced to a minimum.

To increase the precision on the measurement of the reverse bias region, a homogeneous light source can be placed in the otherwise light shielded box. A scratched blue LED, embedded in a matte plexiglas bar, is placed on top of the detector for a homogeneous continuous light injection. The level of light homogeneity is  $\sim 10\%$  as illustrated in Fig.(A.2).

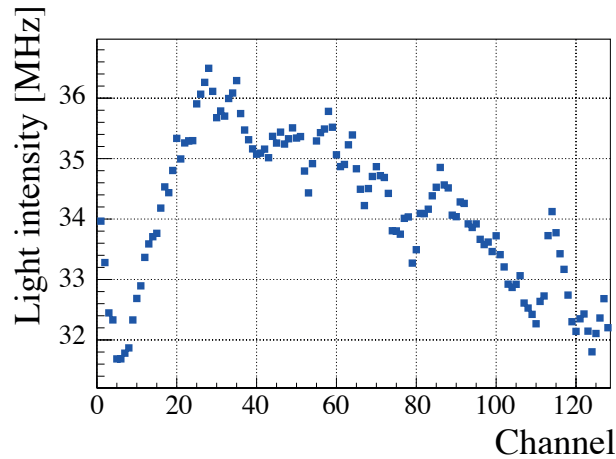


Figure A.2: Light intensity profile after continuous light injection. The overall light homogeneity is better than 10% variations.

## A.5 Test setup with short SciFi module and electron-gun

The setup consists of a prototype fibre module (originally a prototype of the beam gas vertex, BGV, [92] installed at CERN). It consists of a 34 cm long 5 layers fibre module, with glued mirror. The device comprises a cooling system for operation at  $-40^{\circ}\text{C}$ .

The electron-gun [93] mounted on a x-y moving table is used to inject electrons through the fibres. The gun is a small magnetic spectrometer using a  $\beta$ -emitting  $^{90}\text{Sr}$  source. A solenoid coil is used to select the electron energy using a calibrated magnetic field. A trigger system composed of three 1 mm square plastic fibres coupled to two single channel SiPMs is attached under the electron-gun. The electron kinetic energy at the fibre surface is approximately 1 MeV and deposit an energy of  $\sim 200\text{keV}$  over a relatively large region due to multiple scattering. Moreover, some tracks are non orthogonal.

Four SiPMs can be tested simultaneously over a temperature range from  $20^{\circ}\text{C}$  to  $-40^{\circ}\text{C}$ . Either SPIROC [94], VATA64 [95], PACIFIC [38] or Beetle [96] front-end electronic can be used for the readout and so the effect of the shaping time can be studied. More precisely, the following choices are possible:

- **VATA64:** Linear response with input signal charge and tunable shaping time set for the

## Appendix A. Experimental methods

measurement to  $\tau_{shaping} > 500$  ns.

- **SPIROC:** Linear response with input signal charge and shaping time of  $\tau_{shaping} \approx 70$  ns (FWHM).
- **Beetle:** Readout used for the BGV detector [92]. The front-end electronics includes an attenuator circuit for each channel to adapt the SiPM signals to the Beetle inputs. It has a non-linear response with the input signal charge and  $\tau_{shaping} \approx 25$  ns.
- **PACIFIC:** Readout used for the LHCb SciFi. The shaping time is  $\tau_{shaping} \approx 25$  ns. More information can be found in Sec.(3.6).

Either VATA64 or SPIROC front-end electronic are mainly used but only SPIROC is for the study of irradiated detectors. The SPIROC incorporates a DAC for each channel used to adjust the  $V_{bias}$  with respect to  $V_{BD}$ . A voltage offset on the effective  $V_{bias}$  of about 4.4 V for all channels has to be taken into account when using the SPIROC electronics though this offset value depend on the SiPM current. A calibration of the offset as a function of the current was performed by leaking ambient light on the detector. The photon peak deformation due to the current increase can be seen in Fig.(A.3).

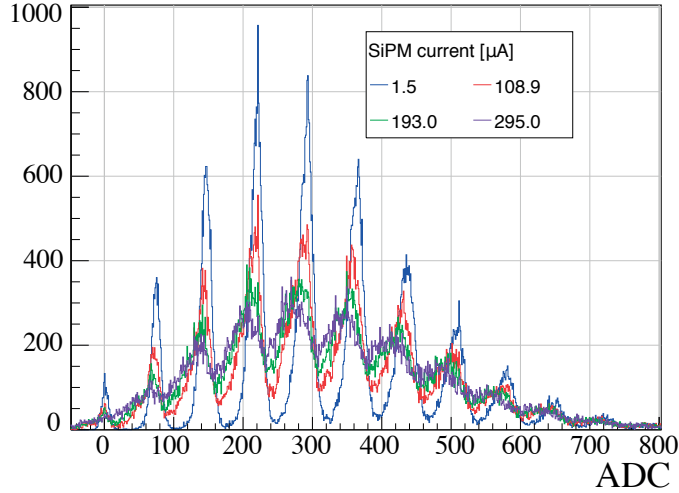


Figure A.3: Light intensity recorded by one channel for different SiPM current. The front-end is the SPIROC chip.

While the peaks are getting wider with increasing current, the position of the peaks is also shifting. The resulting measured gain as a function of the SiPM current can be seen in Fig.(A.4). An almost linear behaviour until  $250 \mu\text{A}$  is observed and is attributed to an increase of the SPIROC DAC voltage offset. For larger current, the flattening of the photon peaks leads to an underestimate of the gain by the peak finding algorithm. Measurement using the electron-gun have a too low current and this effect can be neglected.

VATA64 front-end electronic do not feature a voltage offset and is rather insensitive to large

## A.5. Test setup with short SciFi module and electron-gun

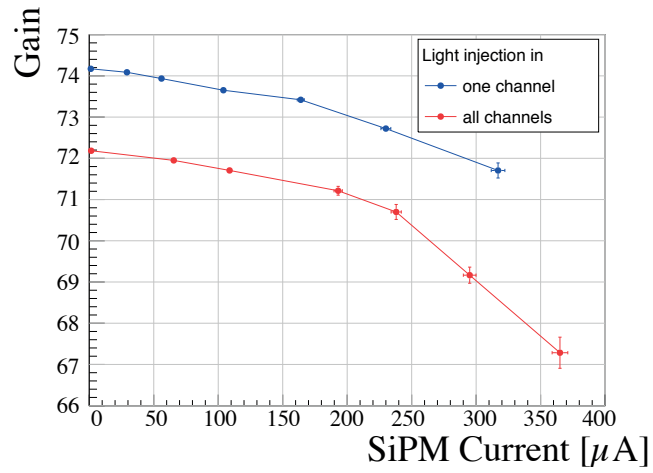


Figure A.4: SPIROC gain as a function of the current when light is injected over one channel or over all channels. The gain is decreasing linearly up to 250  $\mu\text{A}$  in both light injection procedures.

current.  $R_Q$  is observed to change with temperature which leads to a variation of the pulse long component because  $\tau_{\text{long}} = R_Q \cdot (C_q + C_d)$ .



## B Production testing and quality assurance

To ensure the best possible operation of the SciFi, the SiPMs are controlled and classified as a function of electrical and mechanical parameters. The detector is rejected for parameters below a predefined threshold. A grey-room as been installed to perform production tests in a controlled area. The entrance in the controlled area is made through a sas where shoes and hair protections, lab shirt and anti-static glows are available. Precautions regarding dust and static electricity were taken. A picture of the clean room can be seen in Fig.(B.1). The grey-room is organised in stations where each station is dedicated to one quality control test. Each station is equipped with a nitrogen gun for dust removal.

After the testing, detectors are temporary stored in a nitrogen controlled dry cabinet, before being packaged and sent to the module assembly centres.



Figure B.1: Picture of the grey-room.

During the production, three quality assurance tests are performed. The electrical connection are verified and  $V_{BD}$  is measured, the geometrical properties are measured and the optical surface is inspected.

### B.1 Electrical tests and breakdown measurement

The electrical tests are performed in three steps. First, electrical tests are done on samples before the balling procedure and the soldering on the flex. The detector is mounted in a BGA adaptor and measured in the IV multiplexer setup. Second, the detectors are electrically tested at the Valtronic company after the assembly. The test setup used can be seen in Fig.(B.2) and is meant for short and open connection detection. A tension of 2.5 V in forward bias direction is applied to measure the current. The Pt1000 resistance is also controlled. An extractor is mounted for a vertical detector extraction assuring lower constrains on the connectors.

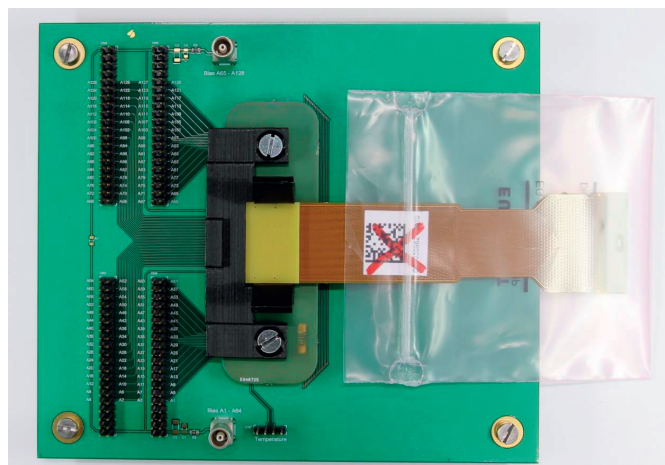


Figure B.2: Electrical test system used at Valtronic. A tension of 2.5 V in forward bias direction is applied to measure the current.

$V_{BD}$  is measured for all channels on all device at EPFL after the assembly.  $V_{BD}$  is a crucial property to operate the detector correctly and has to be measured precisely. I-V curves cannot reach the necessary precision of  $V_{bd}$ . Computing the gain in the low light spectrum and extrapolating it to zero is the most precise way to determine it. A light tight box has been developed that allows  $V_{BD}$  measurement of 8 SiPMs simultaneously. The features are:

- Short measurement time. The goal is to measure 8 detectors in less than 10 minutes.
- Simple handling of detectors. This implies no screws to hold the detectors and easy access, for mounting and unmounting.
- Homogenous light injection system. A system similar to the LHCb SciFi light injection system is used. It is based on a scratched fibre that distributes the photons over its length. The optical fibre is coupled to a depolished plexiglas piece to improve the light homogeneity. A plastic protection is added on the plexiglas bar to protect the optical surface and needs to be exchanged frequently because of accumulated dirt.



## B.2. Geometrical properties measurement

- Constant temperature at 25°C. A heat spreader is put on the top of the SiPMs to thermalise the detectors. The temperature sensor of each detector is read out for temperature control and functionality test of the probe.

The SiPMs readout is done by VATA64 chips [95]. A picture of the setup can be seen in Fig.(B.3). A QR code reader is provided to read the code bar identifying the SiPM.

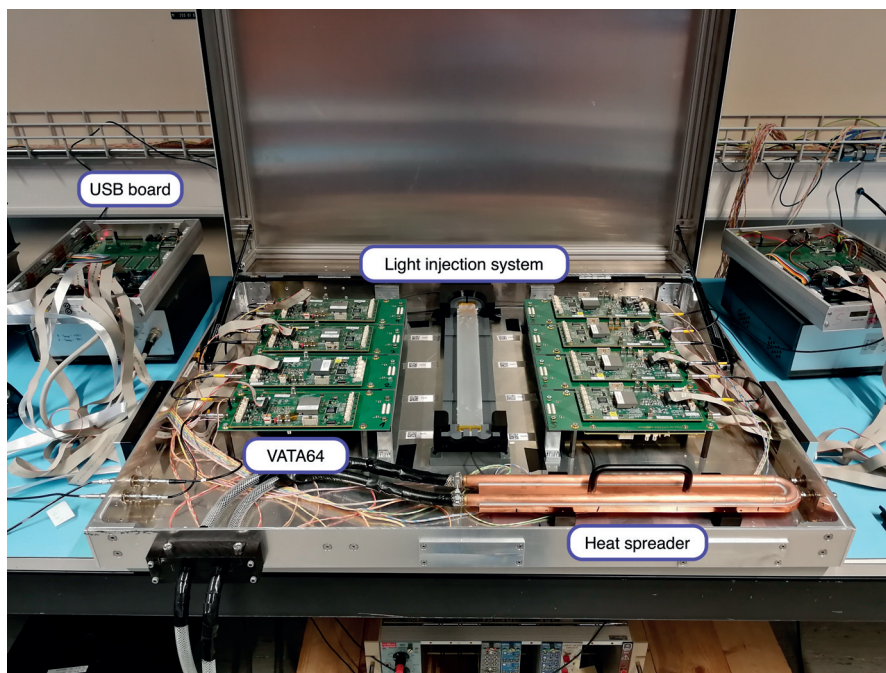


Figure B.3: Picture of the production breakdown test setup. Up to 8 SiPMs can be read out simultaneously with the VATA64 electronic. Temperature is kept constant through a heat spreader. Signal homogeneity is assured by a light injection system.

The gain computation is done with a peak finding method applied on the low light spectrum. The gain extrapolation and  $V_{BD}$  computation is based on the algorithm presented in Sec.(6.1.1). It allows a fast and precise way to determine  $V_{BD}$  for all 128 channel for all 8 detectors. The SiPMs are grouped by similar sets of  $V_{BD}$  in addition to the total thickness classification explained in the following section.

## B.2 Geometrical properties measurement

The SiPM chip is slightly bent along its length taking a "banana shape" parametrised by  $\delta$ , the arc height, as shown in Fig.(B.4). A max  $\delta$  of 100  $\mu\text{m}$  is accepted after the assembly though a maximum of  $\delta=40\ \mu\text{m}$  non-flatness has been seen in the pre-production series. The tolerances for the different dimensions can be seen in Tab.(B.1) as defined in Fig.(B.4).

All geometrical dimensions are measured on selected samples before the mounting on the flex.

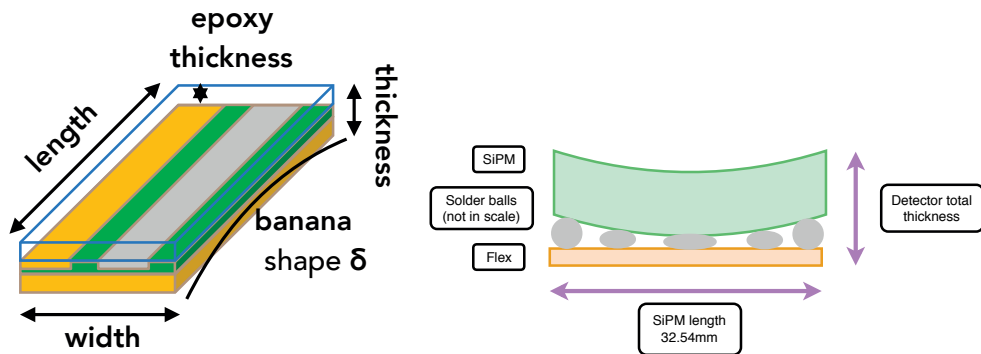


Figure B.4: Right shows the definition of the different dimensions on the non-assembled SiPM. Left shows the dimensions for the assembled flex.

Tolerances	
Width [mm]	$6.6 \pm 0.5$
Epoxy thickness [ $\mu\text{m}$ ]	$105 \pm 20$
Length [mm]	$32.54 \pm 0.05$
Thickness [mm]	$1.16 \pm 0.2$

Table B.1: SiPM chip tolerances on the different dimensions.

After assembly, the total thickness in the center and edges of the active surface is measured on all devices. The detectors with similar total thickness as well as  $V_{BD}$  are grouped by sets of four for glueing on the same cooling bar.

For the metrology, a vacuum based positioning system is used to ensure a repeatable positioning of the flex. An optical method is used to avoid any contact with the SiPM surface, lowering the risk of damages. A Heidenhain measurement probe is placed on the microscope focusing system, measuring the height difference between two focused points. To measure the total thickness, the focus is first made at the center of the active surface and then to a reference point on the periphery. This distance defines the curvature parameter  $\delta$ .

### B.3 Optical inspection

The optical surface inspection is carried under a microscope. Most of the damages and imperfections on the optical window are only seen using a coaxial light. A vacuum positioning system is used to simplify the SiPM placement. The optical surface inspection purpose is:

- Qualification and acceptance of the optical surface imperfections like scratches, hot drops or dirt particles in the epoxy for all devices.
- Cleaning with isopropyl alcohol if needed.

A picture of the setup can be seen in Fig.(B.6).

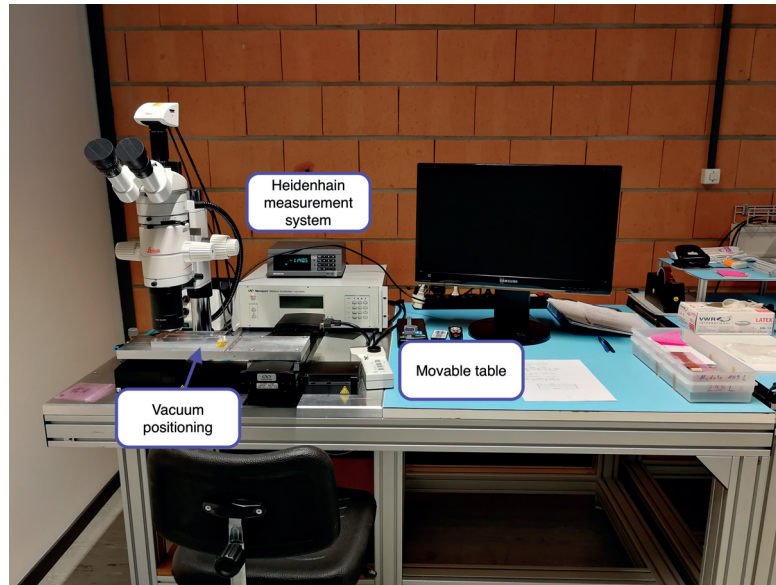


Figure B.5: Picture of the geometrical inspection setup. A Heidenhain measurement probe is set on the focusing mechanism of the microscope and allows a relative measurement between two focal points.

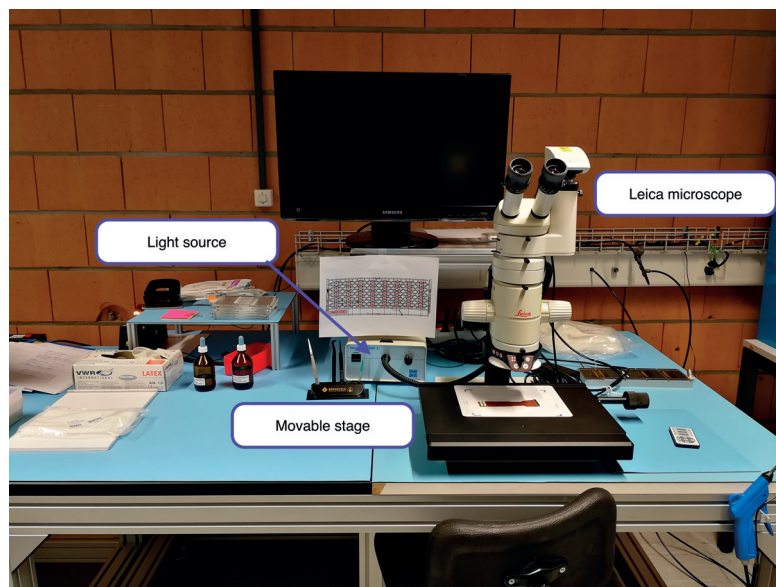


Figure B.6: Optical inspection setup. A microscope is used to inspect and qualify the detector surface. A movable stage allows to move the detector under the microscope. A coaxial light is used to distinguish surface damages.



# C SiPM micro-lens simulation

Each step of the lens simulation is described in the following.

## C.1 Photon generation

Photons are generated on a plane corresponding to the  $3 \times 3$  pixels grid and are given a random x/y position and an initial angle. The initial angle is randomly generated following the light angular distribution at the output of a scintillating fibre as shown in Fig.(C.1).

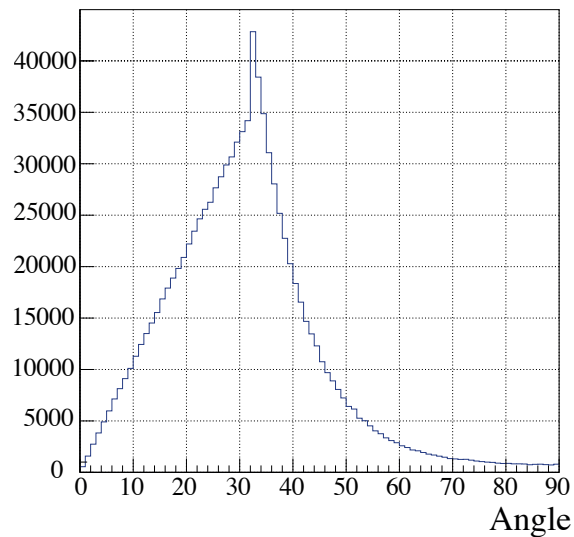


Figure C.1: Angular distribution of the generated photons from [76].

## C.2 Input of light on the lens

After generation, photons travel in air to the lens surface. The intersection point is given by solving the intersection of a vector and a sphere equation. The equation for a sphere centered in  $(x_0, y_0, z_0)$  is given by:

$$(x - x_0)^2 + (y - y_0)^2 + (z - z_0)^2 = R^2 \quad (\text{C.1})$$

with  $R$  the sphere radius. The equations of a vector in spherical coordinates are given by:

$$\begin{cases} x = \rho \sin(\phi) \cos(\theta) \\ y = \rho \sin(\phi) \sin(\theta) \\ z = \rho \cos(\phi) \end{cases} \quad (\text{C.2})$$

with  $\rho$ ,  $\phi$  and  $\theta$  the usual parameters of spherical coordinates. Equalising both equations, one gets the following equation:

$$\rho^2 + \rho(-2x_0 \sin(\phi) \cos(\theta) - 2y_0 \sin(\phi) \sin(\theta) - z_0 \cos(\phi)) + x_0^2 + y_0^2 + z_0^2 = R^2 \quad (\text{C.3})$$

Solving Eq.(C.3) for  $\rho$  and replace in Eq.(C.2) one gets the interaction point coordinates  $(x_{\text{int}}, y_{\text{int}}, z_{\text{int}})$  as a function of  $\phi$  (angle randomly generated following the distribution shown in Fig.(C.1)) and  $\theta$  (angle randomly generated between 0 and 360°).

## C.3 Light transport through the lens

Since air has a smaller refraction index ( $n_1=1.0$ ) compared to epoxy ( $n_2=1.5$ ) the incident photon has a probability to be reflected on the lens surface. This probability increases with the incident angle and can be approximated using Schlick's relation giving the reflection coefficient as:

$$R(\alpha) = R_0 + (1 - R_0)(1 - \cos(\alpha))^5 \quad (\text{C.4})$$

with  $R_0 = \left(\frac{n_1 - n_2}{n_1 + n_2}\right)^2$  and  $\alpha$  the angle between the incident light and the normal of the surface. The normal of a sphere is given by  $\vec{n} = \vec{\nabla}f(x, y, z)$  at the point of interaction  $p$  and with  $f(x, y, z)$  the function given in Eq.(C.1). Note that a change of referential is made to express the inter-

action point  $p(x_{\text{int}}, y_{\text{int}}, z_{\text{int}})$  in the referential attached to the beginning of the first pixel (as shown in Fig.(C.2)) of the grid.

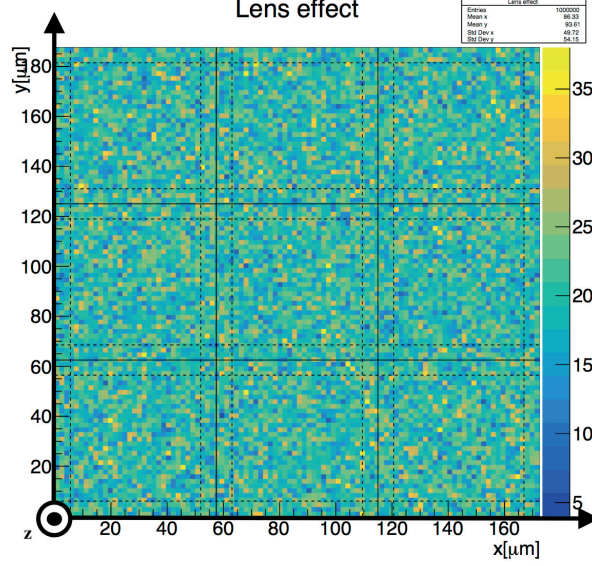


Figure C.2: Simulation of the  $3 \times 3$  pixels grid. The plot shows the photon distribution on the pixel grid without lenses.

The normal  $\vec{n} = \begin{pmatrix} n_1 \\ n_2 \\ n_3 \end{pmatrix}$  at point  $p$  is given by:

$$\begin{cases} n_1 = 2(x_{\text{int}} - x_0) \\ n_2 = 2(y_{\text{int}} - y_0) \\ n_3 = 2(z_{\text{int}} - z_0) \end{cases} \quad (\text{C.5})$$

and is normalised. The angle  $\alpha$  is then given by the scalar product between the normal vector and the incident light ( $\vec{l}_i$ ) vector:

$$\alpha = \cos^{-1} \left( \frac{\vec{n} \cdot \vec{l}_i}{\|\vec{n}\| \|\vec{l}_i\|} \right) \quad (\text{C.6})$$

The next step is to check if the photon is reflected or transmitted using Schlick's approximation. In the case where the photon is reflected, the direction is calculated. A reflected photon with a direction toward the pixel grid can still be detected by an active area. The intersection point of the reflected photon is obtained by solving the equation of a vector crossing a plane. Else the reflected photon event is rejected and do not participate in the computation of the light yield.

## Appendix C. SiPM micro-lens simulation

In the case where the incident photon is transmitted, the transmitted vector ( $\vec{l}_t$ ) is given by Snell's law in vectorial form:

$$\vec{l}_t = \frac{n_1}{n_2} [\vec{n} \times (-\vec{n} \times \vec{l}_i)] - \vec{n} \sqrt{1 - \left(\frac{n_1}{n_2}\right)^2 (\vec{n} \times \vec{l}_i) \cdot (\vec{n} \times \vec{l}_i)} \quad (\text{C.7})$$

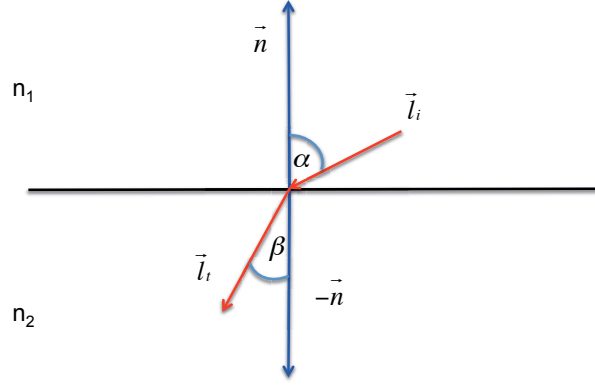


Figure C.3: Vectors and angles definition for the vectorial Snells law.

The final position at the silicon surface is given by the intersection of the transmitted vector and the silicon plane. The following intersection points ( $x_f, y_f, z_f$ ) are obtained:

$$\begin{cases} x_f = -\frac{z_{\text{int}}}{l_{iz}} l_{ix} + x_{\text{int}} \\ y_f = -\frac{z_{\text{int}}}{l_{iz}} l_{iy} + y_{\text{int}} \\ z_f = -\frac{z_{\text{int}}}{l_{iz}} l_{iz} + z_{\text{int}} \end{cases} \quad (\text{C.8})$$

### C.4 SiPM pixel simulation and corresponding fill factor

The pixel geometry is implemented and a simple algorithm checks if ( $x_f, y_f, z_f$ ) for each photon is on a dead or an active area. Note that photons hitting a final position outside the  $3 \times 3$  pixel are not taken into account in the total number of photon used to measure the light yield increase. The corresponding fill factor is the ratio of photons hitting on the sensitive area to the total number of photons reaching the SiPM pixels.

Since the simulation only generates one lens for 9 pixels, the CFF increase obtained has to be multiply by a factor 4.5 for a chequerboard deposition of lenses on the pixel grid since one out of two pixels is equipped with a lens.



## D Testbeam campaigns

A summary of the measurement performed during the testbeam campaigns are presented:

**May 2015 SPS:** Measurements of the light yield, attenuation length,  $\Delta V$  scan, hit detection efficiency and resolution for five and six layer mats (2.5 m) were performed. The AMS ladder telescope and VeLo TimePix were used.

**November 2015 SPS:** Measurements of the light yield of an irradiated 6 layer 2.5 m mat and first PACIFIC chip test. First installation of the fibre telescope used with the VeLo TimePix instead of the AMS ladder telescope. Measurement of the hit detection efficiency, light yield, resolution and track reconstruction for an installed BGV module were also measured. The SciFi telescope used in 2015 consisted of a single box with five tracking stations. The extrapolation of the track to the long SciFi modules introduced a significant error on the resolution. The complete results for the 2015 campaign can be found in [81].

**May 2016 SPS:** Measurements using the split telescope presented previously were performed. It allows to place the long SciFi modules between the telescope boxes. No SciFi long modules were installed. Synchronisation problems in the telescope resulted in unusable data and was solved for next testbeams.

**Nov. 2016 SPS:** Measurements of hit detection efficiency, light yield and angular scans were performed. The measurement were performed on irradiated 6 layer long fibre mats. Inside the telescope H2016\_HRQ and KETEK detectors were evaluated.

**Feb. 2017 DESY:** This testbeam was dedicated to PACIFICr4 test and SPIROC was used as reference. Two modules were tested, one irradiated and one non-irradiated. Both modules are equipped with H2016\_HRQ detectors. The light yield for both modules with electrons was determined using the SPIROC chip. The SciFi telescope was used for track reconstruction.

**Aug. 2017 DESY:** Measurements of long fibre modules were performed. The hit detection efficiency of the PACIFICr5 was measured for different injection points (close to the

## Appendix D. Testbeam campaigns

---

mirror and at 70 cm closer to the SiPM), different  $\Delta V$  and injection angles. The SciFi telescope was used for track reconstruction.

**Oct. 2017 SPS:** Measurements on an updated telescope were performed. The telescope stations were equipped with H2017 detectors for characterisation. Hit efficiency, light yield and resolution were measured and new clustering algorithms were studied.

# Bibliography

- [1] C. Lefèvre, *The CERN accelerator complex. Complexe des accélérateurs du CERN*, Dec, 2008.
- [2] LHCb collaboration, A. A. Alves Jr. *et al.*, *The LHCb detector at the LHC*, JINST **3** (2008) S08005.
- [3] LHCb collaboration, *Production angle plot at 8 TeV*, [https://lhcb.web.cern.ch/lhcb/speakersbureau/html/bb\\_ProductionAngles.html](https://lhcb.web.cern.ch/lhcb/speakersbureau/html/bb_ProductionAngles.html).
- [4] LHCb collaboration, *LHCb : Technical Proposal*, Tech. Proposal, CERN, Geneva, 1998.
- [5] LHCb collaboration, *Tracking and Alignment Plots for Conferences*, <https://twiki.cern.ch/twiki/bin/view/LHCb/ConferencePlots>.
- [6] R. Aaij *et al.*, *Performance of the LHCb Vertex Locator*, JINST **9** (2014) P09007, arXiv:1405.7808.
- [7] LHCb collaboration, *LHCb VELO (VVerteX LOcator): Technical Design Report*, CERN-LHCC-2001-011. LHCb-TDR-005.
- [8] LHCb collaboration, *LHCb VELO Upgrade Technical Design Report*, CERN-LHCC-2013-021. LHCb-TDR-013.
- [9] J. Gassner, F. Lehner, and S. Steiner, *The mechanical Design of the LHCb Silicon Trigger Tracker*, Tech. Rep. LHCb-2004-110. CERN-LHCb-2004-110, CERN, Geneva, Aug, 2010.
- [10] LHCb collaboration, *LHCb Silicon Tracker - Material for Publications*, <http://www.physik.unizh.ch/groups/lhcb/public/material/>.
- [11] LHCb collaboration, *Outer tracker module design*, <https://www.nikhef.nl/pub/experiments/bfys/lhcb/outerTracker/Intro/module.html>.
- [12] E. Rodrigues, *Tracking definitions*, Tech. Rep. LHCb-2007-006. CERN-LHCb-2007-006, CERN, Geneva, Feb, 2007. revised version submitted on 2007-03-28 09:34:37.
- [13] *Letter of Intent for the LHCb Upgrade*, Tech. Rep. CERN-LHCC-2011-001. LHCC-I-018, CERN, Geneva, Mar, 2011.

## Bibliography

---

- [14] LHCb collaboration, *LHCb Tracker Upgrade Technical Design Report*, CERN-LHCC-2014-001. LHCb-TDR-015.
- [15] LHCb collaboration, *LHCb Trigger and Online Technical Design Report*, CERN-LHCC-2014-016. LHCb-TDR-016.
- [16] LHCb collaboration, *Framework TDR for the LHCb Upgrade: Technical Design Report*, CERN-LHCC-2012-007. LHCb-TDR-012.
- [17] G. Battistoni *et al.*, *The FLUKA code: Description and benchmarking*, in *Proceedings of the Hadronic Shower Simulation Workshop 2006* (M. Albrow and R. Raja, eds.), AIP Conference Proceeding 896, pp. 31–49, 2007.
- [18] A. Fasso *et al.*, *FLUKA: a multi-particle transport code*, 2005. CERN-2005-10, INFN/TC05/11, SLAC-R-773.
- [19] M. Karacson, *Simulation Studies for a Neutron Shield for the new SciFiTracker in LHCb*, .
- [20] T. Matsumura *et al.*, *Effects of radiation damage caused by proton irradiation on Multi-Pixel Photon Counters (MPPCs)*, Nucl. Instr. Meth. **A603** (2009) 301.
- [21] C. Joram, G. Haefeli, and B. Leverington, *Scintillating fibre tracking at high luminosity colliders*, Journal of Instrumentation **10** (2015), no. 08 C08005.
- [22] LHCb collaboration, *LHCb SciFi Tracker - Material for Conferences*, <https://twiki.cern.ch/twiki/bin/view/LHCb/SciFiConference>.
- [23] O. Girard, *SciFi working principle illustration*, Private communication 16 April 2018.
- [24] G. F. Knoll, *Radiation detection and measurement; 4th ed.*, Wiley, New York, NY, 2010.
- [25] T. White, *Scintillating fibres*, Nucl. Instrum. Meth. A273 (1988) 820.
- [26] I. O. Ruiz, *Accurate Profile Measurement of the low intensity secondary beams in the CERN experimental areas*, 2018. to be completed.
- [27] I. B. Berlman, *Handbook of fluorescence spectra of aromatic molecules (second edition)*, Academic Press, second edition ed., 1971.
- [28] M. Deckenhoff and B. Spaan, *Scintillating Fibre and Silicon Photomultiplier Studies for the LHCb upgrade*, Dec, 2015. Presented 23 Feb 2016.
- [29] Kuraray, *Kuraray webpage*, <http://kuraraypsf.jp/psf/index.html>.
- [30] C. Joram, *Technical specifications of the scintillating fibres*, Tech. Rep. LHCb-PUB-2014-019. CERN-LHCb-PUB-2014-019. LHCb-INT-2013-061, CERN, Geneva, Feb, 2014.

- 
- [31] M. Tobin, *Lhcb upgrade: Scintillating fibre tracker*, Nuclear Instruments and Methods in Physics Research Section A: Accelerators, Spectrometers, Detectors and Associated Equipment **824** (2016) 148 , Frontier Detectors for Frontier Physics: Proceedings of the 13th Pisa Meeting on Advanced Detectors.
- [32] C. Joram *et al.*, *LHCb Scintillating Fibre Tracker Engineering Design Review Report: Fibres, Mats and Modules*, Tech. Rep. LHCb-PUB-2015-008. CERN-LHCb-PUB-2015-008, CERN, Geneva, Mar, 2015.
- [33] Hamamatsu photonics  
<http://www.hamamatsu.com>.
- [34] KETEK GmbH  
<https://www.ketek.net/>.
- [35] W. E. W. Vink *et al.*, *Lhcb scintillating fiber detector front end electronics design and quality assurance*, Journal of Instrumentation **12** (2017), no. 03 C03053.
- [36] J. M. de Cos *et al.*, *Pacific: Sipm readout asic for lhcb upgrade*, Nuclear Instruments and Methods in Physics Research Section A: Accelerators, Spectrometers, Detectors and Associated Equipment (2017) .
- [37] K. Wyllie *et al.*, *Electronics Architecture of the LHCb Upgrade*, Tech. Rep. LHCb-PUB-2011-011. CERN-LHCb-PUB-2011-011, CERN, Geneva, Jun, 2013. Previous version: 01/03/2013 Current version: 18/06/2013 (version 2.6) based on LHCb-INT-2011-006 (removed from CDS).
- [38] J. Mazorra *et al.*, *Pacific: the readout asic for the scifi tracker of the upgraded lhcb detector*, Journal of Instrumentation **11** (2016), no. 02 C02021.
- [39] D. Gascon *et al.*, *Pacific: A 64-channel asic for scintillating fiber tracking in lhcb upgrade*, Journal of Instrumentation **10** (2015), no. 04 C04030.
- [40] S. Giani *et al.*, *Digitization of SiPM signals for the LHCb Upgrade SciFi tracker*, Tech. Rep. LHCb-PUB-2014-025. CERN-LHCb-PUB-2014-025. LHCb-INT-2013-065, CERN, Geneva, Feb, 2014.
- [41] Particle Data Group, K. A. Olive *et al.*, *Review of Particle Physics*, Chin. Phys. **C38** (2014) 090001.
- [42] National Institute of Standards and Technology, Gaithersburg, MD., Berger, M. J. , Hubbell, J. H. , Seltzer, S. M. , Chang, J. , Coursey, J. S. , Sukumar, R. , Zucker, D. S. , and Olsen, K. , *XCOM: Photon Cross Section Database (version 1.5)*,  
<http://physics.nist.gov/xcom> visitend in 2018, February 15, 2010.
- [43] SensL, *Introduction to SiPM, Technical note*,  
<https://www.sensl.com/downloads/ds/TN%20-%20Intro%20to%20SPM%20Tech.pdf>.

## Bibliography

---

- [44] Hamamatsu Photonics, *Photomultiplier Tubes: Basics and Applications, 3rd Edition (3a, 2007)*, .
- [45] G. Anzivino *et al.*, *Review of the hybrid photo diode tube (hpd) an advanced light detector for physics*, Nuclear Instruments and Methods in Physics Research Section A: Accelerators, Spectrometers, Detectors and Associated Equipment **365** (1995), no. 1 76 .
- [46] Hamamatsu, *HPD webpage*,  
[https://www.hamamatsu.com/us/en/community/optical\\_sensors/articles/intro\\_to\\_hpd/index.html](https://www.hamamatsu.com/us/en/community/optical_sensors/articles/intro_to_hpd/index.html).
- [47] Leica microsystem, Rolf T. Borlinghaus, Holger Birk, Frank Schreiber, *Sensors for True Confocal Scanning*,  
<https://www.leica-microsystems.com/science-lab/sensors-for-true-confocal-scanning/>, 2012.
- [48] S. Eisenhardt, *Production and tests of hybrid photon detectors for the lhcb rich detectors*, Nuclear Instruments and Methods in Physics Research Section A: Accelerators, Spectrometers, Detectors and Associated Equipment **595** (2008), no. 1 142 , RICH 2007.
- [49] M. Villa, *The LHCb RICH PMTs readout electronics and the monitoring of the HPDs quantum efficiency*, Master's thesis, Milan Bicocca U., 2007.
- [50] T. Gys, *Micro-channel plates and vacuum detectors*, Nuclear Instruments and Methods in Physics Research Section A: Accelerators, Spectrometers, Detectors and Associated Equipment **787** (2015) 254 , New Developments in Photodetection NDIP14.
- [51] Hamamatsu, *MCP webpage*,  
[http://www.hamamatsu.com/jp/en/community/optical\\_sensors/applications/mass\\_spectrometry/index.html](http://www.hamamatsu.com/jp/en/community/optical_sensors/applications/mass_spectrometry/index.html).
- [52] S. M. Sze and K. K. Ng, *Physics of Semiconductor Devices*, Wiley, 2006.
- [53] E. Ravotti, *Development and characterisation of radiation monitoring sensors for the high energy physics experiments of the CERN LHC accelerator*, PhD thesis, Montpellier U., 2006.
- [54] Hamamatsu, *Opto-semiconductor handbook, Chapter 03 Si APD and MPPC*,  
[https://www.hamamatsu.com/resources/pdf/ssd/e03\\_handbook\\_si\\_apd\\_mppc.pdf](https://www.hamamatsu.com/resources/pdf/ssd/e03_handbook_si_apd_mppc.pdf).
- [55] D. Zürcher, *Nuclear counter effect and pi-e misidentification*, Nuclear Instruments and Methods in Physics Research Section A: Accelerators, Spectrometers, Detectors and Associated Equipment **442** (2000), no. 1 433 .
- [56] CMS, S. Chatrchyan *et al.*, *The CMS Experiment at the CERN LHC*, JINST **3** (2008) S08004.
- [57] C. Biino, *The cms electromagnetic calorimeter: overview, lessons learned during run 1 and future projections*, Journal of Physics: Conference Series **587** (2015), no. 1 012001.

- 
- [58] J. Grahl *et al.*, *Radiation hard avalanche photodiodes for cms ecal*, Nuclear Instruments and Methods in Physics Research Section A: Accelerators, Spectrometers, Detectors and Associated Equipment **504** (2003), no. 1 44 , Proceedings of the 3rd International Conference on New Developments in Photodetection.
- [59] S. Cova *et al.*, *Avalanche photodiodes and quenching circuits for single-photon detection*, Appl. Opt. **35** (1996) 1956.
- [60] N. Otte, *The silicon photomultiplier - a new device for high energy physics, astroparticle physics, industrial and medical applications*, .
- [61] G. Collazuol, *The sipm physics and technology- a review*, LAL Orsay, 2012.
- [62] F. Corsi *et al.*, *Modelling a silicon photomultiplier (SiPM) as a signal source for optimum front-end design*, Nuclear Instruments and Methods in Physics Research A **572** (2007) 416.
- [63] Hamamatsu, *SiPM webpage*,  
[https://www.hamamatsu.com/us/en/community/optical\\_sensors/articles/technical\\_guide\\_to\\_silicon\\_photomultipliers\\_sipm/index.html](https://www.hamamatsu.com/us/en/community/optical_sensors/articles/technical_guide_to_silicon_photomultipliers_sipm/index.html).
- [64] P. von Doetinchem *et al.*, *PEBS - Positron Electron Balloon Spectrometer*, Nucl. Instrum. Meth. **A581** (2007) 151.
- [65] B. Beischer *et al.*, *A High-resolution Scintillating Fiber Tracker With Silicon Photomultiplier Array Readout*, Nucl. Instrum. Meth. **A622** (2010) 542.
- [66] E. Garutti *et al.*, *Characterization and X-Ray Damage of Silicon Photomultipliers*, PoS **TIPP2014** (2014) 070.
- [67] M. Moll, *Radiation damage in silicon particle detectors: Microscopic defects and macroscopic properties*, PhD thesis, Hamburg U., 1999.
- [68] V. Radulovic *et al.*, *Large Object Irradiation Facility In The Tangential Channel Of The JSI TRIGA Reactor*, .
- [69] M. J. Boschini, P. G. Rancoita and M. Tacconi, *SR-NIEL Calculator: Screened Relativistic (SR) Treatment for Calculating the Displacement Damage and Nuclear Stopping Powers for Electrons, Protons, Light- and Heavy- Ions in Materials (version 3.9.5)*, available at INFN sez. Milano-Bicocca, Italy [2018, March]: <http://www.sr-niel.org/>, 2014.
- [70] M. Auger *et al.*, *Accelerator and detector physics at the Bern medical cyclotron and its beam transport line*, Nukleonika **61** (2016), no. 1 .
- [71] L. An, G. Haefeli, O. Girard, and A. Kuonen, *Testbeam analysis for a scintillating fibre telescope*,  
[http://lphe.epfl.ch/publications/2017/Testbeam\\_Liupan.pdf](http://lphe.epfl.ch/publications/2017/Testbeam_Liupan.pdf).

## Bibliography

---

- [72] M. Moll, E. Fretwurst, and G. Lindstroem, *Leakage current of hadron irradiated silicon detectors - material dependence*, Nuclear Instruments and Methods in Physics Research Section A: Accelerators, Spectrometers, Detectors and Associated Equipment **426** (1999), no. 1 87 .
- [73] O. Girard, G. Haefeli, A. Kuonen, and M. E. Stramaglia, *Read-out of irradiated SiPMs attached to short scintillating fibre module*, <http://lphe.epfl.ch/publications/2017/LPHE-2017-002.pdf>.
- [74] PacTech, *Laser Solder Jetting Systems*, [http://www.pactech.com/wp-content/uploads/2016/12/PacTech\\_SB2Systems\\_201512.pdf](http://www.pactech.com/wp-content/uploads/2016/12/PacTech_SB2Systems_201512.pdf).
- [75] A. Caratelli *et al.*, *The GBT-SCA, a radiation tolerant ASIC for detector control and monitoring applications in HEP experiments*, JINST **10** (2015), no. 03 C03034.
- [76] S. Nieswand and T. Hebbeker, *Measurement of the exit characteristics of light from optical multimode plastic fibres*, 2014.
- [77] M. Kiaee, *SiPM Project, Primary results 21/10/2016*, .
- [78] P. Brugger, *Microsystems laboratory website for inkjet printer* , <https://lmis1.epfl.ch/page-34709.html>.
- [79] SensL, *J-Series SiPMs*, <http://sensl.com/downloads/ds/DS-MicroJseries.pdf>.
- [80] Hamamatsu, *Opto-semiconductor handbook chapter 13*, [https://www.hamamatsu.com/resources/pdf/ssd/e13\\_handbook\\_technology.pdf](https://www.hamamatsu.com/resources/pdf/ssd/e13_handbook_technology.pdf).
- [81] A. B. Rodrigues Cavalcante *et al.*, *LHCb Scintillating Fibre Tracker: Test Beam Report 2015*, Tech. Rep. LHCb-PUB-2015-025. CERN-LHCb-PUB-2015-025, CERN, Geneva, Nov, 2015.
- [82] O. Girard, *Modular beam telescope based on scintillating fibres and silicon photomultipliers*, <https://indico.desy.de/indico/event/18050/session/9/contribution/18>.
- [83] P. Wampler *et al.*, *Measurement of Hit Detection Efficiency and Resolution of Short Scintillating Fiber Modules*, [http://lphe.epfl.ch/publications/specialisation\\_semester/Wampler\\_Specialisation.pdf](http://lphe.epfl.ch/publications/specialisation_semester/Wampler_Specialisation.pdf).
- [84] S. Ek-In *et al.*, *Modified Anti-kt Clustering Algorithm Developed for the SciFi Telescope*, [http://lphe.epfl.ch/publications/specialisation\\_semester/Ek-In\\_Specialisation.pdf](http://lphe.epfl.ch/publications/specialisation_semester/Ek-In_Specialisation.pdf).
- [85] P. Berclaz, *Analysis of particle telescope*, [http://lphe.epfl.ch/publications/2016/PBerclaz\\_Simulation\\_telescope.pdf](http://lphe.epfl.ch/publications/2016/PBerclaz_Simulation_telescope.pdf).



- 
- [86] B. D. Leverington, *Test beam results of the LHCb Scintillating Fibre Tracker*, <https://indico.desy.de/indico/event/18050/session/8/contribution/12>.
- [87] S. Nieswand, *SciFi testbeam at DESY September 18, 2017*, [https://indico.cern.ch/event/664962/contributions/2716003/attachments/1525080/2384393/Testbeam-Analysis\\_Merged.pdf](https://indico.cern.ch/event/664962/contributions/2716003/attachments/1525080/2384393/Testbeam-Analysis_Merged.pdf).
- [88] X. Han, *SciFi test beam at DESY*, [https://indico.cern.ch/event/615424/contributions/2482561/attachments/1418568/2173440/SciFi\\_testbeam\\_2017\\_DESY.pdf](https://indico.cern.ch/event/615424/contributions/2482561/attachments/1418568/2173440/SciFi_testbeam_2017_DESY.pdf).
- [89] B. D. Leverington, *DESY TEST BEAM RESULTS*, [https://indico.cern.ch/event/636629/contributions/2577507/attachments/1457699/2250568/SciFiGM\\_Testbeam\\_20170511.pdf](https://indico.cern.ch/event/636629/contributions/2577507/attachments/1457699/2250568/SciFiGM_Testbeam_20170511.pdf).
- [90] G. Collazuol *et al.*, *Studies of silicon photomultipliers at cryogenic temperatures*, Nuclear Instruments and Methods in Physics Research Section A: Accelerators, Spectrometers, Detectors and Associated Equipment **628** (2011), no. 1 389 , VCI 2010.
- [91] R. Brun and F. Rademakers, *Root - an object oriented data analysis framework*, Proceedings AIHENP'96 Workshop, Lausanne, Sep. 1996, Nucl. Inst. & Meth. in Phys. Res. A 389 (1997).
- [92] A. Alexopoulos *et al.*, *First lhc transverse beam size measurements with the beam gas vertex detector*, Journal of Physics: Conference Series **874** (2017), no. 1 012086.
- [93] S. C. Arfaoui, C. C. Joram, and C. E. Z. Casella, *Characterisation of a Sr-90 based electron monochromator*, Tech. Rep. PH-EP-Tech-Note-2015-003, CERN, Geneva, May, 2015.
- [94] S. Conforti Di Lorenzo *et al.*, *SPIROC: Design and performances of a dedicated very front-end electronics for an ILC Analog Hadronic CALorimeter (AHCAL) prototype with SiPM read-out*, JINST **8** (2013) C01027.
- [95] M. G. Bagliesia *et al.*, *A custom front-end ASIC for the readout and timing of 64 SiPM photosensors*, Nucl. Phys. B ( Proc. Suppl. ) **215** (2011) 344.
- [96] S. Löchner and M. Schmelling, *The Beetle Reference Manual - chip version 1.3, 1.4 and 1.5*, Tech. Rep. LHCb-2005-105. CERN-LHCb-2005-105, CERN, Geneva, Nov, 2006.



# Axel Kuonen

Physicist Engineer

Rte de Taillepied 7  
1095 Lutry  
☎ 079 589 63 11  
✉ axel.kuonen@gmail.com  
Swiss, 07.06.1990, Single



## Formation

- 2014 to end Aug. 2018 **Ph.D. student**, in *Particle Physics*, under the supervision of Prof. A. Bay and Dr. G. Haefeli, EPFL, Lausanne, Switzerland.  
Thesis subject: Development and Characterisation of Silicon Photomultiplier Multichannel Arrays for the Readout of a Large Scale Scintillating Fibre Tracker
- 2012-2014 **Master Degree**, in *Engineering Physics*, EPFL, Lausanne, Switzerland.
- 2008-2012 **Bachelor Degree**, in *Physics*, EPFL, Lausanne, Switzerland.
- Sep. 2008 **Maturité Fédérale**, *bilingual French-German*, Institut Mont-Olivet, Lausanne, Switzerland.

## Experiences

### Professional Experiences

- Aug. 2013 to Feb. 2014 **Compagny internship at TESA**, *Development of an optical test bench for production quality assurance*, TESA, Renens, Switzerland.
- Aug. 2012 **EPFL summer student**, *VCSEL setup elaboration for third year physics practical work*, EPFL, Lausanne, Switzerland.

### Awards

- Jun. 2017 **Best student presentation award**, *TIPP 2017 conference*, Beijing, China.

### Associative Experiences

- Aug. 2012 to this day **Chablais Blues Connection**, *Vice-president of the association*, planification and organisation of musical events for the association, Noville, Switzerland.
- Jun. 2009 to this day **Conseil communal of Lutry**, *Taking part in the political life*, Lutry, Switzerland.
- 2009-2011 **Coaching EPFL**, *Coaching formation, support for first year students and social events organisation*, EPFL, Lausanne, Switzerland.

## Scientific Schools

- 2016 **First Barcelona Technoweek**, *School on semiconductor detectors*, Barcelona, Spain.
- 2015 **4th EIROforum**, *School of instrumentation*, Garching, Germany.

## Software, Programming and technical skills

- Programming: C, C++, ROOT, Python, Matlab and LabView
- Software: Latex, Office and Git
- Technical: Development of test setups, knowledge in DAQ and QA, basic knowledge in mechanics and electronics
- Soft Skills: Communication, social interaction, team work, teaching, organisation and leadership

## Languages

- English **Superior level**
- German **Superior level**
- Swiss-German **Fluent in understanding**
- French **Mother tongue**